5-2014

Gravitational Wave Astrophysics with Compact Binary Systems

Eric Addison
Utah State University

Recommended Citation

Addison, Eric, "Gravitational Wave Astrophysics with Compact Binary Systems" (2014). *All Graduate Theses and Dissertations*. 2166.
https://digitalcommons.usu.edu/etd/2166

GRAVITATIONAL WAVE ASTROPHYSICS WITH COMPACT BINARY SYSTEMS

by

Eric Addison

A dissertation submitted in partial fulfillment
of the requirements for the degree

of

DOCTOR OF PHILOSOPHY

in

Physics

Approved:

Dr. Shane L. Larson
Major Professor

Dr. Charles Torre
Committee Member

Dr. Todd Moon
Committee Member

Dr. Eric Held
Committee Member

Dr. Michael Taylor
Committee Member

Dr. Mark R. McLellen
Vice President for Research and
Dean of the School of Graduate Studies

UTAH STATE UNIVERSITY
Logan, Utah

2014

ABSTRACT

Gravitational Wave Astrophysics with
Compact Binary Systems

by

Eric Addison, Doctor of Philosophy
Utah State University, 2014

Major Professor: Dr. Shane L. Larson
Department: Physics

In this dissertation, I present two studies in the field of gravitational wave astrophysics applied to compact binary systems. In the first project, I investigate simulated encounters between a binary system comprised of two stellar mass black holes with a galactic supermassive black hole. It is found that binaries disrupted by the supermassive black hole form extreme mass ratio inspirals (EMRIs), which would begin with very high eccentricity, $e \approx 1 - \mathcal{O}(10^{-2})$, but circularize dramatically by the emission of gravitational wave radiation. At the time when the stable orbit turns over to a plunge orbit, the EMRIs still have some small residual eccentricity, $e \approx 0.05$ on average, which is slightly larger than previous estimates. The surviving binaries are classified based on their final relation with the supermassive black hole. When inspecting the merger lifetime of the surviving binaries, a mean new merger lifetime of $\tilde{T} = 0.8T_0$ is found. Factoring in this new lifetime with other relevant data, I calculate the merger rate of these systems in the range of the advanced Laser Interferometer Gravitational Wave Observatory to be about 0.25 yr^{-1}, which represents a small percentage of the current predicted CBC rates.

In the second project I propose and explore a new method of estimating the radius of the accretion disc in cataclysmic variable binary systems though the use of coupled electromagnetic and gravitational wave observations. By identifying the angle of the hot spot formed by the impact of the accretion stream with the disc, ϕ_{HS}, the radius of the disc can be recovered. I test the proposed method against fully simulated lightcurve output, as well as the true observed AM CVn lightcurve. In both cases, I find our method capable of estimating the disc radius to high precision. I calculate a disc radius of $\hat{R}_D/a \approx 0.476 \pm 0.025$ for the fully simulated data and $\hat{R}_D/a \approx 0.481 \pm 0.05$ for the true lightcurve data. These estimates agree with the accepted value of $R_D = 0.478a$ within the uncertainties, and differ from the accepted value by 0.4% and 0.6%, respectively. Because this method does not rely on eclipses, it will be applicable to a much broader population of binaries.

(164 pages)

PUBLIC ABSTRACT

Gravitational Wave Astrophysics with
Compact Binary Systems

Eric Addison

Gravitational waves are ripples in the fabric of spacetime that convey information about changing gravitational fields. Large-scale detection projects are currently in operation, and more advanced detectors are being designed and built. Though we have yet to make a direct detection of a gravitational wave signal, upgrades to current detectors are expected to bring the first detections within the next year or two.

Gravitational waves will bring us information about astrophysical phenomena that is complementary to the information gained from photon-based observations (e.g., telescopes and radio receivers). One of the primary sources of gravitational waves are binary systems: two massive objects that orbit around each other due to their mutual gravitational attraction. These systems can have very predictable gravitational wave signatures due to their repetitive motions, making them ideal gravitational wave sources.

In this dissertation, I present two research projects pertaining to gravitational wave astrophysics and compact binary systems. In the first, I explore interactions between compact binary systems near the center of our galaxy with the supermassive black hole that resides there. I am interested in the final state of the binary as a result of the interaction, ranging from small perturbations to the orbit up to total disruption. In the case of disruption, I characterize the new orbits formed between the binary components and the central black hole, known as extreme mass ratio inspirals. For binaries that survive the encounter, I examine the changes they experience, and find on average, they will merge together as a result of gravitational wave emission faster than before the encounter.

In the second project, I propose a new method of measuring the radius of the swirling disc of gas and dust that encircles some stars in compact binary systems, known as the accretion disc. This method relies on the use of coupled electromagnetic and gravitational

wave observations, a synthesis of information known as multi-messenger astronomy. This new method proves very accurate when used on both simulated and observed data from a candidate system known as AM CVn.

The simulation codes written for this research are freely available at

- https://github.com/ericaddison/Binary-SMBH-Encounter-Simulation
- https://github.com/ericaddison/LightCurveSim

I also plan to post the codes to the Astrophysics code database Starship Asterisk (http://asterisk.apod.com/) once the corresponding papers are published.

This dissertation is dedicated to my daughter Luca, the bringer of light,
and to tiny Tori, the bringer of victory.

ACKNOWLEDGMENTS

I would like to express my deepest gratitude to my advisor, Dr. Shane Larson. His enthusiasm for physics and science appears to be infinite, which makes him an incredible scientist to work with. Shane's encouragement and flexibility allowed me to construct an educational experience I am proud of, and to gain the variety of skills I will need as a research scientist. I am indebted to Shane for all he has done for me.

I would also like to acknowledge and thank my committee members, Dr. Charles Torre, Dr. Todd Moon, Dr. Eric Held, and Dr. Michael Taylor, for making my time in graduate school challenging and enjoyable. Dr. Torre and Dr. Moon, in particular, gave me personalized attention regularly throughout my time as a graduate student, for which I am grateful.

Thanks are due to Department Head, Dr. Jan Sojka, and the Utah State University Department of Physics not only for providing a strong support network and teaching opportunities, but also for giving me the chance to enter the field of physics in the first place. Without a physics undergraduate degree, the department was under no obligation to even consider my application for entrance into the graduate program. I truly appreciate the chance I was given, and hope that I have been a positive addition to the student body during my time here.

In the department office, Karalee Ransom and Sharon Pappas have been stalwart heroes in this process. Their unwavering cheerfulness and efficiency in handling administrative matters made easy work of what could have been a painful experience.

Support for the work in this dissertation was provided in part through federal research grants, including National Science Foundation award PHY-0970152 and NASA award NNX13AM10G. Additional support was provided by the Howard L. Blood Endowment, the Gene Adams Endowment, and the Utah State University Department of Physics.

Eric Addison

CONTENTS

LIST OF TABLES

LIST OF FIGURES

NOTATION

Binary Systems

m_i	Binary component masses, $i \in \{1, 2\}$
M	Binary total mass, $M = m_1 + m_2$
μ	Binary reduced mass
$\vec{r}$	Separation vector connecting m_1 and m_2
a	Semimajor axis
e	Orbital eccentricity
θ	True anomaly
i	Inclination angle
Ω_0	Longitude of the ascending node
ω_0	Argument of periapse
$\vec{L}$	Orbital angular momentum
E	Total binary energy

Relativity

c	Speed of light
G	Gravitational constant
$\vec{x}$	Three-vector
$\mathbf{x}$	Four-vector
γ	Lorentz factor

Conversions

$$\left[\frac{G}{c^2}\right] = \frac{m}{kg}$$

$$\left[\frac{G}{c^3}\right] = \frac{s}{kg}$$

ACRONYMS

GW	Gravitational Wave(s)
GR	General Relativity
CO	Compact Object
CSR	Compact Stellar Remnant
SMBH	Supermassive Black Hole
CBC	Compact Binary Coalescence
EMRI	Extreme Mass Ratio Inspiral
BEMRI	Binary Extreme Mass Ratio Inspiral
GC	Galactic Center
HVS	Hypervelocity Star

CHAPTER 1

INTRODUCTION

1.1 Astronomy, Astrophysics, and the Universe

We live in a universe that is paradoxically desolate and isolating, yet teeming with activity and full of mystery. The nearest astronomical object, our Moon, is an incredibly distant object by any terrestrial comparison ($\approx 385,000$ km away, or nearly 10 times the distance around the Earth), yet it creates the tides here on Earth, provides illumination in the dark of night, and varies its motion in predictable ways. The Sun, our star, is vastly further still, nearly 400 times more distant than the Moon, yet in addition to having been responsible for Earth's formation, it provides us with the warmth, light, and energy we require. The closest star after our Sun is an incomprehensible distance in any terms relative to our direct experiences, more than $250,000$ times further from Earth than the Sun, yet the stars twinkle in the night and slowly move across the sky if we care to watch for long enough.

As individuals, we can look out into a clear night sky and experience any range of emotions when faced with the display of the cosmos, be it the smallest amusement, the deepest wonder, or a disturbing sense of insignificance. Whatever we feel individually, on a collective level, the nature of the heavens has captivated us as a species for millennia. Historical evidence strongly suggests many ancient civilizations observed and studied the cosmos, including the ancient Egyptians, Greeks, Mesopotamians, Europeans, Indians, Chinese, and Central Americans. Astronomy is considered the oldest of the natural sciences for good reason: the universe presents its mysteries to us directly every night, and we need only to look up with an inquisitive eye to begin the exploration.

Astronomy consists of the study of celestial objects such as the stars, the planets, and their moons. While historically the study of the universe and its motions were closely linked with some form of religion or mythology, the careful study of astronomy has yielded a bounty of practical outcomes, such as advanced seaborne navigation, the modern GPS navigation system, and countless technology spinoffs. Astronomy, and by direct connection astrophysics (between which the defining line can be quite blurry), also satisfy a more profound human need. These disciplines seek to answer fundamental questions about the universe in which we exist, questions such as how did the universe begin, how did the universe get to be the way it is, is there other life in the universe, and are our circumstances unique in the universe. Through the process of studying the sky, we learn more about the cosmos that created us, the world that shelters us, and as we increase our collective knowledge, we learn more about what it means to be human.

1.2 Gravitational Waves: A New Observing Tool

For as long as we have been studying the sky, the overwhelming majority of our astronomical knowledge comes from observations of light, i.e., electromagnetic (EM) radiation. For the last several decades we have been observing extraterrestrial neutrinos as well; however, it is commonly stated in an anecdotal fashion that 99.9% of our knowledge about the universe comes from observations of light. There is a distinct advantage of light-based astronomical observations, which is that EM radiation is exceedingly easy to observe. Our own personal astronomical observation apparatuses (our eyes) are capable of detailed observations right out of the box with little or no calibration. We are able to extend our own capabilities with the aid of technology, reaching both deeper and more broadly into and across the EM spectrum. It is by this combination of biological and technological instrumentation that we have learned so much about the universe.

There are inherent limitations to EM astronomy associated with the nature of photons, and these limitations tend to stem from a common cause: photons interact strongly with matter. All matter is capable of absorbing and reradiating photons at a variety of wavelengths, and because of this, the light we observe when we point our instruments toward distant objects may have (probably has) been bumped, jostled, altered, and mucked up during its long journey from source to receiver. Any information photons carry about the matter that generated them becomes corrupted by later interactions. That is not to say we should not trust the information we gain from EM astronomy, but that the original encoded information becomes more difficult to interpret.

As an example, EM observations looking back toward the beginning of the universe are limited by the time when space (or rather the primordial plasma that filled all of space) became transparent to photons. Previous to this time the matter in the universe was so hot and dense that photons were not able to travel freely without being scattered by the dense cloud of subatomic particles. After the universe expanded and cooled, the protons and electrons that made up the plasma combined into neutral atoms and their density dropped sufficiently so photons could begin to travel long distances without being severely disturbed. This event is know as photon decoupling, which is estimated to have occurred approximately $380,000$ years after the Big Bang and produced the light we see now as the Cosmic Microwave Background. This is the oldest light we can observe. We are fundamentally unable to observe the universe with EM radiation prior to this time (Weinberg 1972).

Another example is the absorption and scattering of light due to the sparse dust that exists between stars in our galaxy. The absorption and scattering of light changes the apparent brightness of objects, and is known as extinction. It arises due to interstellar dust absorbing and scattering short wavelength light to a greater degree than long wavelength light. The preferential scattering of short wavelength light results in an effect known as interstellar reddening, and causes objects to appear redder than expected (Bennett et al. 2013).

The EM spectrum covers a wide range of energy levels encompassing many different physical phenomena; however, we are still limited by the fact that this is a single channel of information. There is another channel, free from the static of absorption and scattering that plagues the EM spectrum. Gravitational waves (GWs) are a fundamentally different channel of information, a channel to which we have only begun to listen. Where EM radiation is generated by accelerated electrical charges, GW radiation is generated by accelerated masses. When massive objects move, their gravitational field changes, and this change is propagated as GW radiation. GWs are propagating disturbances in gravity, often referred to poetically as ripples in the fabric of spacetime (Misner et al. 1973) in reference to their theoretical foundation in the General Theory of Relativity.

The utility of GWs as a tool for observing the cosmos is immense. Where EM radiation interacts strongly with atoms and can easily be absorbed, altered, and redirected, GWs have incredibly weak coupling to matter. Because of this, once GWs are generated they will propagate outwards from their source, essentially unimpeded by any intervening material, be it Earth's atmosphere, interstellar dust, or even the dense soupy plasma of the early universe. GW observations will allow us to probe the depths of the universe by carrying information about events that EM radiation cannot provide, such as:

- Details about the dynamical evolution of the massive stellar cores at the heart of supernova explosions.
- The merger of compact stellar remnants (CSR) such as neutron stars and white dwarfs.
- The presence of CSR binaries in our galaxy, too faint to see with light.
- The ellipticity of pulsars.
- Collisions of supermassive black holes at the cores of merging galaxies.
- Echoes from the Big Bang.

GWs are complementary to EM observations, and are certainly not a panacea for all of the gaps in our astronomical knowledge. GW detectors are not nearly as directional as EM instruments; an analogy between a GW detector and a microphone would be more accurate than with a telescope. The most crippling limitation of GW observations, precisely opposite from the EM situation, is exactly that virtue upon which the benefits of gravitational waves rest: GWs interact weakly with matter! We are necessarily constrained to construct our GW detectors from matter; and hence, our detectors are intrinsically not very sensitive to GWs. The nature of this problem will be discussed further in Section 1.4, though at this point, it suffices to say the development and construction of GW detectors is pushing the boundaries of technology and engineering and represents one of the most ambitious (and expensive) scientific endeavors in history.

1.3 A Short History of Gravitational Wave Science

As GWs are a consequence of changing gravitational fields, a brief discussion of gravitational theory follows. Currently, the most complete and well-tested theory of gravity is the General Theory of Relativity (GR), originally developed by Albert Einstein in a collection of four papers published in 1915-16 (Einstein 1916a). GR extends the previous dominant theory: Newton's universal law of gravitational attraction, also known as Newtonian gravity. Newton's theory (Brackenridge 1996) explains and quantifies a great number of physical phenomena including falling bodies, Earth's orbit around our Sun, and the tides caused by the Moon. Newtonian gravity has limitations, however. The first observed deviation from Newtonian gravity was an observed excess in the precession of the perihelion of the orbit of the planet Mercury around the Sun (Figure 1.1), noted by the French mathematician Urbain Le Verrier in 1859 (Le Verrier 1859). This precession could not be adequately explained by taking into account perturbations from all of the known planets using Newtonian gravity.

The papers introducing GR were published by Albert Einstein in 1915-16 (Einstein 1916a). GR is a geometric theory that interprets the motion of particles through space, not as the result of gravitational forces, but rather as a response to motion on the curved background of spacetime itself, whose shape (curvature) is influenced by the matter present within it. Newtonian gravity is the weak field and slow motion limit of GR, and GR is consistent with Einstein's previously established theory of special relativity. The use of GR to explain the precession of Mercury's perihelion was done by Einstein in 1916 (Einstein 1916b), which represented an instant triumph for the theory. This is the first of the three so-called classic tests of GR, the other two include measuring the deflection of starlight by the Sun's gravitational field, which was tested on the famous Eddington expedition in 1920 (Dyson et al. 1920), and measuring the gravitational red-shift of photons (Pound & Rebka 1959).

Einstein formally predicted the existence of GWs in 1918, three years after the publication of GR (Einstein 1918). The existence of GWs as a theoretical entity endured a turbulent period in the decades following their initial development, wrought with contro-

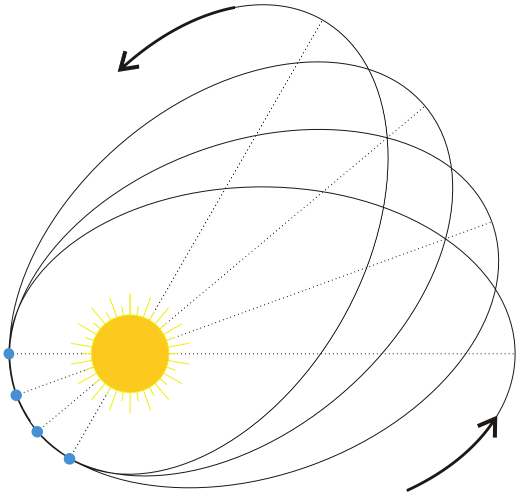

Figure 1.1: Perihelion precession. As a planet orbits the Sun, it's elliptical path will rotate due to various factors. Calculations of Mercury's perihelion precession were made very accurate by including effects from GR. Figure from http://en.wikipedia.org/wiki/Apsidal_precession

versy and skepticism (Kennefick 2007). Whether these waves traveled at the speed of light was an early point of contention, as the preeminent astrophysicist, Arthur Eddington (a noted GW skeptic) questioned what he saw as a presupposition by Einstein. Einstein had discovered three types of waves present in GR, only one of which was believed to carry energy. The other two waves were found to be merely coordinate artifacts; that is, they could be made to disappear in certain coordinate systems (Eddington 1922). Einstein's claims were eventually vindicated by Eddington, who independently showed the one energy carrying GW did, in fact, travel at the speed of light where the other two could take arbitrary velocities based on the choice of coordinates.

Though Einstein, Eddington and others had shown GWs could theoretically carry energy (shown mathematically, that is), whether this was a physical reality was the subject of a long debate. This debate was primarily centered around the question of whether an accelerated mass would experience a resistive force, or back reaction as it is often called, as it loses energy to GW radiation, and the closely related question of whether a pair of stars orbiting one another would eventually spiral inward as they radiate energy. The idea of inspiralling binary stars was uncomfortable for many physicists, as this implied there could be no stationary solution to the so-called two-body problem in GR. In addition to these troubles, Einstein himself prepared a paper with Nathan Rosen, which claimed to disprove the existence of GWs! The story of this paper is interesting in itself, as it was denied publication in the important journal, The Physical Review; however, Einsten eventually reversed his conclusion that GWs do not exist (Einstein & Rosen 1937). There is much more to the story of these early controversies, though it is clear the existence and nature of GWs were on uncertain footing.

The issue of whether GWs carry energy was eventually settled (more or less) by a simple thought experiment proposed by the famous physicist, Richard Feynman, at a 1957 conference in Chapel Hill, NC (Preskill & Thorne 1995), and popularized by the mathematician and cosmologist, Hermann Bondi (Bondi 1957), who was an early skeptic of GWs. The argument goes like this: consider Figure 1.2, showing two rings on a long rod, they are free to slide along, though not without friction. As will be discussed in Section 1.4, the effect of a GW is to alternately stretch and compress space; hence, stretching and compressing any matter present.

Since the material that makes up the rod is held together by internal electric forces, which oppose the stretching and shrinking, the effect of the GW is not as strong on the rod as it would be on two free particles. The rings, however, being subject to the same GW, will experience stretching and shrinking of the space between them, which is not bound by the same restoring forces. Because the rings are constrained to slide on the rod, the distance between them can stretch and shrink, reminiscent of the case of two free particles under the influence of a passing gravitational wave. Unlike the rod, there are no restraining forces between them, so the effect of the wave is to move the rings to a greater degree than the individual elements of the rod. The difference in these motions will cause the rings to slide across the rod, thus generating heat by friction. The energy that is transformed into heat must have come from somewhere, and since the ring-rod system is assumed to have been completely static before the arrival of the wave, the only sensible solution is the energy must have been imparted by the GW itself. This argument led to the general acceptance

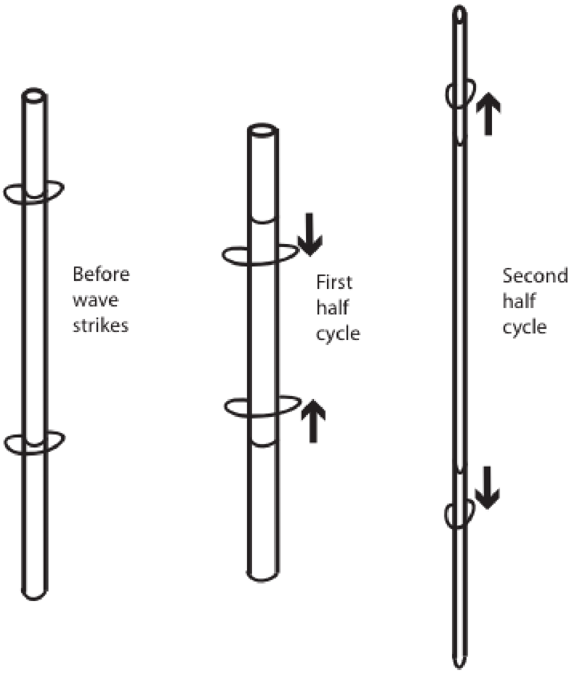

Figure 1.2: The Bondi thought experiment. As a GW passes the rod, the initial effect is to shorten and fatten the rod, and then to stretch and thin it. Internal forces cause the effect on the rod to be less pronounced than on the rings, which are free to slide along the rod. Because the rings move further than the rod stretches, friction is generated and must heat up the material. The heat energy must have been imparted from the passing wave. Figure from Kennefick (2007).

of the reality and energy transport of GWs.

In the decade following the understanding of GW energy transport, serious effort in the detection of GWs began. The principal pioneer in this field was Joseph Weber (1919 - 2000), who in the 1960s designed and constructed a series of resonant bar detectors. These detectors consisted of large aluminum cylinders, approximately 2 m long, 1 m in diameter, and massing roughly 4,200 kg with electrical sensors connected around the circumference that would detect vibrations in the bar. Just as with the bar in the Bondi thought experiment, a passing gravitational wave would stretch or compress the bar; when the gravitational wave passed, the restoring forces would pull the bar back to its original shape, exciting vibrational modes in the bar. The dominant modes of vibration would be the resonant modes defined by the geometry of the bar; for Weber's bars, there was a resonant vibration near 1660 Hz that could be detected by the sensors (Lindley 2005). In 1968, and again in 1970, Weber published papers claiming that he had indeed observed gravitational waves using these detectors (Weber 1968, 1969). Weber claimed to have observed not just a few, but hundreds of events over a two-year period. These claims were met with serious reservations, not least of which was that between the sensitivity of his instruments, the incredibly weak predicted strength of GWs, and the small estimated rate of occurrence for events capable of creating GWs in the frequency range to which his bars were sensitive, there was no plausible way the observed events were multiple GW signals. Many other concerns were raised, including possible manipulation of his data. Other research groups constructed bars of their own and observed nothing but noise. Though Weber steadfastly insisted his findings were real, his claims were all but dismissed by the larger physics community by the late 1970s (Collins 2010).

Bar detectors were not the only variety of early GW instruments. Robert Forward (1932 - 2002) proposed and built the first laser interferometric detector, which was operational by 1972 (Hawking & Israel 1989). The beam detector is based on the interference of laser beams traveling separate paths of initially equal length, similar to the famous Michelson-Morely interferometer used to investigate the existence of the ether in the early Twentieth Century. Forward's beam detector was operational during the same time period as several bar detectors, and while there were (spurious) detection claims made by the groups operating the bars, no corresponding detections were made by the beam detector (Forward 1978). Forward's work paved the way for the large-scale laser interferometers in use today, which present the most realistic possibility of GW detection yet.

1.4 The Nature of Gravitational Waves

As mentioned previously, GWs can be described as ripples in the fabric of spacetime. What does this mean? GWs are traveling disturbances to the geometry of spacetime. In many ways GWs are just like any other waves encountered in science: they are described by characteristic quantities such as wavelength, frequency, oscillation period, and propagation direction. The waves we consider, which are assumed to be small disturbances to the background geometry, travel at the speed of light, c. In this regime of small disturbances, arbitrarily complex waves can be constructed by combining plane waves of various frequencies and amplitudes. Like EM waves and waves on a guitar string, GWs are transverse. That is, the oscillation caused by a GW occurs in a direction perpendicular to the direction of wave propagation. Like other waves, GWs carry energy and angular momentum away from their source, and hence, can impart this energy and angular momentum to matter.

The physical effect of a passing GW, as will be developed mathematically in Chapter 2 and was briefly introduced in Section 1.3, is to alter the proper distance between two freely falling particles. A freely falling particle is one that is subject to no forces. Its trajectory is completely governed by the shape of the background spacetime curvature. An oscillatory wave that passes by a pair of particles will alternately stretch and shrink the distance between them. If we imagine ourselves sitting on one of these particles and surrounding ourselves with a ring of additional particles, then the proper distance between us and the surrounding particles will alternately stretch and shrink as a GW passes through the ring, depending on location. There are two possible manners in which the oscillation can occur, known as the polarizations of a GW. The polarizations are referred to as plus and cross, based on the shape of the oscillation. The GW effect for each polarization is shown in Figure 1.3, where the ring of particles is shown at times equal to $t = 0$, $T/4$, $T/2$, $3T/4$, and T, where T is the period of the GW. This picture sheds some light on the Bondi thought experiment. If we consider the rings on the rod to be the two test particles shown in green which are horizontally separated from the center, then the GW has the effect of alternately moving the rings further apart and closer together. Since the rod is stretching less (due to internal forces), the beads move along the rod and heat is generated by friction.

The GWs described here are predictions based on GR, but other theories of gravity exist with as many as six different polarization states (Will 2006). Alternate theories make different predictions about the nature of GWs, and so measuring and analyzing GWs is a strong test of GR (Arun & Pai 2013).

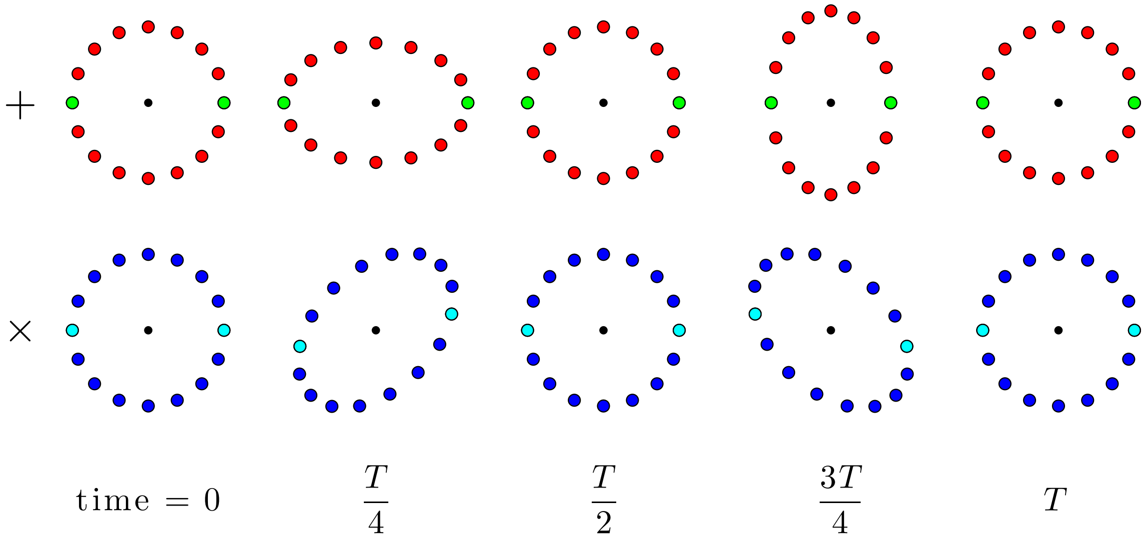

Figure 1.3: The effect of a GW passing through the page on a ring of test particles. The upper row shows the plus polarization, and the lower shows the cross polarization.

1.4.1 Indirect Evidence

Before discussing the efforts to detect the direct effects of GWs, there are several astronomical systems worth mentioning, which display behavior consistent with the loss of energy due to GW radiation.

In 1975, physicists Russell Hulse and Joseph Taylor discovered a remarkable binary star system, designated PSR B1913+16, consisting of a pulsar with a companion neutron star (Hulse & Taylor 1975), which are both very dense remnants from supernova explosions. The remarkable part of this system is it could be used to test the predictions of GR: as the stars orbit each other, they should slowly spiral inward as they lose energy to GW radiation (Taylor & Weisberg 1982). What makes this system different from others is the orbital period was already small enough (about 7.5 hours) so the change in period would be a measurable effect, with an initial predicted change of about -2.403×10^{-12} seconds per second. Binaries with larger periods have much slower changes, which are too small to observe. Figure 1.4 shows the result of more than 30 years of observing this system (Weisberg et al. 2010). The Figure shows the observational data with error bars, and the solid line shows the theoretical prediction by GR due to the emission of GW with no

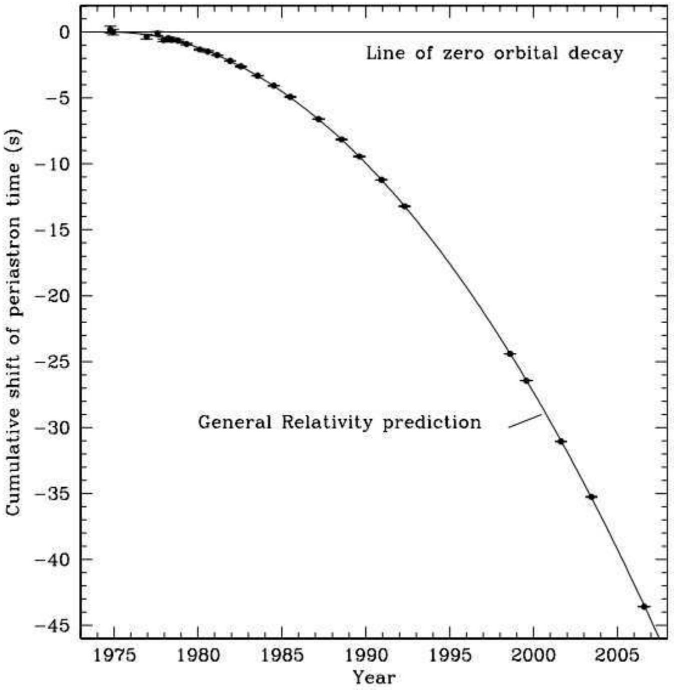

Figure 1.4: Decrease in orbital period of the Hulse-Taylor binary pulsar over 30 years of observation. The solid parabolic curve shows the predicted change from GR, and the data points are shown by the error bars, which are too small to see vertically. Figure from Weisberg et al. (2010).

substantive deviations from theoretical predictions, giving confidence to our expectations for the strength and effect of GW on astrophysical systems.

In 2003, the first and (so far) only double pulsar system, PSR J0737-3039, was discovered (Burgay et al. 2003). This system had an even smaller orbital period than the Hulse-Taylor binary pulsar. The two stars orbited each other every 2.5 hours. This system has allowed for precision tests of GR by matching observed parameter values to those predicted by GR. In a comparison of five parameters present when extending the equations of Keplerian orbital motion beyond Newtonian gravity, four of the five values observed for the double pulsar system agree with the GR predictions with an error of less than 1%. The fifth parameter agrees with an error of about 6% (Kramer & Wex 2009).

More recently, in 2011, there has been a discovery of a very short period white dwarf (WD) binary with an astonishingly small orbital period of about 12.75 minutes, designated SDSS J065133.33+284423.3 (Brown et al. 2011). This system is rather unusual. It is expected by the time a WD binary has shrunk to such a small size, one of the stars will have puffed up enough to fill its Roche lobe (see Chapter 5) and will be transferring matter to its companion. This type of interaction changes the dynamics of the system's evolution, making the effects from GR more difficult to observe. Since the WDs in this system are still detached (not transferring mass), the evolution will still be largely governed by GR, though the proximity of the stars has introduced some tidal deformation. This deformation has been explored and quantified by Benacquista (2011) so the additional orbital perturbations due to the deformation can be isolated from the effects of GR.

These three examples show that there is strong indirect evidence for both the existence of GWs, and the correctness of GR as the dominant theory of gravity. The extreme nature of these and other systems will continue to provide tests for gravitational theory, though the strongest test concerning GWs is that of direct detection.

1.4.2 Modern Detection Efforts

To date, there have been no direct experimental detections of GW radiation. That is, there has not yet been a sufficiently sensitive GW detector coupled with precise signal analysis techniques to unambiguously identify a GW signal distinct from the various sources of noise. The primary style of detector in use today is the laser interferometer, or beam detector. Modern ground-based detectors have laser arms that range in length from several hundred meters to a few kilometers. Current operational detectors include: the Laser Interferometer Gravitational Wave Observatories in Hanford, Washington (LHO) and Livingston, Louisianna (LLO) (collectively referred to as LIGO); the VIRGO detector in Italy; and the GEO600 in Germany. Near-term advanced ground-based detectors currently under construction include: advanced LIGO (aLIGO), a major technological upgrade to the existing LHO and LLO detectors (Virgo technology is also being upgraded); and KAGRA, an underground, cryogenically cooled interferometer under construction in Japan. A summary of important characteristics for several prominent current and planned GW detectors is presented in Table 1.

Table 1
Gravitational Wave Detectors

Name	Type	f_{peak} (Hz)	Sensitivity (10^{-23})	Reference
LHO	Ground, Beam	200	1.5	1
LLO	Ground, Beam	200	1.5	1
aLIGO[b]	Ground, Beam	200	0.3[a]	2
Virgo[c]	Ground, Beam	150	6	3
GEO600	Ground, Beam	600	15	4
KAGRA	Underground, Beam	90	0.3[a]	5
LISA	Space, Beam	0.008	0.4[a]	6,7
eLISA	Space, Beam	0.02	0.2[a]	7
PTA	Space, Pulsar Timing	10^{-8}	10^{10}	8

Notes. [a] Theoretical value.
[b] aLIGO is a technology upgrade to LHO and LLO, currently underway.
[c] The Virgo detector is also undergoing upgrades presently.
References. (1) LSC 2010b[1]; (2) LSC 2010a[2]; (3) Virgo/INFN 2011[3]; (4) GEO600 2006[4]; (5) ICRR 2010[5]; (6) Larson 2003[6]; (7) Amaro-Seoane et al. 2013; (8) Yardley et al. 2010.

The interferometer detectors consist of a laser beam split along two perpendicular arms, reflected off of suspended mirrors on either end, and rejoined to create an interference pattern. The armlengths are chosen to yield a fixed interference pattern. When a GW passes, the changing proper distance along the arms invokes a corresponding time-dependent shift in the interference pattern. A schematic of a laser interferometer, as well as a picture of the LLO are shown in Figure 1.5.

Ground-based interferometers are sensitive to relatively high-frequency GW events. Sources include supernova explosions, bumpy pulsars, and merging CSR binaries. The sensitive frequency range is primarily limited by the size of the interferometer arms: shorter arms are sensitive to shorter wavelengths (higher frequencies). For this reason, and for noise concerns, several space-based GW missions have been conceived (Gair et al. 2013). In space, many of the constraints that limit the size and sensitivity of ground-based detectors vanish,

---

[1] http://www.ligo.caltech.edu/~jzweizig/distribution/LSC_Data/.

[2] https://dcc.ligo.org/LIGO-T0900288/public.

[3] https://www.cascina.virgo.infn.it/DataAnalysis/Calibration/Sensitivity/.

[4] http://www.geo600.uni-hannover.de/geocurves/.

[5] http://gwcenter.icrr.u-tokyo.ac.jp/en/researcher/parameter.

[6] http://www.srl.caltech.edu/~shane/sensitivity/.

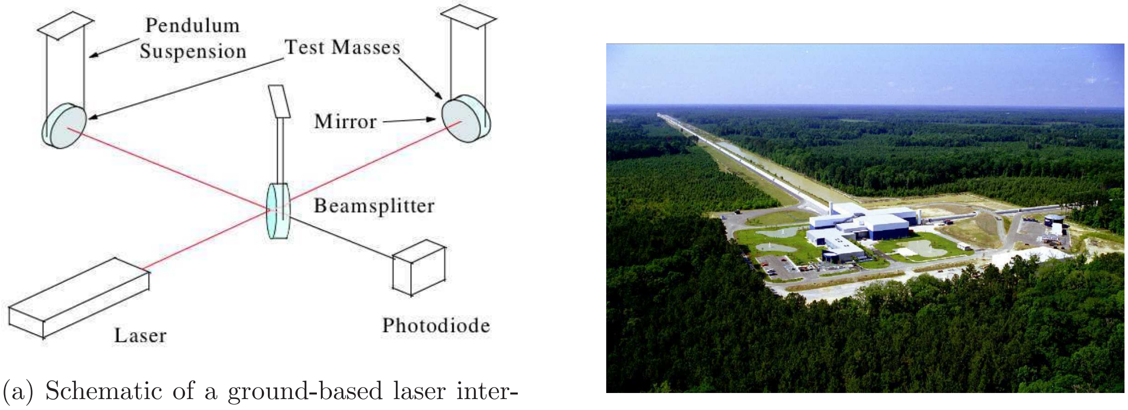

(a) Schematic of a ground-based laser interferometer like LIGO or Virgo.
Figure from Pitkin et al. (2011).

(b) The LIGO Livingston Observatory.
Figure from www.ligo.caltech.edu.

Figure 1.5: Ground-based laser interferometer detectors.

such as seismic noise and the need to maintain a high vacuum. These are replaced by new challenges, such as satellite position adjustments, beam spreading due to diffraction, and laser scattering off of interplanetary dust particles (Rubanu et al. 2009). The archetype for space-based GW observatories is a mission concept known as the Laser Interferometer Space Antenna (LISA). The standard LISA configuration specified a trio of cylindrical shaped satellites arranged in a triangular constellation that orbits the Sun lagging 20° behind the Earth. The distance between the LISA spacecraft was originally planned to be 5,000,000 km (Prince et al. 2006)! Such long arms would make LISA sensitive to frequencies in the millihertz range, where sources include close binary systems with orbital periods of tens of minutes, extreme mass ratio inspirals of stellar remnants into massive black holes, the coalescence of massive black holes, and GWs generated by the Big Bang.

The European Space Agency is currently developing a mission based on the LISA architecture, to be developed over the next decade, known as eLISA. The laser arms for eLISA will be only 1,000,000 km long and instead of forming a triangle of identical spacecraft, eLISA will contain one primary spacecraft at the vertex of the interferometer and two simpler craft as the endstations of the interferometer arms that maintain only two laser links, forming a V-shaped set of arms instead of a triangle (Amaro-Seoane et al. 2013). The eLISA mission boasts similar performance specifications to the original LISA design, with slightly reduced sensitivity and slightly higher frequency range. See Figure 1.6 for a schematic representation of the eLISA mission.

The GW spectrum is covered in the kHz region by ground-based detectors and the mHz region by the proposed space-based missions. Supermassive black hole binaries with masses of $10^8 M_\odot$ to $10^{10} M_\odot$ at the centers of merging galaxies are expected to produce loud GW signals in the nano-Hz region (Lee et al. 2011). Pulsar timing is a GW detection technique in the nanohertz band of the spectrum, and several pulsar timing efforts are currently underway, for example the Parkes Pulsar Timing Array (Manchester et al. 2013), the European Pulsar Timing Array (Ferdman et al. 2010), and the North American Nanohertz Observatory for Gravitational Waves (Demorest et al. 2013). A pulsar is a neutron star which spins rapidly and emits EM radiation in very focused beams, like a lighthouse signal. Pulsars can have rotation periods as short as several milliseconds and rotate very steadily, making them very stable clocks. The basic idea of using pulsar timing for GW detection is that the pulsar and Earth can be thought of as the two test masses in the interferometer setup, except here instead of interfering two laser beams, researchers search for deviations in the arrival time of the pulses. If a GW passes through the space separating the Earth and the pulsar, the pulses will arrive earlier and then later than expected in an alternating fashion. Pulsar timing research groups observe multiple pulsars at once (such a group is called a pulsar timing array), which reduces statistical uncertainty and can wash out other local perturbations to the pulse arrival times (such as the effect of the Earth's atmosphere).

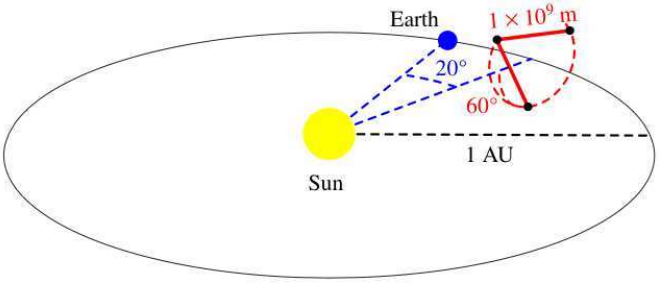

Figure 1.6: The proposed eLISA space-based GW observatory. eLISA will orbit the Sun at a distance of 1 AU, set 20° behind the Earth. Figure from Amaro-Seoane et al. (2013).

1.5 Gravitational Waves and Binary Systems

The connection between GWs with binary star systems should be apparent by now. Binaries present one of the simplest theoretical models for GW emission, and also stand as the primary prospect for GW detection because they are exceedingly common in astrophysics. Emissions from binary systems are of interest to both the low- and high-frequency GW communities. On the ground, observatories such as LIGO search for short GW bursts from the last stages of the inspiral and merger of a CSR binary system, while space-based missions such as eLISA will easily be able to detect the persistent hum of compact binary systems, largely white dwarf binaries, that are nowhere near merger and radiate at very steady frequencies. In fact, eLISA is expected to see so many binaries that they will form a constant source of background noise! Since binaries constitute the bread and butter of GW detection, a substantial amount of research has been done investigating the science that can be accomplished using GW observations of binary systems. The content of this dissertation adds to that body of work, developing new frameworks for interpreting astrophysical results that will be useful once GW observations become readily available.

1.6 The Future of Gravitational Wave Science

We currently sit at the verge of direct GW detections. The advanced LIGO detectors are expected to come online later this decade, the LISA pathfinder mission to test the core eLISA technology is scheduled to launch next year (2015), and pulsar timing array efforts are ongoing, but widely expected to make their first detections before the end of the decade. Plans for future detectors, such as the Einstein Telescope with exquisite sensitivity (Hild et al. 2008), are currently being developed, and even more speculative technology is being talked about for the distant future, such as atom interferometry (Dimopoulos et al. 2009). It has been said that we belong to the last generation of scientists who will not know GW observations as commonplace. Once GW observations become routine, the GW community will shift much of its focus from data analysis and instrumentation toward the astrophysical questions that GWs promised to help explore in the first place: what happens when neutron stars merge together, how well do we understand gravity in its strongest forms, what can we still learn about the early universe, and what else is out there that we have not had the imagination to dream of yet. The promises of GWs are mighty, and the fruits of the labor of a century of science are just around the corner.

1.7 This Document

The work in this dissertation represents my research in GW astrophysics: studying ways in which GW observations will enhance our knowledge of astrophysical phenomena and vice-versa. Specifically, this research deals with GW astrophysics applied to compact binary systems. The remainder of this document will be arranged as follows: Chapters 2 and 3 develop foundational material relating to gravitational wave emissions and binary systems necessary for my research.

Chapter 4 contains my first research project exploring interactions between CO binaries and SMBHs. In this project we show for the extreme mass ratios (EMRIs) created by tidal disruption of a binary by the SMBH, orbital eccentricity in the LISA sensitivity band is significantly smaller than for single star capture EMRIs, though the merging eccentricity is found to be larger than estimated in previous studies. We also explore the altered parameters of binaries that survive the encounter, finding on average, their merger lifetime has been shortened, leading to a net increase to the predicted BH-BH merger rate.

In Chapter 5, my second project is presented, which develops a novel method for estimating the radius of accretion discs in cataclysmic variable systems with multi-messenger astronomy. We describe and test this method with both simulated and observational data for the compact binary system AM CVn; and in both cases, we are able to estimate the disc radius with an error of less than 1%.

Chapter 6 summarizes future directions for this work. The simulation codes used to perform this research are available online at

- https://github.com/ericaddison/Binary-SMBH-Encounter-Simulation, and
- https://github.com/ericaddison/LightCurveSim.

CHAPTER 2

GRAVITATIONAL WAVES

2.1 What Are Gravitational Waves?

Waves are a familiar phenomenon in science, and fundamental to many disciplines in physics. Waves are prominent in electromagnetism, quantum mechanics, geophysics, fluid mechanics, and most other subfields of physics. Waves form the foundation of Fourier analysis, a powerful mathematical tool for analyzing signals and solving differential equations. It should come as no surprise, then, that wave phenomena exist in the field of gravitational physics.

Gravitational waves (hereafter GWs) emerge mathematically as a natural consequence of Einstein's General Theory of Relativity (GR). GWs are present in other theories of gravity as well; however, here I will proceed solely in the context of GR. GWs transmit information about the changing state of the gravitational fields produced by accelerated masses, and exist as propagating disturbances to the spacetime metric. In the weak field regime, where variations of the gravitational field are small and masses move slowly compared to c, a GW can be described mathematically as a small scale perturbation to a background spacetime metric (taken here to be flat):

$$g_{\alpha\beta} = \eta_{\alpha\beta} + h_{\alpha\beta}, \tag{2.1}$$

where $\eta_{\alpha\beta}$ is the flat Minkowski metric $\eta_{\alpha\beta} = \mathrm{diag}(-1, 1, 1, 1)$, and $h_{\alpha\beta}$ is the perturbation with each element satisfying $|h_{\alpha\beta}| \ll 1$. It is from this assumption that the weak-field, or linearized Einstein field Equations are derived, which lead to many interesting results including the admittance of wave-like solutions. The utility of GWs, besides providing a testing ground for GR, will be new and unprecedented astrophysical observations, providing a better understanding of compact systems dominated by gravity, our galaxy, our universe, and the nature of physical law.

This chapter presents the basic concepts of gravitational waves in the context of General Relativity, enough to provide a proper basis for my research. The material presented here comes primarily from texts on GR and review papers: (Maggiore 2008; Sathyaprakash & Schutz 2009; Schutz 2009). Calculations performed in this chapter will be done in geometricized units with $G = c = 1$.

2.2 Conventions

The notation and conventions used in this Section follow closely to those in Schutz (2009). The conversion factors that bring time and mass quantities into units of meters are

$$[c] = \frac{m}{s} \qquad \text{and} \qquad \left[\frac{G}{c^2}\right] = \frac{m}{kg}. \tag{2.2}$$

For example, the mass of the Sun is converted to meters in geometricized units as $M_\odot = \left(2 \times 10^{30}\ \text{kg}\right)\left(G/c^2\right) \approx 1500$ m. In this way distances, times, and masses can be manipulated together under the common units of meters.

The Einstein summation notation is used where repeated indices indicate summation on that variable, i.e.,

$$v^\alpha u_\alpha \equiv \sum_{\alpha=0}^{3} v^\alpha u_\alpha. \tag{2.3}$$

In general, Greek indices $(\alpha, \beta, \mu, \nu$ etc.) imply four total dimensions, while Latin indices (i, j, k) indicate only three, typically the spatial dimensions. Vectors will be denoted in boldface for four-vectors, e.g., $\mathbf{k}$, while three-vectors will have an over-arrow, e.g., $\vec{k}$.

Indices on vectors and tensors will be raised and lowered using the metric $g_{\alpha\beta}$ unless otherwise noted for approximation purposes. For example, $v_\alpha = g_{\alpha\beta} v^\beta$ and $T^{\alpha\beta} = T_{\mu\nu} g^{\mu\alpha} g^{\nu\beta}$, where $g^{\alpha\beta}$ is the inverse of the metric tensor. The metric is chosen with a signature of diag(-1,+1,+1,+1), i.e., with a negative timelike dimension. This choice can vary between texts, and more information can be found in Misner et al. (1973).

Standard partial differentiation is denoted with the comma notation

$$\frac{\partial v^\alpha}{\partial x^\beta} \equiv v^\alpha{}_{,\beta}, \text{ and} \tag{2.4}$$

$$\frac{\partial u^\alpha}{\partial x_\beta} \equiv u^{\alpha,\beta}. \tag{2.5}$$

The covariant derivative is signified with the del notation, i.e.,

$$\nabla_\beta v^\alpha \equiv v^\alpha{}_{,\beta} + v^\mu \Gamma^\alpha{}_{\mu\beta}, \tag{2.6}$$

where $\Gamma^\alpha{}_{,\mu\beta}$ is the Christoffel symbol associated with the metric $g_{\alpha\beta}$. Equation 2.6 gives the component of the covariant derivative in the direction of $\partial/\partial x^\beta$; the directional covariant derivative in the direction of a unit vector U^α is given simply as in the standard calculus fashion:

$$\nabla_U v^\alpha = U^\beta \nabla_\beta v^\alpha. \tag{2.7}$$

2.3 Linearized GR

In order to simplify the highly nonlinear equations that describe GR, a set of linearized equations are developed that neglect powers of small quantities higher than first order.

Begin with a coordinate transformation of the form

$$x^{\alpha'} = x^\alpha + \xi^\alpha(x^\beta), \tag{2.8}$$

which transforms from the unprimed to the primed coordinate system, where x^α are inertial coordinates and $\xi^\alpha(x^\beta)$ is a slowly varying transformation vector valued function of spacetime position in the inertial frame x^α, i.e., $|\xi^\alpha{}_{,\beta}| \ll 1$. The transformation tensor $\Lambda^{\alpha'}{}_\beta$ then has the form

$$\Lambda^{\alpha'}{}_\beta = \frac{\partial x^{\alpha'}}{\partial x^\beta} = \delta^\alpha{}_\beta + \xi^\alpha{}_{,\beta}. \tag{2.9}$$

The inverse transformation $\Lambda^\alpha{}_{\beta'}$ is simply

$$\Lambda^\alpha{}_{\beta'} = \frac{\partial x^\alpha}{\partial x^{\beta'}} = \left(\frac{\partial x^{\beta'}}{\partial x^\alpha}\right)^{-1} \approx \delta^\alpha{}_\beta - \xi^\alpha{}_{,\beta}, \tag{2.10}$$

where the approximation is valid to first order in $\xi^\alpha{}_{,\beta}$.

Applying this transformation to the perturbed metric (equation 2.1), we have

$$
\begin{aligned}
g_{\alpha'\beta'} &= \Lambda^{\mu}{}_{\alpha'}\Lambda^{\nu}{}_{\beta'}g_{\mu\nu} && (2.11)\\
&= \Lambda^{\mu}{}_{\alpha'}\Lambda^{\nu}{}_{\beta'}(\eta_{\mu\nu} + h_{\mu\nu}) && (2.12)\\
&= (\delta^{\mu}{}_{\alpha} - \xi^{\mu}{}_{,\alpha})(\delta^{\nu}{}_{\beta} - \xi^{\nu}{}_{,\beta})(\eta_{\mu\nu} + h_{\mu\nu}) && (2.13)\\
&= \eta_{\alpha\beta} - \eta_{\alpha\nu}\xi^{\nu}{}_{,\beta} - \eta_{\mu\beta}\xi^{\mu}{}_{,\alpha} + h_{\alpha\beta} + \mathcal{O}(\xi^2) + \mathcal{O}(h^2) && (2.14)\\
&= \eta_{\alpha\beta} - \xi_{\alpha,\beta} - \xi_{\beta,\alpha} + h_{\alpha\beta} + \mathcal{O}(\xi^2) + \mathcal{O}(h^2) && (2.15)\\
&\approx \eta_{\alpha\beta} - \xi_{\alpha,\beta} - \xi_{\beta,\alpha} + h_{\alpha\beta}, && (2.16)
\end{aligned}
$$

where we define $\xi_\alpha = \eta_{\alpha\beta}\xi^\beta$. The approximation is valid to first order in the small quantities $|\xi^{\alpha}{}_{,\beta}|$ and $|h_{\alpha\beta}|$. We can now identify that in the primed coordinates, the perturbation $h_{\alpha\beta}$ has transformed to

$$h_{\alpha\beta} \to h_{\alpha\beta} - \xi_{\alpha,\beta} - \xi_{\beta,\alpha}, \tag{2.17}$$

and remains a small quantity. This sort of transformation is known as a gauge transformation, and allows us to simplify the Einstein Equations by a clever choice of the vector, ξ^α. A gauge transformation takes advantage of the freedom to choose a coordinate system, which makes calculations simpler.

The Einstein Equations are a set of ten nonlinear coupled, partial differential equations, written as

$$G^{\mu\nu} = 8\pi T^{\mu\nu}, \tag{2.18}$$

where $G^{\mu\nu}$ is called the Einstein tensor, constructed from combinations of second derivatives of the metric, and $T^{\mu\nu}$ is the stress energy tensor, which characterizes all the matter and energy present. This is the second order differential equation which dictates the dynamical evolution of spacetime. The Riemann curvature tensor, $R_{\alpha\beta\mu\nu}$, quantifies the curvature of spacetime, in one sense by quantifying the change in a vector after parallel transporting it around an infinitesimally small closed loop, and in another by determining the deviation of initially parallel lines. The Riemann tensor is constructed from derivatives of the metric. We are interested in the Riemann tensor specifically because the Einstein tensor is constructed from it. We can now compute the Riemann curvature tensor from our perturbed metric as

$$R_{\alpha\beta\mu\nu} = \frac{1}{2}\left(g_{\alpha\nu,\beta\mu} - g_{\alpha\mu,\beta\nu} + g_{\beta\mu,\alpha\nu} - g_{\beta\nu,\alpha\mu}\right) \tag{2.19}$$

$$= \frac{1}{2}\left(h_{\alpha\nu,\beta\mu} - h_{\alpha\mu,\beta\nu} + h_{\beta\mu,\alpha\nu} - h_{\beta\nu,\alpha\mu}\right). \tag{2.20}$$

Equation 2.20 is gauge invariant to first order, as any gauge transformation would introduce a collection of ξ_α derivative terms as in Equation 2.17, which exactly cancel at first order.

We previously defined the lowered index vector $\xi_\alpha = \eta_{\alpha\beta}\xi^\beta$. In a similar manner we can adopt the index raising convention of

$$h^{\mu}{}_{\beta} = \eta^{\mu\alpha}h_{\alpha\beta}, \text{ and} \tag{2.21}$$

$$h^{\mu\nu} = \eta^{\nu\beta}h^{\mu}{}_{\beta}. \tag{2.22}$$

These operations are simply the first-order terms of index raising on $h_{\alpha\beta}$ using the full metric $g^{\alpha\beta}$. With this convention, we can also define the trace of $h_{\alpha\beta}$ as

$$h = h^{\alpha}{}_{\alpha}, \tag{2.23}$$

and introduce the trace reversed version of $h_{\alpha\beta}$,

$$\bar{h}_{\alpha\beta} = h_{\alpha\beta} - \frac{1}{2}\eta_{\alpha\beta}h. \tag{2.24}$$

The trace reversed $\bar{h}_{\alpha\beta}$ has the useful property that

$$\bar{h} = \bar{h}^{\alpha}{}_{\alpha} \tag{2.25}$$

$$= \eta^{\alpha\mu}\bar{h}_{\mu\alpha} \tag{2.26}$$

$$= \eta^{\alpha\mu}h_{\mu\alpha} - \frac{1}{2}\eta^{\alpha\mu}\eta_{\alpha\mu}h \tag{2.27}$$

$$= h - 2h = -h. \tag{2.28}$$

Next, compute the Ricci tensor and scalar in order to find the Einstein tensor:

$$R_{\alpha\beta} = {R^{\mu}}_{\alpha\mu\beta} \tag{2.29}$$

$$= \eta^{\mu\nu} R_{\nu\alpha\mu\beta} + \mathcal{O}(h^2) \tag{2.30}$$

$$\approx \eta^{\mu\nu} \frac{1}{2} \left(h_{\nu\beta,\alpha\mu} - h_{\nu\mu,\alpha\beta} + h_{\alpha\mu,\nu\beta} - h_{\alpha\beta,\nu\mu} \right) \tag{2.31}$$

$$= \frac{1}{2} ({h_{\mu\beta,\alpha}}^{,\mu} - {h^{\mu}}_{\mu,\alpha\beta} + {h_{\alpha\mu,\beta}}^{,\mu} - {h_{\alpha\beta,\mu}}^{,\mu}) \tag{2.32}$$

$$= \frac{1}{2} \left({\bar{h}_{\mu\beta,\alpha}}^{,\mu} + \frac{1}{2}\eta_{\mu\beta} {h_{,\alpha}}^{,\mu} - h_{,\alpha\beta} + {\bar{h}_{\alpha\mu,\beta}}^{,\mu} + \frac{1}{2}\eta_{\alpha\mu} {h_{,\beta}}^{,\mu} - {\bar{h}_{\alpha\beta,\mu}}^{,\mu} - \frac{1}{2}\eta_{\alpha\beta} {h_{,\mu}}^{,\mu} \right) \tag{2.33}$$

$$= \frac{1}{2} \left({\bar{h}_{\mu\beta,\alpha}}^{,\mu} + {\bar{h}_{\alpha\mu,\beta}}^{,\mu} - {\bar{h}_{\alpha\beta,\mu}}^{,\mu} - \frac{1}{2}\eta_{\alpha\beta} {h_{,\mu}}^{,\mu} \right), \tag{2.34}$$

and

$$R \approx \eta^{\alpha\beta} R_{\alpha\beta}, \tag{2.35}$$

$$= \eta^{\alpha\beta} \frac{1}{2} \left({\bar{h}_{\mu\beta,\alpha}}^{,\mu} + {\bar{h}_{\alpha\mu,\beta}}^{,\mu} - {\bar{h}_{\alpha\beta,\mu}}^{,\mu} - \frac{1}{2}\eta_{\alpha\beta} {h_{,\mu}}^{,\mu} \right) \tag{2.36}$$

$$= \frac{1}{2} \left(2{\bar{h}_{\mu\alpha}}{}^{,\mu\alpha} - {h_{,\mu}}^{,\mu} \right), \tag{2.37}$$

with the approximations correct to first order in $|h_{\alpha\beta}|$. The Einstein tensor, $G_{\alpha\beta}$, is then (again correct to first order)

$$G_{\alpha\beta} = R_{\alpha\beta} - \frac{1}{2}\eta_{\alpha\beta} R, \tag{2.38}$$

$$\approx \frac{1}{2} \left[\left({\bar{h}_{\mu\beta,\alpha}}^{,\mu} + {\bar{h}_{\alpha\mu,\beta}}^{,\mu} - {\bar{h}_{\alpha\beta,\mu}}^{,\mu} - \frac{1}{2}\eta_{\alpha\beta} {h_{,\mu}}^{,\mu} \right) - \frac{1}{2}\eta_{\alpha\beta} \left(2{\bar{h}_{\mu\nu}}{}^{,\mu\nu} - {h_{,\mu}}^{,\mu} \right) \right] \tag{2.39}$$

$$= -\frac{1}{2} \left[{\bar{h}_{\alpha\beta,\mu}}^{,\mu} + \eta_{\alpha\beta} {\bar{h}_{\mu\nu}}{}^{,\mu\nu} - {\bar{h}_{\mu\beta,\alpha}}^{,\mu} - {\bar{h}_{\alpha\mu,\beta}}^{,\mu} \right]. \tag{2.40}$$

We now move into the harmonic gauge, which has the property that

$${\bar{h}^{\mu\nu}}{}_{,\nu}^{\;(\mathrm{NEW})} = 0, \tag{2.41}$$

and is achieved when ξ^μ satisfies

$$\Box\xi^\mu = \xi^{\mu,\nu}{}_{,\nu} = \bar{h}^{\mu\nu}{}_{,\nu}^{\;(\mathrm{OLD})}\,, \tag{2.42}$$

where the box, $\Box$, denotes the D'Alembertian operator or wave operator with our metric signature: $\Box \equiv \eta^{\alpha\beta}\partial_\alpha\partial_\beta$. The superscripts (OLD) and (NEW) are shown here to explicitly identify $h^{\alpha\beta}$ before and after the gauge transformation, and from now on it will be assumed the h's are in the new transformed coordinates.

This choice of constraint on $h_{\alpha\beta}$ uses up some (but not all) of the gauge freedom that we have available in the gauge transformation. This is analogous to choosing the Lorenz gauge in electromagnetism when the gauge condition $\nabla\cdot\vec{A} = -(1/c^2)\partial\Phi/\partial t$ is chosen so the magnetic vector potential, $\vec{A}$, and the electric potential, Φ, each satisfy an inhomogeneous wave equation.

In this gauge, the Einstein tensor quickly reduces to

$$G^{\alpha\beta} = -\frac{1}{2}\Box\bar{h}^{\alpha\beta}, \tag{2.43}$$

and the Einstein Equations then read

$$G^{\alpha\beta} = 8\pi T^{\alpha\beta}, \tag{2.44}$$

$$\Rightarrow \Box\bar{h}^{\alpha\beta} = -16\pi T^{\alpha\beta}. \tag{2.45}$$

These are the so-called weak field Einstein Equations in the harmonic gauge, since they were produced under the assumption that the perturbation to the background metric is weak. They are also known as the linearized Einstein Equations (in the harmonic gauge), or linearized GR, because at each step, terms were only kept to first order in small parameters. It is important to remind ourselves of the gauge these equations belong to, as the additional gauge condition (equation 2.41) is required for any solution, $h^{\alpha\beta}$. These are the equations that will be used in subsequent sections.

2.4 Propagation of Gravitational Waves

We will now use the linearized Einstein Equations to explore the propagation of an oscillatory metric disturbance (a GW) in vacuum. The equations then read

$$\begin{cases} \Box \bar{h}^{\alpha\beta} = \left(-\dfrac{\partial^2}{\partial t^2} + \nabla^2\right) \bar{h}^{\alpha\beta} = 0, \\ \bar{h}^{\alpha\beta}{}_{,\beta} = 0. \end{cases} \tag{2.46}$$

If we assume a complex oscillatory solution representing plane waves of the form

$$\bar{h}^{\alpha\beta} = A^{\alpha\beta} \exp(ik_\alpha x^\alpha), \tag{2.47}$$

where $A^{\alpha\beta}$ is complex, and in the end we will take the real part of the solution, then we can insert into the Einstein Equations to find

$$\Box \bar{h}^{\alpha\beta} = \bar{h}^{\alpha\beta,\nu}{}_{,\nu} \tag{2.48}$$

$$= \eta^{\mu\nu} \bar{h}^{\alpha\beta}{}_{,\mu\nu} \tag{2.49}$$

$$= -\eta^{\mu\nu} k_\mu k_\nu \bar{h}^{\alpha\beta} \tag{2.50}$$

$$= -k^\nu k_\nu \bar{h}^{\alpha\beta} = 0. \tag{2.51}$$

Since $\bar{h}^{\alpha\beta}$ is not identically zero (or else we have no GW), this equation can only hold if $k^\nu k_\nu = 0$, i.e., k^α is a null vector. This implies the GW travels on a null surface; that is, the surfaces of constant phase are null, and therefore move at the speed of light. This follows from satisfying the nullity condition with

$$\omega^2 = |\vec{k}|^2, \tag{2.52}$$

where $\omega = k^0$ and $\vec{k} = k^i$ with $i = 1, 2, 3$, so the wave four-vector is $\mathbf{k} = (\omega, \vec{k})$. This is the dispersion relation for vacuum GWs, which immediately results in both phase and group velocities of 1 (the speed of light in geometricized units). Furthermore, by imposing the harmonic gauge property (equation 2.41), we find

$$\bar{h}^{\alpha\beta}{}_{,\beta} = A^{\alpha\beta} i k_\beta \exp(i k_\nu x^\nu) = 0 \Rightarrow A^{\alpha\beta} k_\beta = 0, \tag{2.53}$$

which shows $A^{\alpha\beta}$ (amplitude-polarization tensor) is orthogonal to k_β (propagation vector); and therefore, the GW $\bar{h}^{\alpha\beta}$ is transverse to the direction of propagation.

Here it has been shown Equation 2.47 is a solution to the vacuum linearized Einstein Equations when the propagation vector k^α is null, and that the amplitude tensor is orthogonal to $\mathbf{k}$. Of course, from this plane-wave solution, it is possible to construct arbitrary solutions through superposition.

So far, we have used the condition of the harmonic gauge (equation 2.41), but have not uniquely determined a choice of the gauge vector, ξ_α. We can choose a gauge vector while remaining in the harmonic gauge of the form

$$\xi_\alpha = B_\alpha \exp(i k_\nu x^\nu), \tag{2.54}$$

where k_ν is the same propagation vector as in $\bar{h}^{\alpha\beta}$, and B^μ is a constant (complex) vector. The nullity of k_ν shows this choice of gauge vector leaves us in the harmonic gauge by enforcing the gauge requirement of $\Box\xi^\alpha = \bar{h}^{\alpha\beta}{}_{,\beta} = 0$. Using this gauge vector and applying Equation 2.17 results in a new GW with (after cancellation of exponential terms)

$$A^{\alpha\beta} \rightarrow A^{\alpha\beta} - i B_\alpha k_\beta - i B_\beta k_\alpha + i \eta_{\alpha\beta} B^\mu k_\mu. \tag{2.55}$$

The remaining gauge freedom allows the following convenient conditions to be imposed on $A^{\alpha\beta}$:

$$A^\mu{}_\mu = 0 \qquad \text{and} \qquad A_{\alpha\beta} U^\beta = 0, \tag{2.56}$$

where U^α is any fixed timelike unit vector. These conditions simplify the form of $A^{\alpha\beta}$, and B_α becomes fixed with the form

$$B_\alpha = \frac{i}{k_\beta U^\beta}\left[\frac{k_\alpha}{2k_\beta U^\beta}\left(\frac{1}{2}A^\mu{}_\mu - U^\mu U^\nu A_{\mu\nu}\right) + \frac{1}{2}U_\alpha A^\mu{}_\mu - A_{\alpha\beta}U^\beta\right]. \tag{2.57}$$

To see why U^α is chosen to be timelike, note that since a timelike vector and a null vector cannot be orthogonal, the quantity $k_\beta U^\beta \neq 0$, and we can never run into divide-by-zero issues, even when integrating over all $\mathbf{k}$. That these conditions hold for general $\bar{h}_{\alpha\beta}$, and not just plane-wave solutions is proved explicitly in Wald (1984).

By choosing $\mathbf{U} = (1, 0, 0, 0)$, and setting coordinates such that the wave is propagating in the z direction, i.e., $\mathbf{k} = (\omega, 0, 0, \omega)$, the following components of $A_{\alpha\beta}$ can be determined:

$$A_{\alpha 0} = A_{0\alpha} = 0, \tag{2.58}$$

$$A_{z\alpha} = A_{\alpha z} = 0, \tag{2.59}$$

$$A_{xx} = -A_{yy}, \text{ and} \tag{2.60}$$

$$A_{xy} = A_{yx} \text{ (due to symmetry)}. \tag{2.61}$$

This choice of B_α and U^α defines the Transverse-Traceless gauge: traceless because of Equation 2.56 and transverse because of Equation 2.59. In this gauge, the amplitude-polarization tensor, $A_{\alpha\beta}$, looks like

$$(A^{TT}_{\alpha\beta}) = \begin{pmatrix} 0 & 0 & 0 & 0 \\ 0 & A_{xx} & A_{xy} & 0 \\ 0 & A_{xy} & -A_{xx} & 0 \\ 0 & 0 & 0 & 0 \end{pmatrix}. \tag{2.62}$$

This can be split into a sum of two terms, each proportional to a polarization tensor:

$$(A^{TT}_{\alpha\beta}) = A_+ \boldsymbol{\epsilon}_+ + A_\times \boldsymbol{\epsilon}_\times, \tag{2.63}$$

where $A_+ = A_{xx}$, $A_\times = A_{xy}$, and

$$\boldsymbol{\epsilon}_+ = \hat{x} \otimes \hat{x} - \hat{y} \otimes \hat{y} = \begin{pmatrix} 0 & 0 & 0 & 0 \\ 0 & 1 & 0 & 0 \\ 0 & 0 & -1 & 0 \\ 0 & 0 & 0 & 0 \end{pmatrix} \quad , \quad \boldsymbol{\epsilon}_\times = \hat{x} \otimes \hat{y} + \hat{y} \otimes \hat{x} = \begin{pmatrix} 0 & 0 & 0 & 0 \\ 0 & 0 & 1 & 0 \\ 0 & 1 & 0 & 0 \\ 0 & 0 & 0 & 0 \end{pmatrix} . \tag{2.64}$$

Here the polarization tensors have been given subscripts + and ×, referred to as the plus and cross polarizations for reasons discussed below. We have found there exists a gauge in which only two independent amplitude terms remain, which can be split into two independent polarizations, and the plane GW can now be written as

$$h^{TT}_{\alpha\beta} = \mathcal{R}[(A_+ \boldsymbol{\epsilon}_+ + A_\times \boldsymbol{\epsilon}_\times) \exp(ik_\mu x^\mu)], \tag{2.65}$$

where $\mathcal{R}$ denotes the real part. We can build up arbitrary waves using Fourier superposition, i.e.,

$$h^{TT}_{\alpha\beta} \to \mathcal{R}\left[\int A^{TT}_{\alpha\beta}(\vec{k}) \exp(ik_\mu x^\mu) d\vec{k}\right], \tag{2.66}$$

where $A^{TT}_{\alpha\beta}(\vec{k})$ is the Fourier decomposition of the general wave, and $\vec{k}$ is the spatial part of the wave vector satisfying the dispersion relation in Equation 2.52.

2.5 Generation of Gravitational Waves

Now that the propagation of GWs in vacuum has been established, we can turn to their generation. The general solution to the sourced Einstein Equations (Equation 2.45) is given by integration of the source along with the retarded Green's function for the wave equation (Jackson 1998):

$$\bar{h}^{\alpha\beta}(\mathbf{x}) = -16\pi \int G_{\text{ret}}(\mathbf{x}; \mathbf{x}') T^{\alpha\beta}(\mathbf{x}') d\mathbf{x}', \tag{2.67}$$

where $\mathbf{x} = (t, \vec{x})$, $\vec{x}$ is a position three-vector, the integral is taken over the region where the source $T^{\alpha\beta} \neq 0$, and the Green's function $G_{\text{ret}}(\mathbf{x};\mathbf{x}')$ is

$$G_{\text{ret}}(\mathbf{x};\mathbf{x}') = G_{\text{ret}}(t,\vec{x};t',\vec{x}') = -\frac{\delta\left(t' - [t - |\vec{x} - \vec{x}'|]\right)}{4\pi|\vec{x} - \vec{x}'|}. \tag{2.68}$$

The retarded Green's function describes the observation at time, t, and location, $\vec{x}$, of the effect from an impulsive source located at position, $\vec{x}'$, occurring at time, t'. The time, t', is known as the retarded time because it is the time in the past at which an event occurs such that it will be observed at time, t, at a distance $|\vec{x} - \vec{x}'|$.

The integral in Equation 2.67 can now be written as

$$\bar{h}^{\alpha\beta}(t,\vec{x}) = 4\int \frac{T^{\alpha\beta}(t',\vec{x}')}{|\vec{x} - \vec{x}'|} d\vec{x}', \tag{2.69}$$

where $t' = t - |\vec{x} - \vec{x}'|$ is the retarded time. Now impose the condition that the observation occurs at a distance very large compared to the size of the source region, i.e., $\frac{|\vec{x}'|}{|\vec{x}|} \ll 1$, and the wavelength is long compared to the source region, $\frac{|\vec{x}'|}{\lambda} \ll 1$. If we write $|\vec{x}| = R$, this allows us to write $\bar{h}^{\alpha\beta}(t,\vec{x})$ to first order in $|\vec{x}'|/R$ as

$$\bar{h}^{\alpha\beta}(t,\vec{x}) \approx \frac{4}{R}\int T^{\alpha\beta}(t - R,\vec{x}')d\vec{x}'. \tag{2.70}$$

It should be noted here that the integration in Equations 2.67, 2.69, and 2.70 are only appropriate for Cartesian coordinates, and hence, Cartesian tensors. Now by applying the conservation law

$$T^{\alpha\beta}{}_{,\beta} = 0, \tag{2.71}$$

it can be shown

$$\frac{\partial^2}{\partial t^2}\int T^{00}x^i x^j d\vec{x} = 2\int T^{ij} d\vec{x}, \tag{2.72}$$

where $i, j = 1, 2, 3$ run over spatial components. For a source with velocities $v \ll 1$, the component, T^{00}, is approximately the mass density, ρ, and the left side of Equation 2.72 is

$$\frac{\partial^2}{\partial t^2} \int T^{00} x^i x^j d\vec{x} \approx \frac{\partial^2}{\partial t^2} \int \rho x^i x^j d\vec{x} = \ddot{Q}^{ij}, \tag{2.73}$$

where $\mathbf{Q}$ is the mass-quadrupole moment[1] (often denoted $\mathbf{I}$), and over-dots denote time derivatives. We can now write down the spatial part of the GW as

$$\bar{h}^{ij} = \frac{2}{R} \ddot{Q}^{ij}(t - R). \tag{2.74}$$

This is the famous quadrupole formula for the gravitational radiation from distant slow-moving sources, and finds many applications in astrophysics. This is the equation that will be used in Chapter 3 to derive the GW signal from a binary system.

2.6 Physical Effects

As stated in Chapter 1, the physical effect of a GW is to change the proper distance between points, and to alternately stretch and compress a ring of test particles. To demonstrate this effect mathematically, consider two freely falling test particles whose geodesics are connected by a vector, ζ^α, and define an inertial coordinate system in the rest frame of the particle where ζ^α originates, as in Figure 2.1.

Since ζ^α is a connecting vector between two geodesics, and we parametrize both curves by a common parameter, τ, we can appeal to the equation of geodesic deviation:

$$\nabla_U \nabla_U \zeta^\alpha = R^\alpha{}_{\mu\nu\beta} U^\mu U^\nu \zeta^\beta, \tag{2.75}$$

where U^α is the tangent curve to the geodesic from which ζ^α originates, and ∇_U is the

---

[1] There are various conventions for defining and denoting the quadrupole moment tensor. In particular, the quantity $\mathbf{Q}$ is often defined to be trace-free; however, the trace-free quadrupole moment tensor is also commonly referred to as the reduced quadrupole moment tensor, further confusing the matter. As defined above, $\mathbf{Q}$ is not trace free in general, but is the natural form that emerges from the GW derivation. This definition could be unambiguously described as the "second moment of the mass distribution," however this differs from the common language. The notation $\mathbf{Q}$ is chosen as a base quantity, which appears in the initial GW quadrupole formula, and is explicitly denoted as trace free with a superscript T when transformed in subsequent sections.

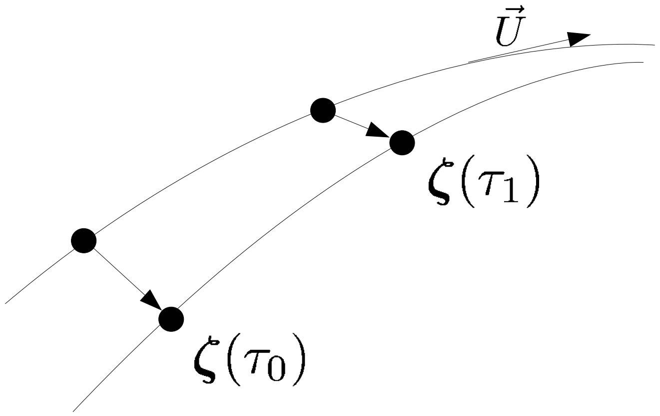

Figure 2.1: Two freely falling test particles with geodesics parametrized by τ and connecting vector $\boldsymbol{\zeta}$. Coordinates are chosen to move along the geodesic with tangent vector, $\boldsymbol{U}$, and from which $\boldsymbol{\zeta}$ originates.

covariant derivative along the curve with tangent vector, $\boldsymbol{U}$. This equation describes the evolution of the connecting vector, $\boldsymbol{\zeta}$, and represents the effect of spacetime curvature on a pair of nearby particles. Note that in flat space, where $R^{\alpha}{}_{\mu\nu\beta} = 0$, there is no deviation so geodesics that begin parallel will remain parallel, which is generally not true for curved spacetimes.

The choice of coordinates that move along the geodesic with tangent vector, $\boldsymbol{U}$, provide several simplifications. First, in this frame we have $U^{\alpha} = \dfrac{dx^{\alpha}}{d\tau} = \delta^{\alpha}{}_{0}$, and hence, we can consider the proper time parameter, τ, and the coordinate time, t, interchangeably. In this freely falling frame, all the Christoffel symbols vanish at the spatial origin, i.e., the location of the test particle, and so the covariant derivatives, ∇_U, reduce to ordinary derivatives, $\dfrac{d}{d\tau}$. Lastly, since we are always in the rest frame of the first test particle, the components, $\zeta^{\alpha}(\tau)$, can be regarded as the proper distances between the two test particles at parameter value, τ. These simplifications lead to

$$\frac{d^2\zeta^{\alpha}}{d\tau^2} = \frac{\partial^2\zeta^{\alpha}}{\partial t^2} = R^{\alpha}{}_{\mu\nu\beta}U^{\mu}U^{\nu}\zeta^{\beta} = R^{\alpha}{}_{00\beta}\zeta^{\beta}. \tag{2.76}$$

Define the initial connecting vector as $\boldsymbol{\zeta}(\tau_0) = (0, \varepsilon, 0, 0)$, which further simplifies the equation to

$$\frac{\partial^2 \zeta^\alpha}{\partial t^2} = \varepsilon R^\alpha{}_{00x} = -\varepsilon R^\alpha{}_{0x0}. \tag{2.77}$$

The components of the Riemann tensor are gauge invariant quantities, so we can use the transverse-traceless gauge to determine the equations of motion for $\boldsymbol{\zeta}$:

$$R^x{}_{0x0} = R_{x0x0} = -\frac{1}{2} h^{TT}_{xx,00}, \tag{2.78}$$

$$R^x{}_{0y0} = R_{x0y0} = -\frac{1}{2} h^{TT}_{xy,00}, \text{ and} \tag{2.79}$$

$$R^y{}_{0y0} = R_{y0y0} = \frac{1}{2} h^{TT}_{xx,00}, \tag{2.80}$$

and so, for the two particles beginning with separation vector $\boldsymbol{\zeta}(\tau_0) = (0, \varepsilon, 0, 0)$, the Equations of motion for $\boldsymbol{\zeta}$ are

$$\frac{\partial^2 \zeta^x}{\partial t^2} = \frac{\varepsilon}{2} \frac{\partial^2}{\partial t^2} h^{TT}_{xx}, \text{ and} \tag{2.81}$$

$$\frac{\partial^2 \zeta^y}{\partial t^2} = \frac{\varepsilon}{2} \frac{\partial^2}{\partial t^2} h^{TT}_{xy}, \tag{2.82}$$

and for a pair of particles initially separated in the y direction with $\boldsymbol{\zeta}(\tau_0) = (0, 0, \varepsilon, 0)$:

$$\frac{\partial^2 \zeta^x}{\partial t^2} = \frac{\varepsilon}{2} \frac{\partial^2}{\partial t^2} h^{TT}_{xy}, \text{ and} \tag{2.83}$$

$$\frac{\partial^2 \zeta^y}{\partial t^2} = -\frac{\varepsilon}{2} \frac{\partial^2}{\partial t^2} h^{TT}_{xx}. \tag{2.84}$$

Since the geodesic deviation equation is linear, we can form the general solution for a pair of particles displaced by small distance in an arbitrary direction in the plane orthogonal to the direction of wave propagation, i.e., $\boldsymbol{\zeta}(\tau_0) = (0, \varepsilon_x, \varepsilon_y, 0)$:

$$\frac{\partial^2 \zeta^x}{\partial t^2} = \frac{1}{2} \frac{\partial^2}{\partial t^2} \left(\varepsilon_x h^{TT}_{xx} + \varepsilon_y h^{TT}_{xy} \right), \text{ and} \tag{2.85}$$

$$\frac{\partial^2 \zeta^y}{\partial t^2} = \frac{1}{2} \frac{\partial^2}{\partial t^2} \left(\varepsilon_x h^{TT}_{xy} - \varepsilon_y h^{TT}_{xx} \right). \tag{2.86}$$

We can solve these equations by assuming a plane-wave form for h^{TT}, as in Equation 2.47 and initial rest conditions for the two particles. This leads to

$$\begin{pmatrix} \zeta^x \\ \zeta^y \end{pmatrix} = \begin{pmatrix} \varepsilon_x \\ \varepsilon_y \end{pmatrix} + \frac{1}{2} \begin{pmatrix} A_{xx} & A_{xy} \\ A_{xy} & -A_{xx} \end{pmatrix} \begin{pmatrix} \varepsilon_x \\ \varepsilon_y \end{pmatrix} \exp(i\omega t). \tag{2.87}$$

This equation gives justification to the polarization labels plus and cross. If we have a pure plus wave with $A_{xy} = 0$, then the effect on a ring of test particles is to alternately stretch and compress the ring along the x and y dimensions, creating a plus-shaped pattern of oscillation. For a cross wave with $A_{xx} = 0$, the ring of particles is stretched and compressed along the lines $y = x$ and $y = -x$, forming a cross-shaped pattern (see Figure 1.3). This solution also shows the amplitude of oscillation depends on the initial separation. Of course, this solution only holds to first order in a variety of small quantities, including the components of $\boldsymbol{\zeta}$. If separation becomes large compared to the GW wavelength, then the linear approximation is no longer valid.

It is important to note we have restricted the GW to be small in the sense that $|h^{\alpha\beta}| \ll 1$, and for a plane wave, the amplitude of oscillation created by a passing GW is proportional to $h^{\alpha\beta}$. By inserting explicit factors of G and c, we can find an order of magnitude estimate for the upper limit on the oscillation amplitude in standard units for a source at distance, R, with mass, M, and spatial extent, D, oscillating at frequency, f:

$$\Delta|\boldsymbol{\zeta}| \sim |\mathbf{h}||\boldsymbol{\zeta}_0| \sim \frac{G|\ddot{\mathbf{Q}}|}{c^4 R}|\boldsymbol{\zeta}_0| \lesssim \frac{GMD^2 f^2}{c^4 R}|\boldsymbol{\zeta}_0|. \tag{2.88}$$

For a galactic source with $R \sim 10$ ly, $M \sim M_\odot$, $f \sim 0.1$ mHz, and $D \sim R_\odot$ (a compact binary, for example), the strain $|\mathbf{h}| \sim 10^{-21}$, and a pair of particles separated by a distance $\varepsilon \sim 1$km, the amplitude of oscillation has an upper limit on the order $\Delta|\boldsymbol{\zeta}| \sim 10^{-18}$ m, or several orders of magnitude smaller than the nucleus of an atom. Even for much more energetic sources, strains are expected to have upper limits on the order of $|\mathbf{h}| \sim 10^{-19}$. These terribly small numbers explain why the GW detection effort has been so difficult, and why Einstein himself initially thought GWs could not possibly be physically real.

CHAPTER 3

BINARY SYSTEMS

One of the most common subjects of study in astrophysics is binary star systems. A binary star system (or simply binary for brevity) consists of two stars that are gravitationally bound together. Binaries occupy an important role in astrophysics. It has been estimated that while only $\approx 33\%$ of stars with spectral types G-M have binary companions (Lada 2006), as many as 75% of larger stars (types O-F) are in multiple systems (Raghavan et al. 2010). When the stars that make up a binary are sufficiently far away, they can live out their lives in a more or less typical manner, generally unaffected by the presence of an orbiting companion. It can occur, however, that the component stars are close enough so that gravitational tidal forces have nonnegligible effects on the orbit or stars themselves. I will refer to this second family of binaries as compact binary systems.

Binaries and binary system dynamics are at the core of my research. This chapter will introduce the fundamental physics and nuances of binaries. It will consist of background information that will be heavily utilized in subsequent material, e.g., binary orbital paths, orbit orientation, GW emission, etc.

3.1 One-Body Reduction

The beauty of the two-body central force problem is that it can be reduced to an equivalent one-body problem and the shape of the orbit can be analytically solved for an inverse square force law. The derivations shown here closely parallel those in Goldstein et al. (2002). Begin by considering two masses, m_1 and m_2, at absolute locations given by $\vec{x}_1$ and $\vec{x}_2$ in some arbitrary coordinate system, respectively. We can write the separation vector and center of mass location as

$$\vec{r} = \vec{x}_2 - \vec{x}_1 \qquad \text{and} \qquad \vec{R} = \vec{r}_{\rm cm} = \frac{m_1\vec{x}_1 + m_2\vec{x}_2}{M}, \tag{3.1}$$

where $M = m_1 + m_2$ is the total mass of the system. These quantities are illustrated in Figure 3.1.

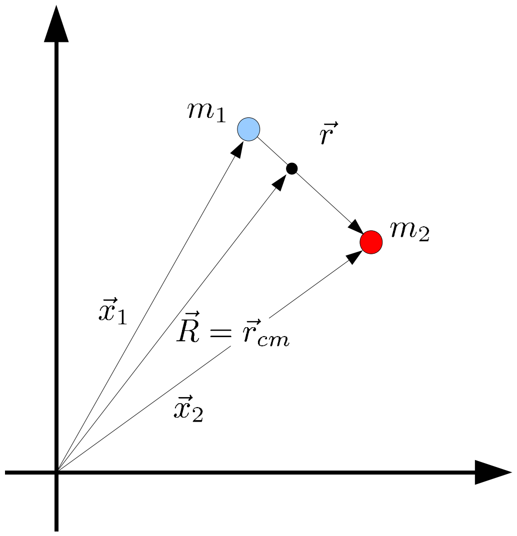

Figure 3.1: Geometry associated with the two-body problem.

Writing these Equations in a matrix form, i.e.,

$$\begin{bmatrix} \vec{r} \\ \vec{R} \end{bmatrix} = \begin{bmatrix} -1 & 1 \\ m_1/M & m_2/M \end{bmatrix} \begin{bmatrix} \vec{x_1} \\ \vec{x_2} \end{bmatrix}, \tag{3.2}$$

we can easily solve for $\vec{x}_1$ and $\vec{x}_2$ in terms of $\vec{r}$ and $\vec{R}$ by inverting the matrix

$$\begin{bmatrix} \vec{x_1} \\ \vec{x_2} \end{bmatrix} = \begin{bmatrix} -m_2/M & 1 \\ m_1/M & 1 \end{bmatrix} \begin{bmatrix} \vec{r} \\ \vec{R} \end{bmatrix}. \tag{3.3}$$

This equation results in the following relationships:

$$\vec{x}_1 = \vec{R} - \frac{m_2}{M}\vec{r}, \text{ and} \tag{3.4}$$

$$\vec{x}_2 = \vec{R} + \frac{m_1}{M}\vec{r}. \tag{3.5}$$

Using these location vectors as generalized coordinates, the Lagrangian for this system can now be written as

$$L = \frac{1}{2}m_1\dot{\vec{x}}_1^2 + \frac{1}{2}m_2\dot{\vec{x}}_2^2 - U(\vec{r}) \tag{3.6}$$

$$= \frac{1}{2}\left[m_1\left(\dot{\vec{R}} - \frac{m_2}{M}\dot{\vec{r}}\right)^2 + m_2(\dot{\vec{R}} + \frac{m_1}{M}\dot{\vec{r}})^2\right] - U(\vec{r}) \tag{3.7}$$

$$= \frac{1}{2}\left[M\dot{\vec{R}}^2 + 2\dot{\vec{R}}\cdot\dot{\vec{r}}\left(\frac{m_1m_2}{M} - \frac{m_2m_1}{M}\right) + \dot{\vec{r}}^2\left(\frac{m_1m_2^2}{M^2} + \frac{m_2m_1^2}{M^2}\right)\right] - U(\vec{r}) \tag{3.8}$$

$$= \frac{1}{2}\left[M\dot{\vec{R}}^2 + \frac{m_1m_2}{M}\dot{\vec{r}}^2\right] - U(\vec{r}), \tag{3.9}$$

where $U(\vec{r}) = V(r) = -G\frac{m_1m_2}{r}$ is the standard Newtonian gravitational potential energy. By appealing to the Lagrange Equations, we can find the equations of motion for $\vec{R}$ to be

$$\frac{d}{dt}\frac{\partial L}{\partial\dot{\vec{R}}} = \frac{\partial L}{\partial\vec{R}} \Rightarrow \ddot{\vec{R}} = 0. \tag{3.10}$$

This shows the system as a whole will move at a constant velocity, $\dot{\vec{R}}$, or stand still. Either way, we are now free to investigate the dynamics of the two-body problem in terms of the single quantity, $\vec{r}$, as the vector, $\vec{R}$, does not dynamically affect the separation vector. The problem has now been recast as the motion of a particle with mass $\mu \equiv m_1m_2/M$ (called the reduced mass) at location, $\vec{r}$, in a potential $V(r) = -Gm_1m_2/r = -GM\mu/r$. Heuristically, this is the orbit problem for a particle of mass μ orbiting around a fixed mass, M.

3.1.1 Solving for the Orbit of the One-Body Problem

Now that the physical system has been reformulated as the motion of a single mass, we can solve for the orbital path. Since the potential term, $V(r)$, is spherically symmetric (only depends on the radial distance, r), the angular momentum, $\vec{\ell} = \vec{r}\times\vec{p}$, of the system must be conserved (a central force field applies no torque). This fixes the value of $\vec{\ell}$ for all time, restricting both $\vec{r}$ and $\vec{p}$ to lie in the plane with normal vector parallel to $\vec{\ell}$. We now describe the vector, $\vec{r}$, in terms of polar coordinates (r, θ) in this plane. The Langrangian for the system in these coordinates can be written

$$\begin{aligned} L &= \frac{1}{2}\mu\dot{\vec{r}}^2 - V(r) && (3.11)\\ &= \frac{1}{2}\mu(\dot{r}^2 + r^2\dot{\theta}^2) - V(r). && (3.12) \end{aligned}$$

The straightforward expansion of $\dot{\vec{r}}^2$ follows from writing $\dot{\vec{r}} = \dot{x}\hat{x} + \dot{y}\hat{y}$, so $\dot{\vec{r}}^2 = \dot{\vec{r}}\cdot\dot{\vec{r}} = \dot{x}^2 + \dot{y}^2$, then writing x and y in polar form and expanding.

We now find the Equations of Motion (EOM) for the coordinates r and θ. The EOM for θ comes from the angular momentum, $p_\theta = \partial L/\partial\dot{\theta}$, and is given by

$$\begin{aligned} & \frac{d}{dt}\frac{\partial L}{\partial \dot{\theta}} = \dot{p}_\theta = \frac{\partial L}{\partial \theta} = 0 && (3.13)\\ \Rightarrow \quad & \frac{d}{dt}(\mu r^2\dot{\theta}) = 0 && (3.14)\\ \Rightarrow \quad & \mu r^2\dot{\theta} = \ell = \text{constant}. && (3.15) \end{aligned}$$

Here ℓ is the magnitude of the angular momentum vector, $\vec{\ell}$, which is now confirmed to be a conserved quantity. Moving to the equation for r, we see

$$\begin{aligned} & \frac{d}{dt}\frac{\partial L}{\partial \dot{r}} = \frac{\partial L}{\partial r} && (3.16)\\ \Rightarrow \quad & \mu\ddot{r} = \mu r\dot{\theta}^2 - \frac{\partial V}{\partial r} && (3.17)\\ \Rightarrow \quad & \mu\ddot{r} - \frac{\ell^2}{\mu r^3} + \frac{\partial V}{\partial r} = 0. && (3.18) \end{aligned}$$

Apply the standard first integral technique of multiplying through by $\dot{r}$ and identifying total derivatives:

$$\begin{aligned} & \mu\dot{r}\ddot{r} - \dot{r}\frac{\ell^2}{\mu r^3} + \dot{r}\frac{\partial V}{\partial r} = 0 && (3.19)\\ \Rightarrow \quad & \frac{d}{dt}\left(\frac{1}{2}\mu\dot{r}^2\right) + \frac{dr}{dt}\frac{d}{dr}\left(\frac{\ell^2}{2\mu r^2}\right) + \frac{dr}{dt}\frac{\partial V}{\partial r} = 0 && (3.20)\\ \Rightarrow \quad & \frac{d}{dt}\left(\frac{1}{2}\mu\dot{r}^2\right) + \frac{d}{dt}\left(\frac{\ell^2}{2\mu r^2}\right) + \frac{dV(r)}{dt} = 0 && (3.21) \end{aligned}$$

$$\Rightarrow \quad \frac{d}{dt}\left(\frac{1}{2}\mu\dot{r}^2 + \frac{\ell^2}{2\mu r^2} + V(r)\right) = 0 \tag{3.22}$$

$$\Rightarrow \quad \frac{d}{dt}\left(\frac{1}{2}\mu\dot{r}^2 + \frac{1}{2}\mu r^2\dot{\theta}^2 + V(r)\right) = 0 \tag{3.23}$$

$$\Rightarrow \quad \frac{d}{dt}\left(\frac{1}{2}\mu(\dot{r}^2 + r^2\dot{\theta}^2) + V(r)\right) = 0 \tag{3.24}$$

$$\Rightarrow \quad \frac{d}{dt}\left(\frac{1}{2}\mu\dot{\vec{r}}^2 + V(r)\right) = 0 \tag{3.25}$$

$$\Rightarrow \quad \frac{1}{2}\mu\dot{\vec{r}}^2 + V(r) = E = \text{constant.} \tag{3.26}$$

We recognize this term as the total energy, which is now explicitly shown to be conserved.

We can use the two conserved quantities, ℓ and E, to find an integrable ODE that will result in the shape of the orbit:

$$\frac{1}{2}\mu\dot{r}^2 + \frac{\ell^2}{2\mu r^2} + V(r) = E \tag{3.27}$$

$$\Rightarrow \quad \dot{r} = \sqrt{\frac{2}{\mu}\left(E - V - \frac{\ell^2}{2\mu r^2}\right)} \tag{3.28}$$

$$\Rightarrow \quad dt = \frac{dr}{\sqrt{\frac{2}{\mu}\left(E - V - \frac{\ell^2}{2\mu r^2}\right)}}. \tag{3.29}$$

As we are interested in the shape of the orbit, $r(\theta)$, at this point we can exchange derivatives with respect to t for derivatives with respect to θ in the following manner:

$$\ell = \mu r^2 \frac{d\theta}{dt}, \tag{3.30}$$

$$\Rightarrow \quad \ell dt = \mu r^2 d\theta, \tag{3.31}$$

where we impose the restriction that $\ell > 0$. Making this substitution in Equation 3.29 yields

$$d\theta = \frac{\ell dr}{\mu r^2\sqrt{\frac{2}{\mu}\left(E - V - \frac{\ell^2}{2\mu r^2}\right)}}. \tag{3.32}$$

Substituting $u = 1/r$ with $du = -(1/r^2)dr$ gives

$$d\theta = -\frac{\dfrac{\ell}{u^2}du}{\mu\dfrac{1}{u^2}\sqrt{\dfrac{2}{\mu}\left(E - V\left(\dfrac{1}{u}\right) - \dfrac{\ell^2u^2}{2\mu}\right)}} = -\frac{du}{\sqrt{\dfrac{2\mu E}{l^2} - \dfrac{2\mu V}{\ell^2} - u^2}}. \tag{3.33}$$

Finally, inserting the potential for an inverse-square force law, i.e., $V(r) = -(k/r) \Rightarrow V(1/u) = -ku$ where $k = GM\mu$, we have

$$d\theta = -\frac{du}{\sqrt{\dfrac{2\mu E}{l^2} + \dfrac{2\mu k u}{l^2} - u^2}}. \tag{3.34}$$

We are now able to integrate this differential equation. Note that Equation 3.34 has the general form

$$\theta = \theta' - \int \frac{du}{\sqrt{au^2 + bu + c}}, \tag{3.35}$$

which has solution

$$\theta = \theta' - \frac{1}{\sqrt{-a}} \arccos\left(-\frac{2au + b}{\alpha}\right), \tag{3.36}$$

where $\alpha^2 = b^2 - 4ac$. By identifying $a = -1$, $b = (2\mu k)/\ell^2$, and $c = (2\mu E)/\ell^2$, we can form our solution as

$$\theta - \theta' = -\arccos\left(\frac{2u - \dfrac{2\mu k}{\ell^2}}{\sqrt{\dfrac{4\mu^2k^2}{\ell^4} + 4\dfrac{2\mu E}{\ell^2}}}\right) \tag{3.37}$$

$$= -\arccos\left(\frac{\dfrac{\ell^2 u}{\mu k} - 1}{\sqrt{1 + \dfrac{2\ell^2 E}{\mu k^2}}}\right) \tag{3.38}$$

$$\Rightarrow \quad u = \frac{\mu k}{\ell^2}\left(1 + \sqrt{1 + \frac{2\ell^2 E}{\mu k^2}}\cos(\theta - \theta')\right) \tag{3.39}$$

$$\Rightarrow \quad r = \frac{C}{1 + e\cos(\theta - \theta')}, \tag{3.40}$$

where $C = \ell^2/(\mu k)$, $e = \sqrt{1 + (2\ell^2 E)/(\mu k^2)}$, and θ' is the value of θ at periapse. Equation 3.40 is the general form of a conic section in polar coordinates with one focus at the origin and eccentricity, e. The eccentricity determines the shape of the orbit according to Table 2, which in turn puts corresponding constraints on the shape due to the total energy, E.

Table 2
Conic Sections

Eccentricity	Shape	Energy
$e = 0$	circle	$E = -\dfrac{\mu k^2}{2l^2}$
$0 < e < 1$	ellipse	$E < 0$
$e = 1$	parabola	$E = 0$
$e > 1$	hyperbola	$E > 0$

We can gain additional insight into the nature of these orbits by rewriting Equation 3.22 as

$$\frac{1}{2}\mu\dot{r}^2 + \frac{\ell^2}{2\mu r^2} + V(r) = \frac{1}{2}\mu\dot{r}^2 + V_{eff}(r) = E, \tag{3.41}$$

where we have defined an effective potential $V_{eff}(r) = V(r) + \ell^2/(2\mu r^2)$. This can be interpreted as the total energy of the radial motion of a particle in an effective potential $V_{eff}(r)$. The orbits with negative energy are bound together so their separation will alternately grow and shrink for elliptical orbits or remain stationary for circular orbits. Bound orbits are those that are caught in the potential well formed by the effective potential, whose minimum corresponds to circular orbits. The bound orbits reach apoapse and periapse at the points where the total energy equals the effective potential energy (zero radial motion), known as the turning points. Unbound orbits are those with positive total energy, which only have one turning point. These orbits come in from infinity for a single interaction at the turning point, and then move away back to infinite distance. This is all illustrated in terms of the total energy in Figure 3.2.

Since we are particularly interested in bound systems, i.e., systems with $E < 0$, we will restrict further attention to the elliptical orbits. Consider the motion of a mass along an elliptical trajectory described by Equation 3.40, as in Figure 3.3.

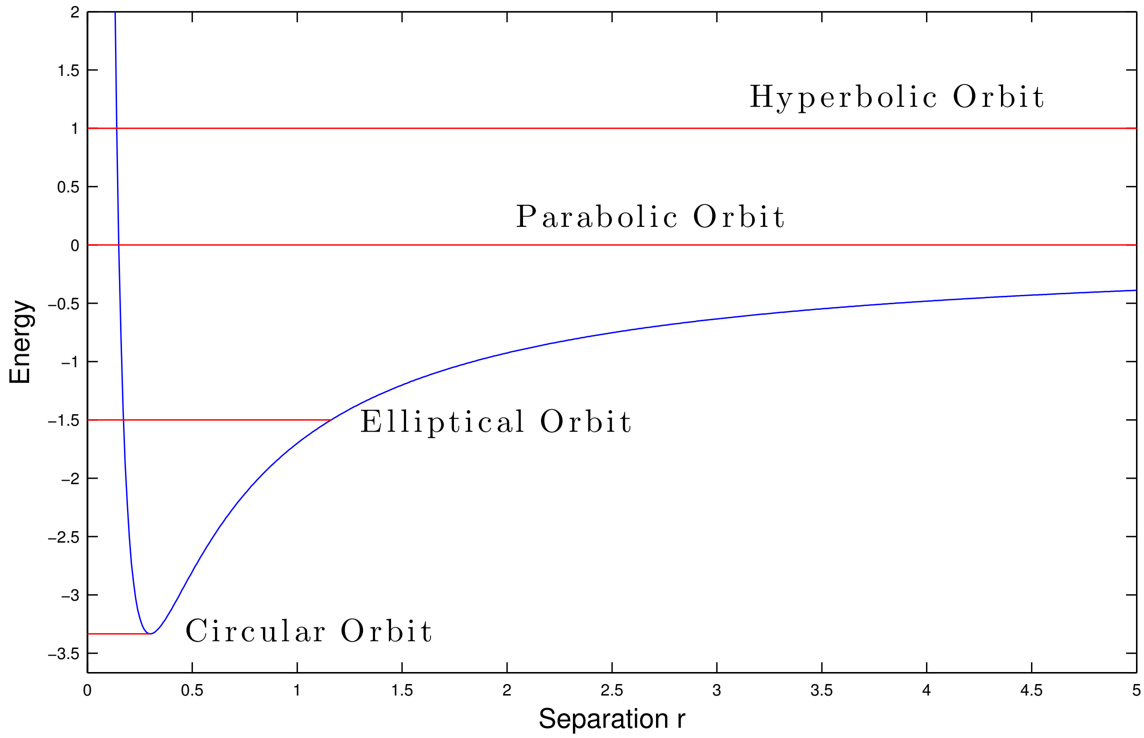

Figure 3.2: The effective potential, $V_{eff}(r)$ (blue), of a particle in the two-body problem experiencing radial motion. The red lines show the various types of orbits corresponding to their total energy, E. Bound orbits are those with $E < 0$, which have two intersections with $V_{eff}(r)$ for elliptical orbits and a single intersection for the circular orbit, which is the global minimum of $V_{eff}(r)$. The unbound orbits are those with $E \geq 0$, and have only one turning point.

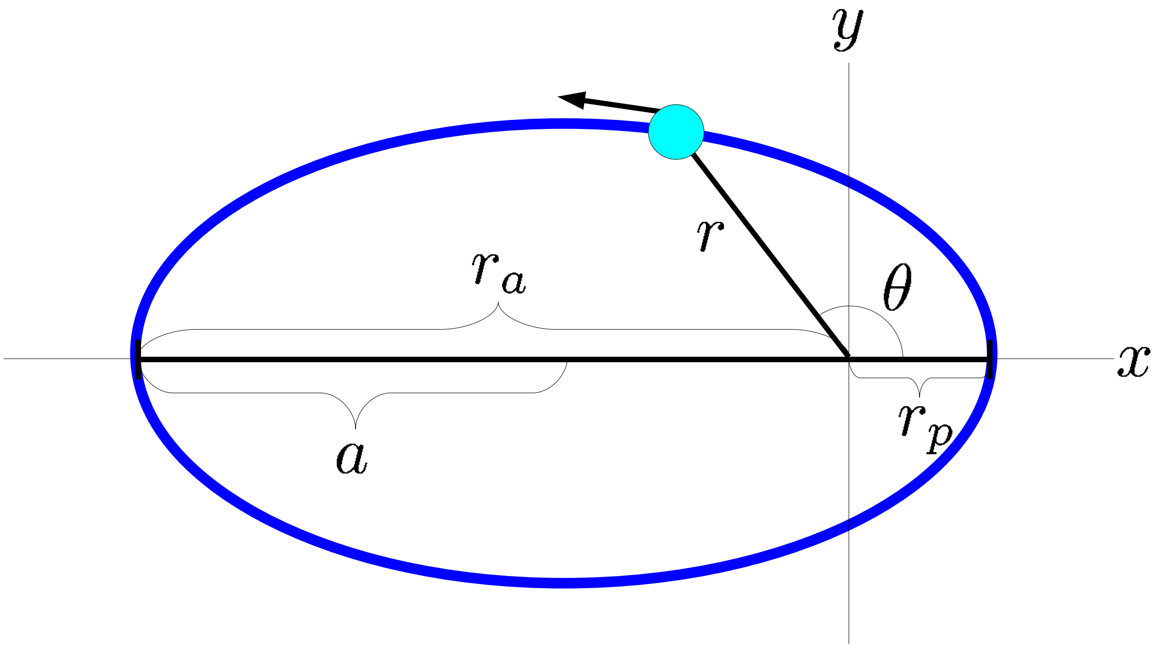

Figure 3.3: The elliptical orbit of the reduced mass, μ, about the center of mass including the periapse and apoapse distances, r_p and r_a, as well as the radial distance, r, and angular position, θ.

The major axis of the ellipse is the longest chord that can be drawn within the ellipse, and analogous to the diameter of a circle. The semimajor axis, typically denoted a, is half the value of the major axis, and is akin to the radius of a circle. We can identify a relationship between a, r_p, and r_a, namely $r_p + r_a = 2a$. Additionally, note the turning points in the orbit (which occur when $\dot{r} = 0$) are located at the apoapse and periapse distances. By referring back to Equation 3.26 and setting $\dot{r} = 0$, we can write

$$\frac{\ell^2}{2\mu r^2} - \frac{k}{r} = E \tag{3.42}$$

$$\Rightarrow \quad r^2 + \frac{k}{E} r - \frac{\ell^2}{2\mu E} = 0. \tag{3.43}$$

The two roots of this quadratic equation, which we can identify at r_p and r_a from the preceding discussion, are

$$r_p = -\frac{k}{2E}(1-e) \qquad \text{and} \qquad r_a = -\frac{k}{2E}(1+e), \tag{3.44}$$

which leaves us with the relationship

$$a = \frac{r_p + r_a}{2} = -\frac{k}{2E}. \tag{3.45}$$

Now note in the definition of eccentricity e, we can write

$$e = \sqrt{1 + \frac{2\ell^2 E}{\mu k^2}} = \sqrt{1 - \frac{\ell^2}{\mu k a}} \Rightarrow \frac{\ell^2}{\mu k} = a(1 - e^2). \tag{3.46}$$

Using this relation, and making the conventional choice that $\theta' = 0$ (define θ so that $\theta = 0$ at periapse), we can finalize the form of the orbital path to be

$$r(\theta) = \frac{a(1 - e^2)}{1 + e\cos(\theta)}. \tag{3.47}$$

What has been derived here? This equation represents the orbital path of the reduced mass μ around the center of mass, which can be completely specified by either pair of values $\{a, e\}$ or $\{\ell, E\}$. This is only one orbital path, however, and there are two stars in the binary system. The relations between this orbit and the trajectory of the actual component masses will be developed in the next section.

3.1.2 Relations Between the One-Body and Two-Body Orbits

Given the relations in Equations 3.4 and 3.5, and by working in the barycenter frame (set $\vec{R} = 0$), the orbital path of the two component masses can be written as

$$r_1(\theta) = \frac{a_1(1 - e^2)}{1 + e\cos(\theta)} \qquad \text{and} \qquad r_2(\theta) = -\frac{a_2(1 - e^2)}{1 + e\cos(\theta)}, \tag{3.48}$$

where $a_1 = a(m_2/M)$ and $a_2 = a(m_1/M)$. Or, by exchanging the negative sign in r_2 for a 180° phase shift in θ, we can rewrite as

$$r_2(\theta) = \frac{a_2(1 - e^2)}{1 - e\cos(\theta)}. \tag{3.49}$$

We can now draw an important conclusion. Since the individual component masses each follow an elliptical path with focus at the origin, and the origin in the barycenter frame is the center of mass, we can conclude that both stars orbit their common center of mass. In addition to the positional relationship, we also have the following momenta relations:

$$\vec{p} = \mu\dot{\vec{r}} = \mu\frac{M}{m_2}\dot{\vec{r}}_1 = m_1\dot{\vec{r}}_1 = \vec{p}_1, \tag{3.50}$$

and similarly $\vec{p}_2 = -\vec{p}$. This both verifies conservation of momentum in the barycenter frame ($\vec{p}_1 + \vec{p}_2 = 0$), as well as gives the additional connection between the reduced mass orbit and the two-body orbit.

3.2 The Laplace-Runge-Lenz Vector

There is another conserved quantity that can be constructed, and will be useful in later sections. For a general central force problem, we have

$$\dot{\vec{p}} = f(r)\frac{\vec{r}}{r}, \tag{3.51}$$

where $f(r)$ is a conservative central force, i.e., a force whose magnitude depends only on the radial distance from the the origin of coordinates, and always points in a radial direction. Consider the cross product

$$\begin{aligned}\dot{\vec{p}} \times \vec{\ell} &= \dot{\vec{p}} \times (\vec{r} \times \vec{p}) \qquad (3.52)\\ &= \frac{mf(r)}{r}[\vec{r} \times (\vec{r} \times \dot{\vec{r}})] \qquad (3.53)\\ &= \frac{mf(r)}{r}[\vec{r}(\vec{r} \cdot \dot{\vec{r}}) - \dot{\vec{r}}(\vec{r} \cdot \vec{r})], \qquad (3.54)\end{aligned}$$

and note

$$\vec{r} \cdot \dot{\vec{r}} = \frac{1}{2}\frac{d}{dt}(\vec{r} \cdot \vec{r}) = r\dot{r}, \tag{3.55}$$

where $\dot{r}$ is the velocity in the radial direction. Because $\vec{\ell}$ is conserved, we have

$$\dot{\vec{p}} \times \vec{\ell} = \frac{d}{dt}(\vec{p} \times \vec{\ell}) \tag{3.56}$$

$$= -\mu f(r) r^2 \left(\frac{\dot{\vec{r}}}{r} - \frac{\vec{r}\dot{r}}{r^2} \right) \tag{3.57}$$

$$= -\mu f(r) r^2 \frac{d}{dt} \left(\frac{\vec{r}}{r} \right). \tag{3.58}$$

If we now specify the central force to be the Kepler force, i.e., $f(r) = -k/r^2$, we have

$$\frac{d}{dt}(\vec{p} \times \vec{\ell}) = \frac{\mu k}{r^2} r^2 \frac{d}{dt} \left(\frac{\vec{r}}{r} \right) \tag{3.59}$$

$$= \frac{d}{dt} \left(\frac{\mu k \vec{r}}{r} \right), \tag{3.60}$$

which directly implies

$$\frac{d}{dt} \left(\vec{p} \times \vec{\ell} - \frac{\mu k \vec{r}}{r} \right) = 0. \tag{3.61}$$

This is another conserved vector, known as the Laplace-Runge-Lenz vector, and is denoted

$$\vec{A} = \vec{p} \times \vec{\ell} - \frac{\mu k \vec{r}}{r}. \tag{3.62}$$

At pericenter, both $\vec{p}$ and $\vec{\ell}$ are orthogonal to $\vec{r}$, which implies $\vec{p} \times \vec{\ell}$ must point toward the same direction as $\vec{r}$, i.e., toward pericenter. Since $\vec{A}$ is conserved, it then always points toward pericenter. The magnitude of $\vec{A}$ is found by taking the dot product of $\vec{A}$ with $\vec{r}$:

$$\vec{A} \cdot \vec{r} = Ar\cos(\theta) = \vec{r} \cdot (\vec{p} \times \vec{\ell}) - \mu k r \tag{3.63}$$

$$= \vec{\ell} \cdot (\vec{r} \times \vec{p}) - \mu k r \tag{3.64}$$

$$= \ell^2 - \mu k r \tag{3.65}$$

$$= \mu k a(1 - e^2) - \mu k r \tag{3.66}$$

$$= \mu k \left(r[1 + e\cos(\theta)] - r \right) \tag{3.67}$$

$$= \mu k r[e\cos(\theta)], \tag{3.68}$$

and so we have

$$A = \mu k e. \tag{3.69}$$

Scaling $\vec{A}$ by $1/(\mu k)$ leaves a conserved vector with magnitude equal to the eccentricity of the binary, known as the eccentricity vector, $\vec{e}$. This will be of use in Chapter 4.

3.3 Orbital Parameters

The orbital path followed by the individual stars, or component masses, is specified by Equation 3.47. This is the equation of an ellipse with one focus (the center of mass) at the origin, eccentricity, e, and semimajor axis, a. If desired, Equation 3.47 can be modified by substituting $r_p = a(1 - e)$ to read

$$r(\theta) = \frac{r_p(1 + e)}{1 + e\cos(\theta)}, \tag{3.70}$$

which is now more generally applicable to conic sections of any eccentricity. Values without a numerical subscript, e.g. a and r_p, will be used to denote quantities relating to the reduced mass orbit, while numeric subscripts will be added when referring to the parameters for the individual masses, e.g., a_1 or $r_{p,2}$. These parameters define the intrinsic (inherent to the system itself) geometrical parameters of the orbit, i.e., the shape of the orbit within the orbital plane. See Figure 3.4.

The extrinsic (observer dependent) geometrical parameters must specify the orientation of the orbit in three-dimensional space. For orientation we adopt the standard Euler angles, but label them in accordance with astronomical convention: inclination, ι, argument of periapse, ω_0, and the longitude of the ascending node, Ω_0. These angles, as well as the true anomaly, θ (angular position of the mass in its orbit), and are depicted in Figure 3.5.

3.4 Observation Geometry

To begin relating binary quantities to observations from Earth, we must first define appropriate coordinate systems in which to work. This will be particularly important when attempting to express GWs in an observer coordinate system.

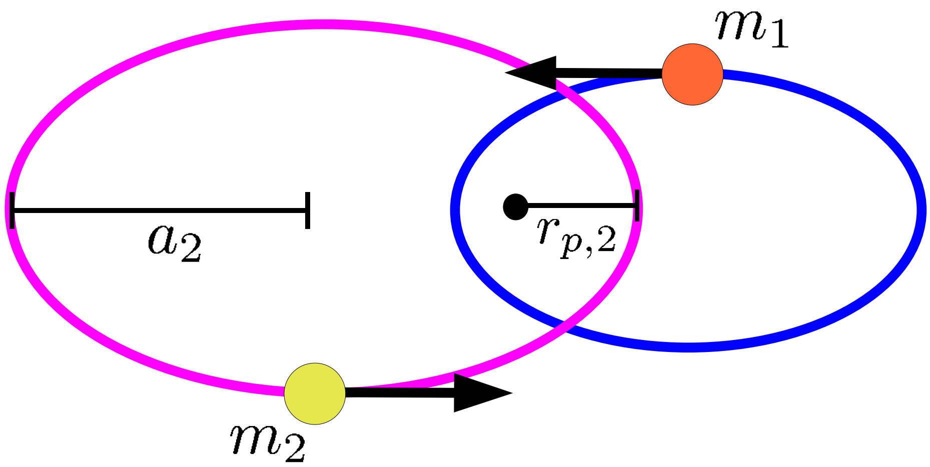

Figure 3.4: Several standard orbital parameters, including the component masses m_1 and m_2, the semimajor axis of the second, smaller mass, a_2, and the corresponding periapse distance, $r_{p,2}$.

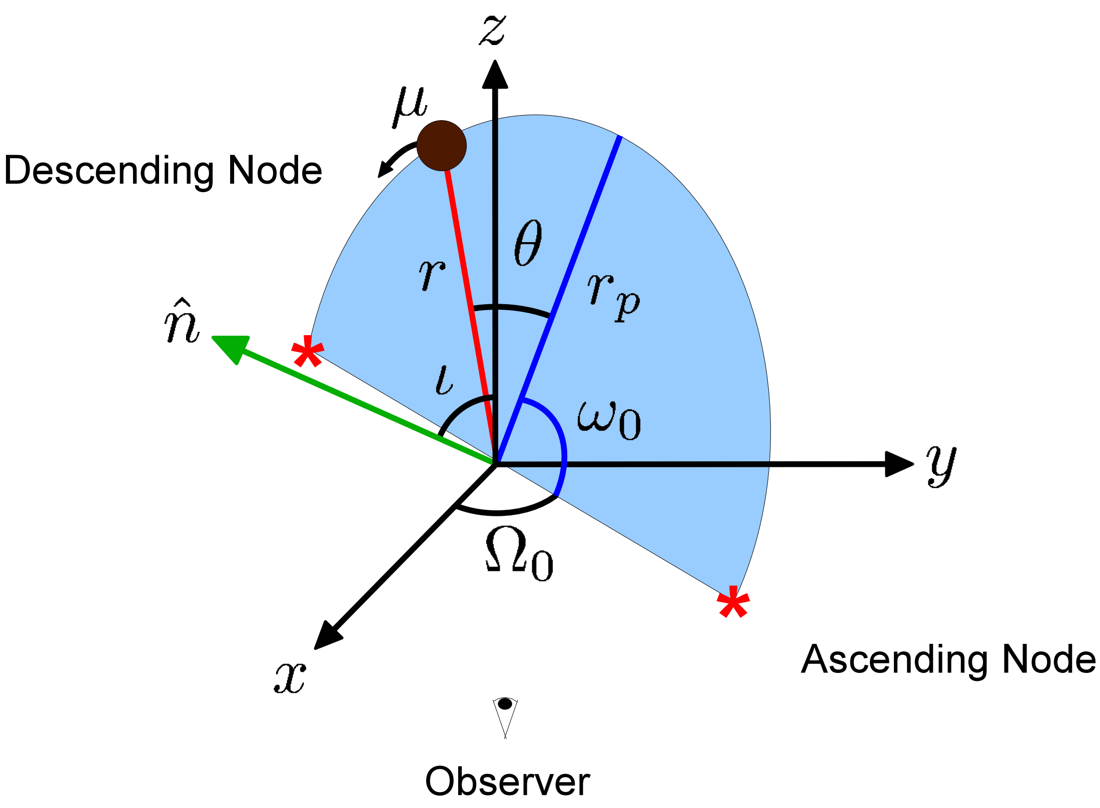

Figure 3.5: The orbital angles of a binary system including true anomaly, θ, inclination, ι, longitude of the ascending node, Ω_0, and argument of periapse, ω_0.

Define a fundamental coordinate system called the celestial frame, described by the three orthonormal unit vectors $\hat{\imath}$, $\hat{\jmath}$, and $\hat{k}$. Let $\hat{k}$ point toward the north celestial pole, along the axis of Earth's rotation, and $\hat{\imath}$ point to the so-called first point in Aries, which is one of two points where the ecliptic plane intersects the celestial equator.

On this coordinate frame we define angular coordinates α and δ, the right ascension and declination, respectively. In comparison with standard spherical-polar coordinates, α maps one-to-one to the azimuthal angle and δ is the complement of the polar angle, i.e., $\delta = \theta_{\text{pol}} - \pi/2$. We can write the unit vectors for these angular coordinates as

$$\hat{\alpha} = -\sin(\alpha)\hat{\imath} + \cos(\alpha)\hat{\jmath}, \text{ and} \tag{3.71}$$

$$\hat{\delta} = -\sin(\delta)[\cos(\alpha)\hat{\imath} + \sin(\alpha)\hat{\jmath}] + \cos(\delta)\hat{k}. \tag{3.72}$$

If a source of interest is located by a vector, $\vec{R}$, define the sky plane as the plane located a distance, R, from the origin with normal vector, $\vec{R}$, as shown in Figure 3.6. This plane is tangent to the celestial sphere at radius, R, and can be described as the α-δ plane in the $\{\hat{\alpha}, \hat{\delta}, \hat{R}\}$ coordinate system.

Next, suppose we observe a binary system and wish to relate the binary orientation

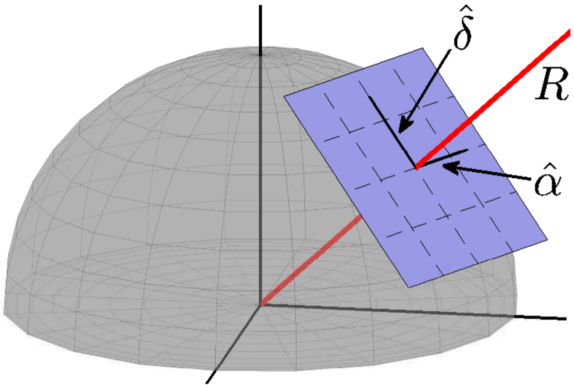

Figure 3.6: Illustration of the sky plane (purple): the coordinate plane on the sky, tangent to the Celestial Sphere (grey), as observed from a location on Earth. Here R is the radial vector pointing along the line of sight to a source, $\hat{\alpha}$ is a unit vector pointing in the direction of increasing right ascension, and $\hat{\delta}$ is a unit vector pointing in the direction of increasing declination.

to the sky plane. Define a vector, $\hat{u}$, which points along the line of nodes, defined by the longitude of the ascending node angle, Ω_0, measured CCW from the $\hat{\alpha}$ axis. Additionally, define a unit normal vector, $\hat{n}$, parallel to the binary angular momentum vector, $\vec{\ell}$, and a third vector, $\hat{v}$, which completes a right-handed coordinate system $\{\hat{u}, \hat{v}, \hat{n}\}$ (see Figure 3.7). Note when the argument of periapse $\omega_0 = 0$, the vector u points along the binary axis.

Writing these three vectors in the celestial frame in terms of observational angles describing the binary orientation gives

$$\hat{u} = \cos(\Omega_0)\hat{\alpha} + \sin(\Omega_0)\hat{\delta}, \tag{3.73}$$

$$\hat{v} = \cos(\iota)[-\sin(\Omega_0)\hat{\alpha} + \cos(\Omega_0)\hat{\delta}] + \sin(\iota)\hat{R}, \text{ and} \tag{3.74}$$

$$\hat{n} = \sin(\iota)[\sin(\Omega_0)\hat{\alpha} - \cos(\Omega_0)\hat{\delta}] + \cos(\iota)\hat{R}. \tag{3.75}$$

To finally connect this back with the orbital shape equation, define polar coordinates (r, ϑ) in the u-v orbital plane such that a point $a_u\hat{u} + a_v\hat{v}$ can be expressed by

$$a_u = r\cos(\vartheta), \text{ and} \tag{3.76}$$

$$a_v = r\sin(\vartheta). \tag{3.77}$$

In this coordinate system, the orbital shape equation becomes $r(\theta) = r(\vartheta - \omega_0)$, where θ is the angular distance of a binary component from periapse, and ϑ is the angular coordinate in the u-v plane measured from the vector $\hat{u}$, and ω_0 is the argument of periapse. We now have the ability to move from the binary coordinate frame (r, θ) (i.e., the orbital plane with coordinates aligned with the binary axis), into the Earth-based observer frame $\{\hat{i}, \hat{j}, \hat{k}\}$ and back again through the series of invertible coordinate transformations $(r, \theta) \leftrightarrow (\hat{u}, \hat{v}, \hat{n}) \leftrightarrow (\hat{\alpha}, \hat{\delta}, \hat{R}) \leftrightarrow (\hat{i}, \hat{j}, \hat{k})$.

3.5 Gravitational Wave Emissions

In this Section, the GW emissions from a binary system are calculated. The calculation is performed in the linearized GW theory, and factors of G and c are left explicit. The

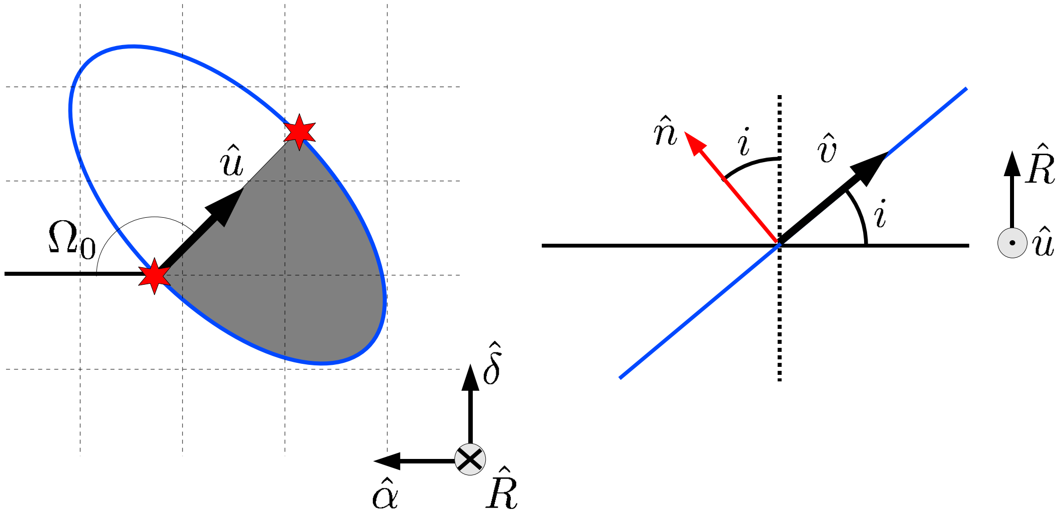

(a) Observer view.

(b) Edge on view.

Figure 3.7: Observing a binary system in the sky-plane coordinates. The unit vector $\hat{u}$ points along the line of nodes, $\hat{n}$ is parallel to the angular momentum vector of the binary, and $\hat{v}$ completes an orthonormal triad for coordinates in the orbital plane such that $\hat{u} \times \hat{v} = \hat{n}$.

derivation in this Section closely parallels that in Wahlquist (1987), with some notational changes, namely vectors will be written with an over-arrow, e.g., $\vec{x}$, and dyadic notation will be used for tensors, written in bold face $\mathbf{X}$ as opposed to using index notation $X^{\alpha\beta}$ and with outer products denoted by $\vec{x} \otimes \vec{x} = \vec{x}\vec{x}$. Since all tensors involved in this section will be formed by the tensor product (outer product) of two vectors, e.g., $\mathbf{X} = \vec{x}\vec{x}$, tensor manipulation will be essentially identical to matrix manipulation, and therefore I may use the terms tensor and matrix interchangeably here (however, explicit matrix/vector transpose notation will be dropped for less notational clutter).

Begin with the quadrupole formula for GW emission,

$$\mathbf{h}^{TT}(t) = \frac{2G}{Rc^4}\ddot{\mathbf{Q}}^{TT}\left(t - \frac{R}{c}\right), \tag{3.78}$$

where $\vec{R}$ is a vector pointing from the observer to the center of mass, the TT superscript signifies the transverse-traceless gauge. Keeping with the previous definition of the mass quadrupole moment for a system of mass, $\mathfrak{M}$ (see Section 2.5), we start with

$$\mathbf{Q} \equiv \int_{\mathfrak{M}} \vec{x}\vec{x} dm, \tag{3.79}$$

which for a binary system simplifies to

$$\mathbf{Q} = m_1\vec{x}_1\vec{x}_1 + m_2\vec{x}_2\vec{x}_2 = M\vec{R}\vec{R} + \mu\vec{r}\vec{r}. \tag{3.80}$$

Making use of the transformations in Equations 3.4 and 3.5 once again, we can rewrite this as

$$\mathbf{Q} = M\vec{R}\vec{R} + \mu\vec{r}\vec{r}. \tag{3.81}$$

Equation 3.78 has been transformed from Equation 2.74 by transforming each side into the transverse-traceless coordinates. We, therefore, need to transform the quadrupole tensor, $\mathbf{Q}$, to the transverse-traceless coordinate system before it can be used in Equation 3.78. Gravitational waves emitted from a source very far away from us will have propagation direction $-\hat{R}$, so we can form the transverse part of $\mathbf{Q}$ by projecting onto the space orthogonal to $\hat{R}$, i.e., with the projection operator

$$\mathbf{P}_\perp = \mathbf{I} - \mathbf{P}_R = \mathbf{I} - \hat{R}(\hat{R}\cdot\hat{R})^{-1}\hat{R} = \mathbf{I} - \hat{R}\hat{R}, \tag{3.82}$$

where $\mathbf{I}$ is the identity matrix, so the transverse part Q^T is found to be

$$\mathbf{Q}^T = \mathbf{P}_\perp\mathbf{Q}\mathbf{P}_\perp = \mathbf{P}_\perp(M\vec{R}\vec{R} + \mu\vec{r}\vec{r})\mathbf{P}_\perp = \mu\vec{r}^T\vec{r}^T. \tag{3.83}$$

Here we have used the projection $\mathbf{P}_\perp\vec{R} = 0$, and defined the transverse part of $\vec{r}$ as $\vec{r}^T = \mathbf{P}_\perp\vec{r}$. We could now create a traceless version by subtracting the trace of $\mathbf{Q}^T$, i.e.,

$$\mathbf{X} = \mathbf{Q}^T - \mathrm{Tr}(\mathbf{Q}^T)\left(\frac{\mathbf{I}}{\mathrm{Tr}(\mathbf{I})}\right); \tag{3.84}$$

however, this would destroy the transverse nature we have established for $\mathbf{Q}^T$. Alternatively, note that we can detrace a matrix $\mathbf{X}$ with respect to any other matrix $\mathbf{A}$ by the following:

$$\mathbf{X}_A = \mathbf{XA} - \mathrm{Tr}(\mathbf{XA})\left(\frac{\mathbf{A}}{\mathrm{Tr}(\mathbf{A})}\right). \tag{3.85}$$

In order to maintain the transverse nature of $\mathbf{Q}^T$, we can detrace it with respect to the projection, $\mathbf{P}_\perp$,

$$\mathbf{Q}^{TT} = \mathbf{Q}^T\mathbf{P}_\perp - \mathrm{Tr}(\mathbf{Q}^T\mathbf{P}_\perp)\left(\frac{\mathbf{P}_\perp}{\mathrm{Tr}(\mathbf{P}_\perp)}\right), \tag{3.86}$$

but note since $\mathbf{Q}^T = \mathbf{P}_\perp\mathbf{Q}\mathbf{P}_\perp$ and $\mathbf{P}_\perp\mathbf{P}_\perp = \mathbf{P}_\perp$, we have $\mathbf{Q}^T\mathbf{P}_\perp = \mathbf{Q}^T$. Additionally, note

$$\mathrm{Tr}(\mathbf{P}_\perp) = \mathrm{Tr}(\mathbf{I} - \hat{R}\hat{R}) = \mathrm{Tr}(\mathbf{I}) - \mathrm{Tr}(\hat{R}\hat{R}) = 3 - \mathrm{Tr}(\hat{R}\cdot\hat{R}) = 3 - 1 = 2. \tag{3.87}$$

Using these two facts, we can write $\mathbf{Q}^{TT}$ as

$$\mathbf{Q}^{TT} = \mathbf{Q}^T - \frac{1}{2}\mathrm{Tr}(\mathbf{Q}^T)\mathbf{P}_\perp = \mu\left(\vec{r}^T\vec{r}^T - \frac{1}{2}[\vec{r}^T\cdot\vec{r}^T]\mathbf{P}_\perp\right). \tag{3.88}$$

Now move from the binary coordinate system into the u-v coordinates defined in Section 3.4,

$$\vec{r} = r\cos(\vartheta)\hat{u} + r\sin(\vartheta)\hat{v}, \tag{3.89}$$

from which we can find (with $\vartheta = \theta + \omega_0$)

$$\vec{r}^T = \mathbf{P}_\perp(r\cos(\theta+\omega_0)\hat{u} + r\sin(\theta+\omega_0)\hat{v}) \tag{3.90}$$

$$= (\mathbf{I} - \hat{R}\hat{R})(r\cos(\theta+\omega_0)\hat{u} + r\sin(\theta+\omega_0)\hat{v}) \tag{3.91}$$

$$= r(\cos(\theta+\omega_0)\hat{u} + r\sin(\theta+\omega_0)[\hat{v} - (\hat{v}\cdot\hat{R})\hat{R}]) \tag{3.92}$$

$$= r(\cos(\theta+\omega_0)\hat{u} + r\sin(\theta+\omega_0)[\hat{v} - \sin(\iota)\hat{R}]). \tag{3.93}$$

If we now express $\vec{r}^T$ in terms of $\hat{\alpha}$ and $\hat{\delta}$ using Equations 3.73 and 3.74, we have

$$\vec{r}^T = r[\cos(\Omega_0)\cos(\theta+\omega_0) - \sin(\Omega_0)\cos(\iota)\sin(\theta+\omega_0)]\hat{\alpha} \tag{3.94}$$

$$+ r[\sin(\Omega_0)\cos(\theta+\omega_0) + \cos(\Omega_0)\cos(\iota)\sin(\theta+\omega_0)]\hat{\delta}. \tag{3.95}$$

Write $\vec{r}^T = r_\alpha\hat{\alpha} + r_\delta\hat{\delta}$, then compute $\vec{r}^T\vec{r}^T$,

$$\vec{r}^T\vec{r}^T = (r_\alpha\hat{\alpha} + r_\delta\hat{\delta})(r_\alpha\hat{\alpha} + r_\delta\hat{\delta}) = r_\alpha^2\hat{\alpha}\hat{\alpha} + r_\alpha r_\delta(\hat{\alpha}\hat{\delta} + \hat{\alpha}\hat{\delta}) + r_\delta^2\hat{\delta}\hat{\delta}. \tag{3.96}$$

Writing $\mathbf{I} - \hat{R}\hat{R} = \hat{\alpha}\hat{\alpha} + \hat{\delta}\hat{\delta} + \hat{R}\hat{R} - \hat{R}\hat{R} = \hat{\alpha}\hat{\alpha} + \hat{\delta}\hat{\delta}$, we can now express $\mathbf{Q}^{TT}$ in the sky frame as

$$\mathbf{Q}^{TT} = \mu\left(\vec{r}^T\vec{r}^T - \frac{1}{2}[\vec{r}^T\cdot\vec{r}^T]\mathbf{P}_\perp\right) \tag{3.97}$$

$$= \mu\left(r_\alpha^2\hat{\alpha}\hat{\alpha} + r_\alpha r_\delta(\hat{\alpha}\hat{\delta} + \hat{\delta}\hat{\alpha}) + r_\delta^2\hat{\delta}\hat{\delta} - \frac{1}{2}[r_\alpha^2 + r_\delta^2][\hat{\alpha}\hat{\alpha} + \hat{\delta}\hat{\delta}]\right) \tag{3.98}$$

$$= \mu\left(\frac{1}{2}(r_\alpha^2 - r_\delta^2)(\hat{\alpha}\hat{\alpha} - \hat{\delta}\hat{\delta}) + r_\alpha r_\delta(\hat{\alpha}\hat{\delta} + \hat{\delta}\hat{\alpha})\right) \tag{3.99}$$

$$= Q_+\mathbf{e}_+ + Q_\times\mathbf{e}_\times, \tag{3.100}$$

where the following definitions have been made:

$$Q_+ = \frac{\mu}{2}(r_\alpha^2 - r_\delta^2) \qquad , \qquad Q_\times = \mu r_\alpha r_\delta, \tag{3.101}$$

and

$$\mathbf{e}_+ = \hat{\alpha}\hat{\alpha} - \hat{\delta}\hat{\delta} \qquad , \qquad \mathbf{e}_\times = \hat{\alpha}\hat{\delta} + \hat{\delta}\hat{\alpha}. \tag{3.102}$$

Some simple trigonometric substitutions allow us to write

$$Q_+ = \frac{\mu r^2}{2}\left(\cos(2\Omega_0)[\cos^2(\theta+\omega_0) - \cos^2(\iota)\sin^2(\theta+\omega_0)]\right. \tag{3.103}$$

$$\left. - \sin(2\Omega_0)\cos(\iota)\sin[2(\theta+\omega_0)]\right),$$

and

$$Q_\times = \frac{\mu r^2}{2}\left(\sin(2\Omega_0)[\cos^2(\theta+\omega_0) - \cos^2(\iota)\sin^2(\theta+\omega_0)] \right. \tag{3.104}$$
$$\left. + \cos(2\Omega_0)\cos(\iota)\sin[2(\theta+\omega_0)]\right).$$

We are almost at the point of evaluating the derivatives of $\mathbf{Q}^{TT}$, which we must do with respect to θ since we have no explicit time dependence, i.e.,

$$\ddot{\mathbf{Q}}^{TT} = \dot{\theta}\frac{d}{d\theta}\left(\dot{\theta}\frac{d\mathbf{Q}^{TT}}{d\theta}\right). \tag{3.105}$$

Before that, however, we must find $\dot{\theta}$. We can do so by the making use of several relations from Section 3.1.1 (equations 3.30 and 3.46):

$$\mu r^2\dot{\theta} = \ell \tag{3.106}$$
$$\Rightarrow \quad \dot{\theta}^2 = \frac{\ell^2}{\mu^2 r^4} \tag{3.107}$$
$$\Rightarrow \quad \dot{\theta}^2 = \frac{\mu k a(1-e^2)}{\mu^2 r^4} \tag{3.108}$$
$$\Rightarrow \quad \dot{\theta}^2 = \frac{GMa(1-e^2)}{\left(\dfrac{a(1-e^2)}{1+e\cos(\theta)}\right)^4} \tag{3.109}$$
$$\Rightarrow \quad \dot{\theta} = \left(\frac{GM}{a^3}\right)^{1/2}(1-e^2)^{-3/2}(1+e\cos(\theta))^2. \tag{3.110}$$

Equation 3.105 can now be rewritten as

$$\ddot{\mathbf{Q}}^{TT} = \left(\frac{GM}{a^3}\right)\left(1-e^2\right)^{-3}(1+e\cos(\theta))^2\frac{d}{d\theta}\left((1+e\cos(\theta))^2\frac{d\mathbf{Q}^{TT}}{d\theta}\right). \tag{3.111}$$

Now collect all of the terms not involved with the θ derivatives, including μ in the Q coefficients, the numerator in $r(\theta)$, and a factor of 2 to find

$$\ddot{\mathbf{Q}}^{TT} = \left(\frac{2GM\mu}{a}\right)\left(1-e^2\right)^{-1}\left[(1+e\cos(\theta))^2\frac{d}{d\theta}\left((1+e\cos(\theta))^2\frac{d\tilde{\mathbf{Q}}^{TT}}{d\theta}\right)\right], \tag{3.112}$$

with $\tilde{\mathbf{Q}} = \mathbf{Q}/(2\mu a^2(1-e^2)^2)$. Substituting this into Equation 3.78, we have

$$\mathbf{h}^{TT} = H\left\{[1+e\cos(\theta)]^2\frac{d}{d\theta}\left([1+e\cos(\theta)]^2\frac{d\tilde{\mathbf{Q}}^{TT}}{d\theta}\right)\right\}, \tag{3.113}$$

where

$$H = \frac{4G^2M\mu}{c^4a(1-e^2)R}. \tag{3.114}$$

The calculation of the θ derivatives in Equation 3.113 is long and tedious (and best done with the aid of a computer algebra package), but once complete, the properly arranged final result can be written as

$$h_+(\theta) = H\left(\cos(2\Omega_0)[A_0+eA_1+e^2A_2] - \sin(2\Omega_0)[B_0+eB_1+e^2B_2]\right), \text{ and} \tag{3.115}$$

$$h_\times(\theta) = H\left(\sin(2\Omega_0)[A_0+eA_1+e^2A_2] + \cos(2\Omega_0)[B_0+eB_1+e^2B_2]\right). \tag{3.116}$$

While these expressions have the appearance of a truncated series in e, these are simply the powers of e that emerge in the derivation. This form is convenient so circular orbits ($e = 0$) collapse to simpler expressions. The A_i and B_i coefficients have the forms

$$A_0 = -\frac{1}{2}[1+\cos^2(\iota)]\cos[2(\theta+\omega_0)], \tag{3.117}$$

$$\begin{aligned} A_1 = {} & \frac{1}{4}\sin^2(\iota)\cos(\theta-\theta') - \frac{1}{8}[1+\cos^2(\iota)][5\cos(\theta+2\omega_0+\theta') \\ & +\cos(3\theta+2\omega_0-\theta')], \text{ and} \end{aligned} \tag{3.118}$$

$$A_2 = \frac{1}{4}\sin^2(\iota) - \frac{1}{4}[1+\cos^2(\iota)]\cos(2[\omega_0+\theta']), \tag{3.119}$$

and

$$B_0 = -\cos(\iota)\cos[2(\theta+\omega_0)], \tag{3.120}$$

$$B_1 = -\frac{1}{4}\cos(\iota)[5\sin(\theta+2\omega_0+\theta')+\sin(3\theta+2\omega_0-\theta')], \text{ and} \tag{3.121}$$

$$B_2 = -\frac{1}{2}\cos(\iota)\sin[2(\omega_0+\theta')]. \tag{3.122}$$

This completes the expressions for quadrupole GW radiation from an arbitrarily oriented elliptical binary. This form of the binary GW Equations was originally published by Wahlquist (1987).

In this chapter we have derived, from first principles, the dynamics of two gravitationally interacting massive bodies. Special attention was paid to bound systems, which result in elliptical orbits. An observer coordinate frame was defined and related to an arbitrarily oriented binary system, and the gravitational wave emissions in this frame were computed. We are now equipped to step into my research projects, which will occupy the subsequent chapters.

CHAPTER 4

BUSTING UP BINARIES: PARABOLIC ENCOUNTERS BETWEEN COMPACT BINARIES AND A SUPERMASSIVE BLACK HOLE

Given the stellar density near the galactic center, close encounters between compact object binaries and the supermassive black hole are a plausible occurrence. Tidal disruptions resulting from these encounters have been proposed as possible sources of extreme-mass-ratio inspirals (EMRIs) and hyper-velocity stars in the galaxy. For disrupted binaries, we show the component of the compact object binary becoming bound to the supermassive black hole have initial eccentricities $\approx 1 - \mathcal{O}(10^{-2})$, but circularize dramatically by the time they enter the classical LISA band, consistent with previous studies. Surviving binaries also merit attention as they will suffer perturbations to their internal orbital parameters. We show the conditions under which compact object binaries are able to survive the tidal field of supermassive black holes during a parabolic encounter, as well as the distribution of orbital parameters post-encounter. The effect of the tidal field on binaries that remain unbound from the supermassive black hole is to decircularize and shrink them, thus accelerating merger due gravitational radiation emission and increasing the predicted merger rates by approximately 0.25 mergers per year. This work is being prepared for publication in the Astrophysical Journal.[1]

4.1 Introduction

Gravitational waves (GW) will provide new probes of dynamic astrophysical systems in regimes where strong gravity plays a role. In galactic nuclei, stellar mass interactions with supermassive black holes (SMBH) will be a good probe, not only of the properties of the SMBH, but also of the stellar population itself. Our own galactic center (GC) is the easiest to study and can provide insight into the types of encounters we can expect, and the frequency of observable GW events.

Previous studies of encounters between stellar mass binaries and a galactic SMBH have focused on the generation of hyper-velocity stars (HVS) and stellar collisions (Hills 1988;

---

[1] Coauthored by Eric Addison, Shane L. Larson, and Pablo Laguna.

Gualandris et al. 2005; Antonini et al. 2010), and the eccentricity of EMRIs created by tidal separation (Miller et al. 2005) (hereafter M05). More recently, these interactions have been explored in the context of the GW emissions in the LIGO band from binaries driven to merger by Kozai resonance (Antonini & Perets 2012; Antonini et al. 2014).

The strongest GW sources will involve compact, degenerate stellar remnants that can survive close encounters with the central black hole, namely neutron stars and stellar mass black holes. The fraction of field stars in binaries varies by stellar type, but for O- and B-type stars, which are the stellar types massive enough to form neutron stars or black holes, it is estimated that more than 75% of O-type and 70% of B-type stars have some number of companions (Raghavan et al. 2010). Near the GC, the density of stars grows very large compared to field conditions, with density estimates up to $10^8 M_\odot$ pc^{-3} within the inner 0.1pc (Alexander 2005). Given this information, it is reasonable to expect the existence of compact object (CO) binaries in the GC, and, in fact, it has been observed by way of X-ray transients that CO binaries exist near the GC, and are more abundant within the inner 1 pc (Muno et al. 2005). It has been estimated that as many as $\sim 20,000$ stellar mass BH binaries have segregated within the inner ≈ 1 pc of the Milky Way GC (O'Leary et al. 2009).

With the existence of CO binaries near the GC, it is reasonable to expect some number of them may interact directly with the SMBH. Many known main sequence stars exist in bound orbits around the SMBH (Ghez et al. 2005, 2008, 2009), suggesting the same could be true for COs and CO binaries. Such interactions have implications for gravitational wave (GW) observation campaigns, for example ground-based observatories (e.g., LIGO) searching for compact binary coalescences (CBC). Proposed space-based interferometers (e.g., LISA) will be sensitive to EMRIs, which can be created by the tidal disruption of CO binaries near the SMBH.

In this study we complement previous work by extending the results of M05 for the formation of EMRIs by tidal disruption to arbitrary binary orientations, as well as classifying and examining surviving binary systems after the SMBH encounter with respect to the merger lifetime from GW emission, the so-called Peters' lifetime (Peters 1964), and estimating the impact on predicted CBC rates. We consider a significantly different section of parameter space than the previous GW studies, focusing on CO binaries that are on initially parabolic orbits with the SMBH with $e = 1$ and varying orbital angles and pericenter distance, where Antonini & Perets (2012) focused on binaries bound to the SMBH at a fixed orientation, and M05 explored hyperbolic encounters with coplanar binaries. The exploration of a greater volume of the parameter space comes at the expense of integration sophistication, though the time and distance scales involved in our simulation suggest relativistic effects will not play a significant role for the majority of the parameter range, and Newtonian gravitational forces should suffice.

Resulting systems will be classified into one of four categories:

1. binary disrupted,
2. survived, bound to SMBH, $T > P_\bullet$,
3. survived, bound to SMBH, $T < P_\bullet$, or
4. survived, unbound from SMBH, $T < T_0$,

where T is the resulting binary Peters' lifetime post-encounter, $P_\bullet$ is the period of the bound binary around the SMBH, and T_0 is the original unperturbed Peters' lifetime of the binary. It will be shown that the case of survived and unbound with $T > T_0$ is not possible. We are interested in how the probability of a binary falling into one of these categories could alter the predicted CBC rate by perturbing the merger lifetime.

The remainder of this chapter is organized as follows. Section 4.2 outlines some analytic expectations of the three-body encounter. In Section 4.3 we describe the numerical integration and simulation setup, as well as the parameters that have been used. Section 4.4 presents the simulation results and provides discussion for both the disrupted and surviving populations. Results are discussed in terms of binary disruption and EMRI formation, surviving parameter distributions, and the effect on the Peters' lifetime. An estimate of how these outcomes may affect the estimated CBC rates is also presented.

4.2 Initial Estimates

4.2.1 Tidal Disruption Radius

The tidal disruption radius for a binary, r_t, is defined as the distance inside which a binary will be separated by the tidal force of the SMBH, and has the general form

$$r_t \equiv \left(\eta \frac{M_\bullet}{M_b}\right)^{1/3} a_0, \tag{4.1}$$

where a_0 is the initial semi-major axis of the binary, M_b is the total mass of the binary, $M_\bullet$ is the mass of the SMBH, and η can vary depending on the nature of the encounter. For example, it is found that $\eta \approx 3$ for a circular prograde orbits (M05), $\eta \approx 4$ for weakly hyperbolic prograde orbits, and about half that for retrograde orbits (Hamilton & Burns 1991, 1992).

The functional form in Equation 4.1 can be derived simply by balancing forces. Set a binary with masses m_1 and m_2 in line with a SMBH of mass m_3 such that the three masses are collinear and the binary center of mass a distance R from the SMBH. Assume disruption will occur when the tidal force on the binary due to the SMBH is equal to the internal force between m_1 and m_2 and expand to first order in r/R, where r is the binary separation. This leads to an expression for a circular equal mass binary of

$$r_t \approx \left(4 \frac{m_3}{M_b}\right)^{1/3} a_0. \tag{4.2}$$

4.2.2 Energy Considerations

While the binary is bound, we can assume $r/R \ll 1$, where r is the binary separation distance and R is the distance from the binary center of mass to the SMBH. The total energy of the three-body system can be written to first order in the small quantities r/R and $m/M_\bullet$ as

$$E_{sys} = \frac{1}{2} m(v_1^2 + v_2^2) - Gm\left(\frac{M_\bullet}{r_1} + \frac{M_\bullet}{r_2} + \frac{m}{r}\right) + \mathcal{O}\left(\frac{m}{M_\bullet}\right),$$

$$= E_{\rm cm} + E_b + \mathcal{O}\left(\frac{m}{M_\bullet}\right) + \mathcal{O}\left(\frac{r}{R}\right), \tag{4.3}$$

where r_i and v_i are the speeds and distances of the binary components relative to the SMBH, and $E_{\rm cm}$ and E_b are the binding energies of the binary-SMBH orbit and the binary orbit respectively.

The case of disruption removes energy from $E_{\rm cm}$ and donates it to E_b of an amount $\delta E \geq |E_b|$. After disruption, it is assumed the separation, r, grows to the same scale as r_1 and r_2 such that $r/r_i \gtrsim 1$, then we can write the system energy to first order in $m/M_\bullet$ as

$$E_{sys} = E_{1h} + E_{2h} + \mathcal{O}\left(\frac{m}{M_\bullet}\right), \tag{4.4}$$

where E_{ih} is the binding energy between binary component i and the SMBH. Equating this expression to the original binary binding energy $E_{sys,0} = E_{b0}$, and recalling the parabolic binary-SMBH orbit has $E_{cm} = 0$,

$$E_{1h} + E_{2h} \approx E_{b0} < 0. \tag{4.5}$$

It is clear from the preceeding expression that the possible outcomes of a disrupted binary include both $E_{1h}, E_{2h} < 0$ and $E_{ih} < 0 < E_{jh}$, but exclude the possibility of $0 < E_{1h}, E_{2h}$. This implies the disrupted binary components can either form one bound and one unbound orbit, or two bound orbits. Intuitively this makes sense as the increase in energy required to disrupt the binary can only come from a corresponding decrease in the black hole orbital energy, and maintaining the negative system energy requires at least one component stay bound.

4.2.3 Multipole Expansion of Three-Body Tidal Force

The purpose of this study is to investigate the effect of the tidal field of the SMBH on a compact binary system, and so the tidal force on the binary is a central consideration. The tidal acceleration term, $\ddot{\vec{r}}$, can be expressed as a power series in the small parameter, (r/R), where $\vec{r}$ is the separation vector between two components of a binary system and $\vec{R}$

is the distance from the SMBH to the binary. The expansion is done assuming there is a third body acting on the binary as shown in Figure 4.1.

With the separation vector defined as $\vec{r} = \vec{x}_2 - \vec{x}_1$, we can write

$$\ddot{\vec{r}} = \ddot{\vec{x}}_2 - \ddot{\vec{x}}_1, \tag{4.6}$$

which we can write out in terms of the total acceleration on each mass:

$$\ddot{\vec{r}} = \left[-\frac{GM_\bullet}{x_2^3}\vec{x}_2 - \frac{Gm_1}{|\vec{x}_2 - \vec{x}_1|^3}(\vec{x}_2 - \vec{x}_1)\right] - \left[-\frac{GM_\bullet}{x_1^3}\vec{x}_1 - \frac{Gm_2}{|\vec{x}_2 - \vec{x}_2|^3}(\vec{x}_1 - \vec{x}_2)\right]. \tag{4.7}$$

Substituting in for $\vec{x}_1$ and $\vec{x}_2$ from Equations 3.4 and 3.5, we have

$$\ddot{\vec{r}} = -\frac{GM}{r^3}\vec{r} - GM_\bullet\left(\frac{(\vec{R} + \frac{m_1}{M}\vec{r})}{\left|\vec{R} + \frac{m_1}{M}\vec{r}\right|^3} - \frac{(\vec{R} - \frac{m_2}{M}\vec{r})}{\left|\vec{R} - \frac{m_2}{M}\vec{r}\right|^3}\right), \tag{4.8}$$

where M is the total binary mass $M = m_1 + m_2$. With the useful identity $\nabla_r(1/r) = -\vec{r}/r^3$ (where the ∇_r means taking derivatives with respect to the components of $\vec{r}$), we can rewrite

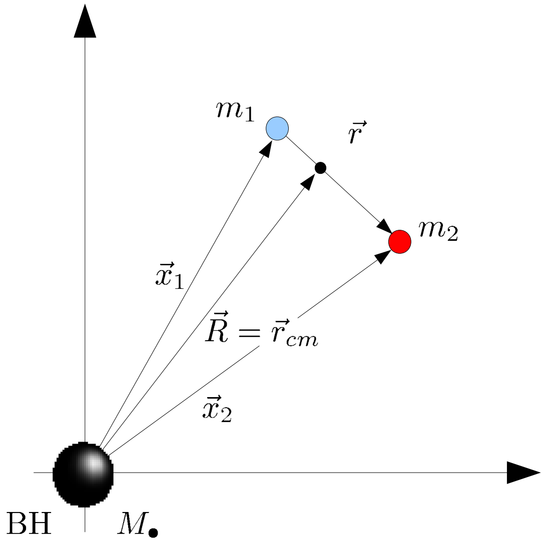

Figure 4.1: Coordinates and relevant vectors for the three-body tidal force problem. Here the black hole is much more massive than the masses m_1 and m_2, so these coordinates keep it fixed at the origin.

this as

$$\ddot{\vec{r}} = -\frac{GM}{r^3}\vec{r} + GM_\bullet \nabla_r \left(\frac{\frac{M}{m_1}}{\left|\vec{R} + \frac{m_1}{M}\vec{r}\right|} + \frac{\frac{M}{m_2}}{\left|\vec{R} - \frac{m_2}{M}\vec{r}\right|} \right). \tag{4.9}$$

Pull out a factor of R from the gradient,

$$\ddot{\vec{r}} = -\frac{GM}{r^3}\vec{r} + \frac{GM_\bullet}{R} \nabla_r \left(\frac{\frac{M}{m_1}}{\left|\hat{R} + \frac{m_1}{M}\frac{\vec{r}}{R}\right|} + \frac{\frac{M}{m_2}}{\left|\hat{R} - \frac{m_2}{M}\frac{\vec{r}}{R}\right|} \right), \tag{4.10}$$

and write out the fractions in the gradient as

$$\frac{1}{\left|\hat{R} + \frac{m_1}{M}\frac{\vec{r}}{R}\right|} = \left[\left(\hat{R} + \frac{m_1}{M}\frac{\vec{r}}{R}\right) \cdot \left(\hat{R} + \frac{m_1}{M}\frac{\vec{r}}{R}\right)\right]^{-1/2} = \left[1 + \left(\frac{m_1}{M}\frac{\vec{r}}{R}\right)^2 + 2\frac{m_1}{M}\frac{r}{R}\cos(\varphi)\right]^{-1/2}, \tag{4.11}$$

where φ is the angle between $\vec{r}$ and $\vec{R}$, and $\hat{R} = \vec{R}/R$. Now, take note of the Legendre polynomial identity, which can be shown by using a binomial expansion and collecting powers of Z

$$(1 - 2XZ + Z^2)^{-1/2} = \sum_{n=0}^{\infty} Z^n P_n(X), \tag{4.12}$$

which is valid for $|X| \leq 1$ and $|Z| \leq 1$, and $P_n(X)$ is the nth Legendre polynomial. We identify $Z = -(m_1/M)(r/R)$ and $X = \cos(\varphi)$, and so

$$\frac{1}{\left|\hat{R} \pm \frac{m_i}{M}\frac{\vec{r}}{R}\right|} = \sum_{n=0}^{\infty} \left(\mp\frac{m_i}{M}\frac{r}{R}\right)^n P_n[\cos(\varphi)]. \tag{4.13}$$

Now insert this back into Equation 4.10 to find

$$\ddot{\vec{r}} = -\frac{GM}{r^3}\vec{r} + \frac{GM_\bullet}{R}\nabla_r \left(\sum_{n=0}^{\infty} \left[(-1)^n \left(\frac{m_1}{M}\right)^{n-1} \left(\frac{r}{R}\right)^n + \left(\frac{m_2}{M}\right)^{n-1} \left(\frac{r}{R}\right)^n \right] P_n[\cos(\varphi)] \right) \tag{4.14}$$

$$= -\frac{GM}{r^3}\vec{r} + \frac{GM_\bullet}{R} \sum_{n=0}^{\infty} \left[\frac{(m_2)^{n-1} - (-m_1)^{n-1}}{M^{n-1}} \right] \nabla_r \left[\left(\frac{r}{R}\right)^n P_n\left(\frac{\vec{r} \cdot \vec{R}}{rR}\right) \right], \tag{4.15}$$

where $\cos(\varphi)$ has been written as $(\vec{r}\cdot\vec{R})/(rR)$. For an equal mass binary this reduces to

$$\ddot{\vec{r}} = -\frac{GM}{r^3}\vec{r} + \frac{GM_\bullet}{R}\sum_{n=0}^{\infty}\left(\frac{1}{4}\right)^{n-1}\nabla_r\left[\left(\frac{r}{R}\right)^n P_n\left(\frac{\vec{r}\cdot\vec{R}}{rR}\right)\right]. \tag{4.16}$$

The tidal force acting on the binary from the SMBH in our simulations is then given by

$$\vec{F}_{tid} = \vec{F}_{\bullet 2} - \vec{F}_{\bullet 1} = m\ddot{\vec{r}} + \frac{GM}{r^3}\vec{r} = \frac{GmM_\bullet}{R}\sum_{n=0}^{\infty}\left(\frac{1}{4}\right)^{n-1}\nabla_r\left[\left(\frac{r}{R}\right)^n P_n\left(\frac{\vec{r}\cdot\vec{R}}{rR}\right)\right]. \tag{4.17}$$

4.2.4 Perturbed Eccentricity

An analytic result for the perturbed eccentricity after an encounter between a binary system and a third body has been derived by Heggie & Rasio (1996) (hereafter HR96). The result is derived by integrating the time derivative of the eccentricity vector of the binary in the presence of a tidal acceleration due to the third body. The tidal acceleration is expressed as a multipole expansion in powers of $(r/R)^n$ (see Section 4.2.3), and the final results are presented for the $n = 2$ and $n = 3$ terms. In the case of an initially circular equal mass binary on a parabolic orbit around a third body, the leading order term has $n = 3$ and is given by

$$\begin{aligned}\delta e = {} & 3\sqrt{2\pi}\frac{m_3 M_b^{1/4}}{M_{tot}^{5/4}}\left(\frac{2r_p}{a_0}\right)^{3/4}\exp\left[-\frac{2}{3}\left(\frac{2M_b}{M_{tot}}\right)^{1/2}\left(\frac{r_p}{a_0}\right)^{3/2}\right] \\ & \times\cos^2\frac{\iota}{2}\left[\cos^4\frac{\iota}{2} + \frac{4}{9}\sin^4\frac{\iota}{2} + \frac{4}{3}\cos^2\frac{\iota}{2}\sin^2\frac{\iota}{2}\cos\phi\right]^{1/2},\end{aligned} \tag{4.18}$$

where $M_b = m_1 + m_2$, $M_{tot} = M_b + m_3$, r_p is the pericenter distance for the orbit of the binary around m_3, ι is the relative inclination of the two orbits, and ϕ depends on the initial phase of the binary and the longitude of the ascending node. This expression will be compared against simulation results in Section 4.4.4. Note this term vanishes as inclination $\iota \to \pi$, so at high inclinations, the higher order terms in the multipole expansion will dominate the change in eccentricity and this expression loses validity. Additionally, as r/R grows, higher order terms may become nonnegligible as well. Given these considerations, we expect to see stronger agreement between simulation results and Equation 4.18 for the low inclination and large pericenter regime.

4.3 Numerical Experiments

4.3.1 Numerical Runs

Fully integrated, three-body interaction simulations are used to study the effects of encounters between a CO binary and a galactic SMBH (black hole orbit). The outcomes of these simulations provide insight into the range of final states the binary can attain after such an encounter. Integration of the Newtonian Equations of motion is performed using Burlish-Stoer extrapolation with a leap-frog integrator as described in Mikkola & Tanikawa (1999), and the accuracy is increased by the use of the CHAIN concept a la Mikkola & Aarseth (1993). The coordinate system used for the numerical integration are barycentric coordinates with the three-body center of mass at the origin. The z-axis is normal to the plane of the black hole orbit, and the x-axis points toward the SMBH at pericenter. Figure 4.2 displays this coordinate system for clarity, but note the parabolic paths are not to scale. Figure 4.3 shows a flowchart describing the general execution flow of the code.

The center of mass of the binary is set in a parabolic orbit around the SMBH, with initial separation set to $200r_p$, where r_p is the pericenter distance of the black hole orbit.

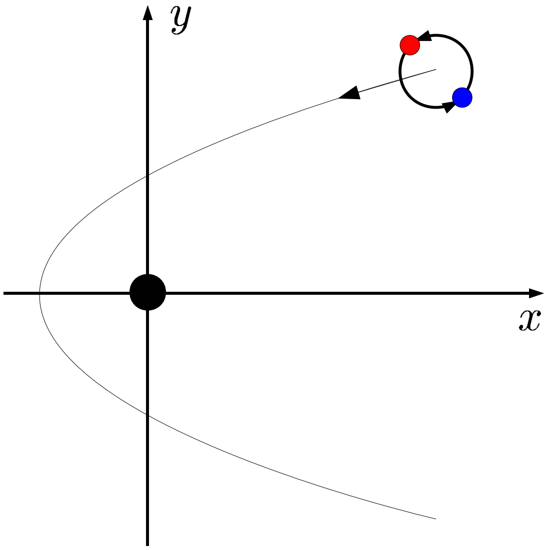

Figure 4.2: Coordinate system used for numerical integration.

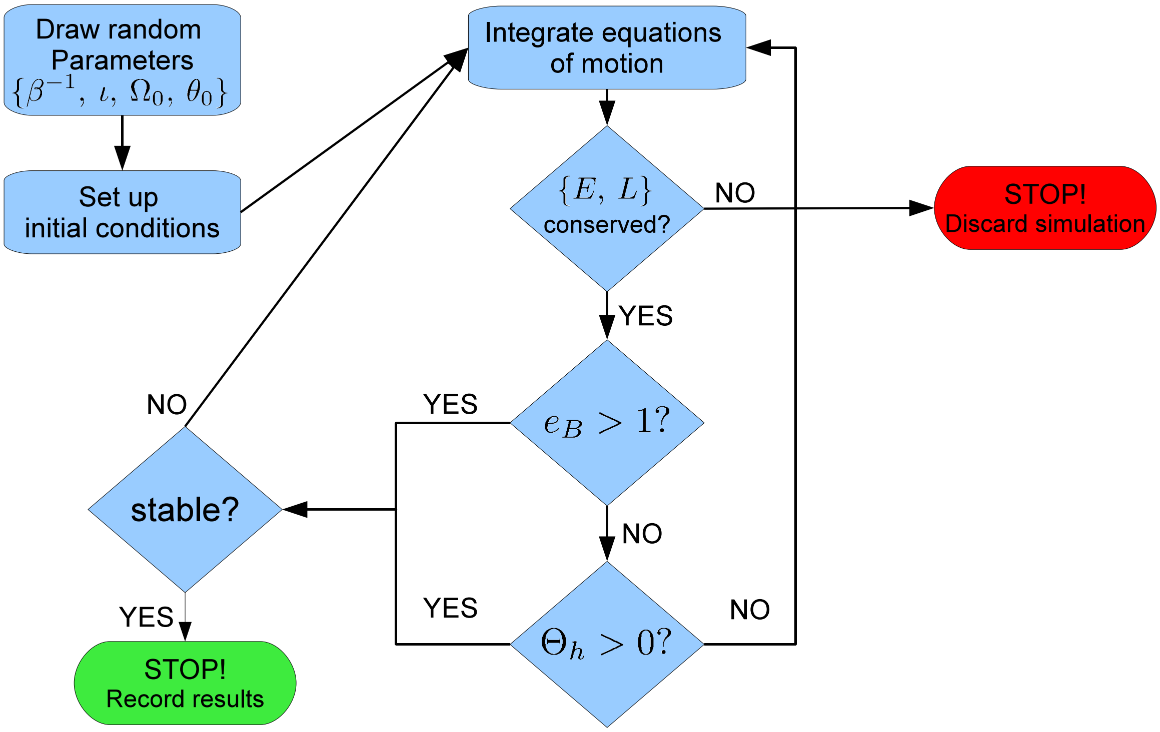

Figure 4.3: Binary-SMBH encounter simulation flowchart. The simulation begins by drawing random parameters and setting up initial positions and velocities of the three masses. The equations of motion (EOM) are then integrated using an adaptive step size leap-frog integrator. At every time step, energy and angular momentum conservation are checked, followed by checks for binary disruption and pericenter passage. If all tests fail, then the EOM are integrated again and the simulation continues. If the binary is disrupted or pericenter has been passed, then the three-body system is checked for stable parameters. If the orbital parameters have stabilized (remained constant over the last several time steps), then the simulation is halted and the results are recorded. If not, the integration continues.

All masses are scaled by the binary component mass m_1 and the integration is carried out with fundamental constants set to unity, i.e., $G = c = 1$. The integration runs until either the binary is tidally disrupted by the SMBH and an amount of time equal to the initial time passes, or the center of mass of the binary has reached a true anomaly of $\Theta = -\Theta_0$, where $\Theta_0 < 0$ is the initial true anomaly of the black hole orbit. Illustrations of the disruption and survival scenarios are shown in Figure 4.4.

Conservation of energy and angular momentum is checked at every time step, and simulations are halted and rejected if either quantity deviates from the initial value by one part in 10^6.

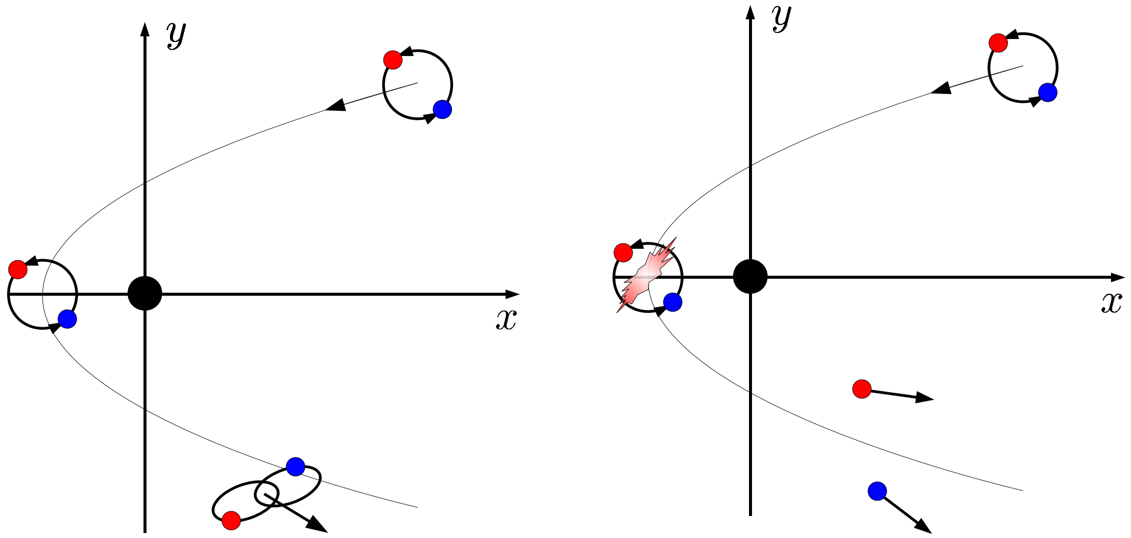

(a) Illustration of a binary surviving the SMBH encounter.

(b) Illustration of a binary being disrupted as a result of the SMBH encounter.

Figure 4.4: Two possible simulation outcomes.

4.3.2 System Parameters

The study is carried out by randomly sampling initial parameters to seed each individual simulation and collecting statistics on the output data points. Input parameters include the binary orbital angles inclination, ι, and longitude of the ascending node, Ω_0, both relative to the simulation coordinates, the binary initial phase, θ_0, and the penetration factor, β, which is related to the tidal disruption radius and the pericenter distance of the black hole orbit by $r_p = \beta^{-1} r_t$.

We adopt a generic definition of r_t from Equation 4.1 with $\eta = 1$ and use this to probe the range of possible disruption radii for varying orientation. Fixed parameters include the component masses $m_1 = m_2 = 10 M_\odot$, as well as the SMBH mass $M_\bullet = 10^6 M_\odot$, the initial binary semimajor axis $a_0 = 10 R_\odot \sim 0.05 AU$, and the initial binary eccentricity $e_0 = 0$. This leaves us with a four-dimensional parameter space, from which β^{-1}, Ω_0, and $\cos\iota$ are sampled uniformly as $\beta^{-1} \sim \mathcal{U}[0.5, 5]$ (where $\sim \mathcal{U}[a, b]$ denotes a uniformly distributed random variable taking values between a and b) corresponding approximately to $r_p \sim \mathcal{U}[0.6AU, 8.5AU]$, $\Omega_0 \sim \mathcal{U}[0, 2\pi]$, and $\cos\iota \sim \mathcal{U}[-1, 1]$, and for each triple (β, Ω_0, ι), θ_0 takes 200 evenly spaced values between 0 and 2π. In addition to the raw parameter distributions, it is also the case that the binary orientation parameters $(\Omega_0, \iota, \theta_0)$ are uniformly distributed with respect to β^{-1}.

Approximately 13,000,000 individual simulations have been run with initial parameters drawn from $(\beta, \Omega_0, \iota, \theta_0)$ space according to the distributions described above.

4.3.3 Relativistic Effects

Basing our study on the Newtonian Equations of motion allows us to quickly explore a large volume of parameter space, but necessarily sacrifices accuracy due to the omission of any relativistic effects. The closest approach between the binary and the SMBH, as well as the largest velocities, occurs at the pericenter passage in the black hole orbit. Given our range of pericenter values, the velocity fraction $v^2/c^2 = (2GM_\bullet)/(c^2 r_p)$ falls between

$$0.002 \leq \frac{v^2}{c^2} \leq 0.039. \tag{4.19}$$

For the smallest values of β^{-1} this implies first order relativistic corrections on the order of

$$\gamma_{rel} = \frac{1}{\sqrt{1 - \frac{v^2}{c^2}}} \approx 1 - \frac{1}{2}\frac{v^2}{c^2} \approx 1 - 0.02. \tag{4.20}$$

That is, to first order the first post-Newtonian correction is only $\approx 2\%$.

The Schwarzchild radius of the $10^6 M_\odot$ SMBH is $r_s \approx 0.02$ AU, so the closest approach in our simulations is about $r_p \approx 30 r_s = 5 r_{ISCO}$. Also neglected is the evolution of the binary semimajor axis due to the emission of GW energy, which we find to be small; however, the slow evolution due to periapsis passage GW emission could be included using the technique of Gair et al. (2006) to slowly evolve the system to the point where these effects are important. The rate at which the semimajor axis of an equal mass circular binary decreases, in the quadrupole approximation, is given by (Peters 1964) as

$$\left\langle \frac{da}{dt} \right\rangle = -\frac{128}{5}\frac{Gm^3}{c^5 a^3}. \tag{4.21}$$

The typical evolutionary timescale of the individual simulations is on the order of several years, with the maximum simulation time at several hundred years. For a binary with $a_0 = 10R_\odot$ and $m_1 = m_2 = 10M_\odot$, the rate of semimajor axis decay is $\langle da/dt \rangle \approx -2.3$ m yr^{-1}, or about $-3.3 \times 10^{-8}\%$ yr^{-1}. Even over a few hundred years, the total change to semimajor axis is less than 1 km or $\approx 1.5 \times 10^{-5}\%$. Precession of the binary periapse is not accounted for, but for a circular binary would only affect the initial phase, θ_0.

For all the relativistic effects, the only one that causes some concern is the velocity fraction for low values of β^{-1}. For completeness' sake we include results for all parameters, but for $\beta^{-1} < 1$ it should be understood that there is potential for $v > 0.1c$, and relativistic effects may become nonnegligible.

4.3.4 Computing Instantaneous Orbital Parameters

In our simulation, the tidal force on the binary components due to the SMBH will cause the binary orbital parameters to change in time. These parameters can include the intrinsic quantities eccentricity, e, semimajor axis, a, internal energy, E, and orbital angular momentum, $\vec{\ell}$, as well as extrinsic quantities, the three orbital angles inclination, ι, longitude of the ascending node, Ω_0, and the argument of periapse, ω_0 (see Figure 4.5a). The rate of advancement of the true anomaly, θ, can change as well, making analytic calculations for θ unreliable.

In Newtonian simulations of gravitationally interacting point masses, the quantities that are explicitly evolved in time are generally the positions and velocities (or momenta) of the components. We can use the separation vector $\vec{r} = \vec{x}_2 - \vec{x}_1$ and the component velocities $\vec{v}_1$ and $\vec{v}_2$ to compute any of the instantaneous orbital parameters for a pair of masses, m_1 and m_2 (see orbit diagram in Figure 4.5b). This can include determining whether or not a given pair of masses is gravitationally bound.

This section will develop algorithms for computing the initial orbital position and momentum, and the instantaneous energy, angular momentum, eccentricity and semimajor axis, as well as the orbital angles of a binary system. These are used in simulation to set up and monitor the time varying orbital parameters between various pairs of masses, which may or may not form bound systems.

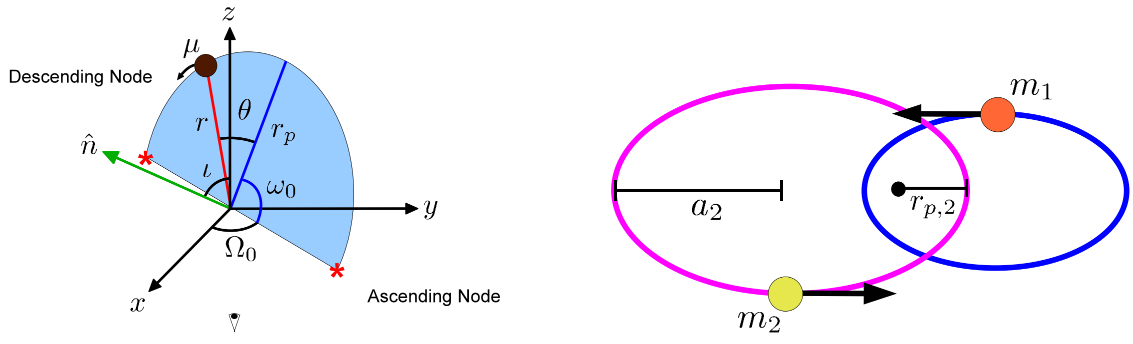

(a) Standard orbital angles.

(b) Orbital path of reduced mass μ and barycentric coordinate system.

Figure 4.5: Orbital parameters for an elliptical orbit.

Initial Orbit Position and Momentum

When computing initial conditions for a simulation, position and momentum must be specified for each component of a binary system. Here, we derive expressions for each of these quantities as a function of the true anomaly, θ, so an initial value of θ will fix the position and velocity values within the orbital plane.

The position of the reduced mass in an orbit is given by the ellipse shape equation

$$r(\theta) = \frac{a(1-e^2)}{1+e\cos(\theta)}, \tag{4.22}$$

where $0 \leq \theta < 2\pi$ is the true anomaly of the orbit, and a is the semi-major axis of the reduced mass orbit.

In the Cartesian coordinate system with origin at the binary center of mass and x-axis pointing toward periapse, we can write

$$x = r\cos(\theta) = \frac{a(1-e^2)}{1+e\cos(\theta)}\cos(\theta), \text{ and} \tag{4.23}$$

$$y = r\sin(\theta) = \frac{a(1-e^2)}{1+e\cos(\theta)}\sin(\theta). \tag{4.24}$$

Then to find the velocity as a function of anomaly, take derivatives (shown for x) as

$$\begin{aligned} \dot{x} = \frac{d}{dt}(r\cos(\theta)) &= \frac{dr}{d\theta}\frac{d\theta}{dt}\cos(\theta) - r\sin(\theta)\frac{d\theta}{dt} \qquad (4.25) \\ &= \dot{\theta}\left(\frac{dr}{d\theta}\cos(\theta) - r\sin(\theta)\right), \qquad (4.26) \end{aligned}$$

where $\dot{\theta} \equiv \dfrac{d\theta}{dt}$ is the instantaneous orbital frequency.

Next, recall the orbital angular momentum $\ell = \mu r^2\dot{\theta}$. Since ℓ is known and constant for a stable orbit, we can replace $\dot{\theta}$ by

$$\dot{\theta} = \frac{\ell}{\mu r^2}, \qquad (4.27)$$

and with this, we have momentum values $p_x = \mu\dot{x}$ and $p_y = \mu\dot{y}$,

$$\begin{aligned} p_x &= \frac{\ell}{r^2}\left(\frac{dr}{d\theta}\cos(\theta) - r\sin(\theta)\right), \text{ and} \qquad (4.28) \\ p_y &= \frac{\ell}{r^2}\left(\frac{dr}{d\theta}\cos(\theta) + r\cos(\theta)\right). \qquad (4.29) \end{aligned}$$

Calculate $\dfrac{dr}{d\theta}$ as

$$\frac{dr}{d\theta} = \frac{d}{d\theta}\left(\frac{a(1-e^2)}{1+e\cos(\theta)}\right) = \frac{ae(1-e^2)\sin(\theta)}{(1+e\cos(\theta))^2} = r\frac{e\sin(\theta)}{1+e\cos(\theta)}, \qquad (4.30)$$

and substitute this into equations 4.28 and 4.29 to find

$$\begin{aligned} p_x(\theta) &= \frac{\ell}{r^2}\left(r\frac{e\sin(\theta)\cos(\theta)}{1+e\cos(\theta)} - r\sin(\theta)\right) = -\frac{\ell}{r}\left(\frac{\sin(\theta)}{1+e\cos(\theta)}\right), \text{ and} \qquad (4.31) \\ p_y(\theta) &= \frac{\ell}{r^2}\left(r\frac{e\sin^2(\theta)}{1+e\cos(\theta)} + r\cos(\theta)\right) = \frac{\ell}{r}\left(\frac{e+\cos(\theta)}{1+e\cos(\theta)}\right). \qquad (4.32) \end{aligned}$$

Finally, substitute equation 4.22 back in for r to find

$$\begin{aligned} p_x &= \frac{-\ell\sin(\theta)}{a(1-e^2)}, \text{ and} \\ p_y &= \frac{\ell[e+\cos(\theta)]}{a(1-e^2)}. \end{aligned} \qquad (4.33)$$

Any orbit is defined by two constants of the motion; (ℓ, E) or (a, e). Here, we have mixed the two sets of parameters for convenience, though only two are actually needed. The expressions in equation 4.33 could be put completely in terms of either pair of parameters using the transformations

$$e = \sqrt{1 + \frac{2E\ell^2}{\mu k^2}} \quad , \quad a = -\frac{k}{2E}, \tag{4.34}$$

$$\ell = \sqrt{\mu k a(1 - e^2)} \quad , \quad E = -\frac{k}{2a}. \tag{4.35}$$

Conservation of momentum in the orbit implies the component masses have momenta

$$p_{1,x} = p_x \qquad \text{and} \qquad p_{1,y} = p_y, \tag{4.36}$$

and

$$p_{2,x} = -p_x \qquad \text{and} \qquad p_{2,y} = -p_y, \tag{4.37}$$

where p_1 and p_2 refer to the momenta of the component masses, m_1 and m_2.

From this, we can identify the anomaly-dependent velocities of each component as:

$$v_{1,x}(\theta) = \frac{p_x(\theta)}{m_1} \quad , \quad v_{1,y}(\theta) = \frac{p_y(\theta)}{m_1} \tag{4.38}$$

$$v_{2,x}(\theta) = -\frac{p_x(\theta)}{m_1} \quad , \quad v_{1,y}(\theta) = -\frac{p_y(\theta)}{m_2}. \tag{4.39}$$

Energy and Angular Momentum

The instantaneous internal energy and angular momentum between a pair of masses are used frequently in this simulation to compute the orbital eccentricity and semimajor axis at any point in time. These quantities can be computed for a pair of masses using the relevant positions and velocities in the global coordinate system, which are the quantities evolved by the simulation.

For any pair of masses, the internal binding energy can be computed as the total energy in the rest frame of the center of mass

$$E_{internal} = \frac{1}{2}m_1(\vec{v}_1 - \vec{v}_{cm})^2 + \frac{1}{2}m_2(\vec{v}_2 - \vec{v}_{cm})^2 - G\frac{m_1 m_2}{r}, \tag{4.40}$$

where the center of mass velocity, $\vec{v}_{cm} = (m_1\vec{v}_1 + m_2\vec{v}_2)/M$, and M is the total mass $M = m_1 + m_2$. Note that

$$\begin{aligned}
\vec{v}_1 - \vec{v}_{cm} &= \vec{v}_1 - \left[\frac{m_1\vec{v}_1 + m_2\vec{v}_2}{M}\right] && (4.41)\\
&= \frac{(m_1+m_2)\vec{v}_1 - m_1\vec{v}_1 - m_2\vec{v}_2}{M} && (4.42)\\
&= \frac{m_2\vec{v}_1 - m_2\vec{v}_2}{M} && (4.43)\\
&= \left(\frac{m_2}{M}\right)(\vec{v}_1 - \vec{v}_2) && (4.44)\\
&= -\left(\frac{m_2}{M}\right)\vec{v}, && (4.45)
\end{aligned}$$

where the relative velocity $\vec{v} = \vec{v}_2 - \vec{v}_1$. Similarly, we have $\vec{v}_2 - \vec{v}_{cm} = \left(\frac{m_1}{M}\right)\vec{v}$. Using these expressions in the internal energy Equation gives

$$\begin{aligned}
E_{internal} &= \frac{1}{2}m_1\left(\frac{m_2}{M}\right)^2 v^2 + \frac{1}{2}m_2\left(\frac{m_1}{M}\right)^2 v^2 - G\frac{m_1 m_2}{r} && (4.46)\\
&= \frac{1}{2}\mu\left(\frac{m_1}{M}\right)v^2 + \frac{1}{2}\mu\left(\frac{m_1}{M}\right)v^2 - G\frac{m_1 m_2}{r} && (4.47)\\
&= \frac{1}{2}\mu v^2 - G\frac{\mu M}{r}, && (4.48)
\end{aligned}$$

where μ is the reduced mass $\mu = m_1 m_2/M$. This is essentially just the one-body reduction; however, here we see the energy equivalence between the binary rest frame and the one-body formulation. Computationally this allows us to calculate the instantaneous internal energy of a pair of masses simply by moving into the rest frame of one of the masses, finding the relative position, $\vec{r}$, and velocity, $\vec{v}$, of the second mass and computing the internal energy as in Equation 4.48. So given the simulation positions and velocities $\vec{x}_1$, $\vec{x}_2$, $\vec{v}_1$, $\vec{v}_2$, the internal energy can be computed by

$$E_{internal} = \frac{1}{2}\left(\frac{m_1 m_2}{m_1 + m_2}\right)(\vec{v}_2 - \vec{v}_1)^2 - G\frac{m_1 m_2}{|\vec{x}_2 - \vec{x}_1|}. \tag{4.49}$$

In a similar manner, the internal angular momentum, $\vec{\ell}_{internal}$, is computed from

$$\ell_{internal} = m_1(\vec{r}_1 - \vec{R}) \times (\vec{v}_1 - \vec{v}_{cm}) + m_2(\vec{r}_2 - \vec{R}) \times (\vec{v}_2 - \vec{v}_{cm}), \tag{4.50}$$

which can be expressed as

$$\vec{\ell}_{internal} = \mu \vec{r} \times \vec{v} = \frac{m_1 m_2}{(m_1 + m_2)}(\vec{x}_2 - \vec{x}_1) \times (\vec{v}_2 - \vec{v}_1). \tag{4.51}$$

Eccentricity and Semimajor Axis

With the internal energy and angular momentum for a pair of masses computed as described above, the eccentricity and semimajor axis between a pair of masses can be calculated directly by the equations in Chapter 3,

$$e = \sqrt{1 + \frac{2E\ell^2}{\mu k^2}} \quad , \quad a = -\frac{k}{2E}, \tag{4.52}$$

where $k = Gm_1m_2$, and $\ell = |\vec{\ell}|$. These expressions allow the simulation to track and output the instantaneous eccentricity and semimajor axis as a function of simulation time, which is shown in Figure 4.6 as used in our SMBH encounter simulation for both a disruption orbit and a surviving orbit, where the strong change in eccentricity can be seen after the close interaction with the SMBH at about $\tilde{t} \approx 0.7$ (normalized time $\tilde{t} = t/T_{max}$) in both panels. For the disrupted binary, the binary eccentricity quickly rises from zero and increases above $e_b = 1$, indicating disruption, while at the same time the eccentricity of the individual components with the SMBH lock into steady values just above and below $e = 1$. The surviving binary shows a significant increase in eccentricity after the interaction, but stays below $e_b = 1$ and is therefore not disrupted.

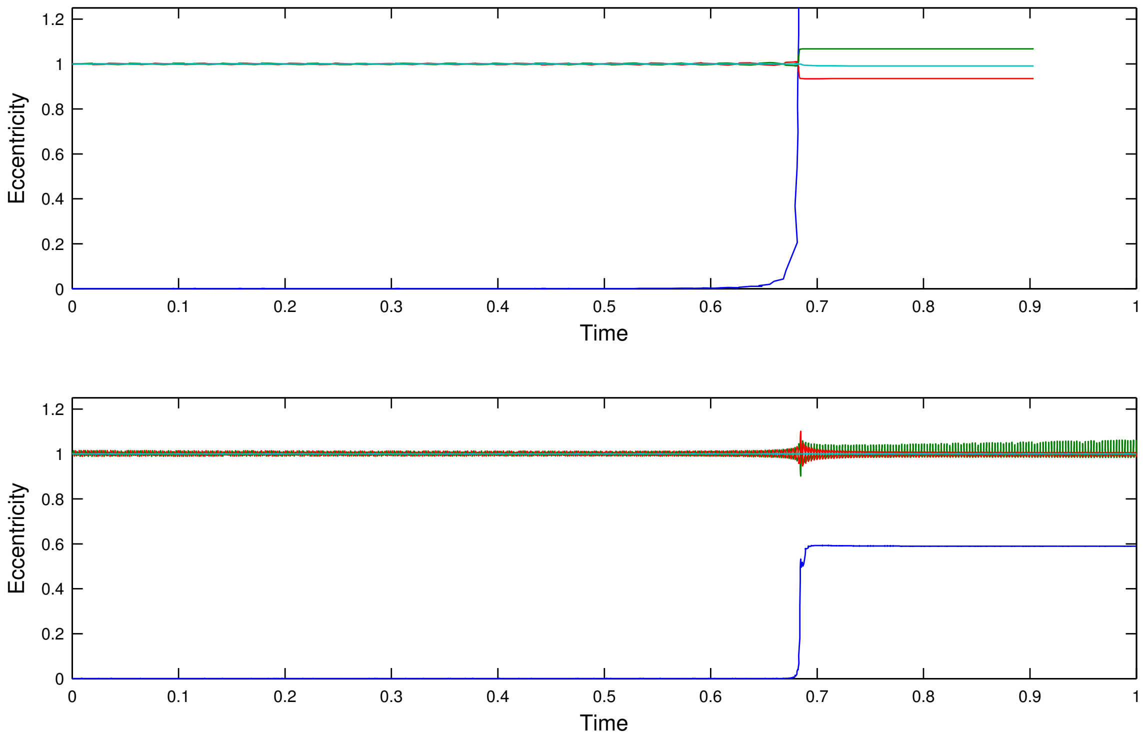

Figure 4.6: Two examples of instantaneous eccentricity tracking with the binary eccentricity in blue, eccentricity between the component masses and the SMBH in red and green, and the center of mass eccentricity around the SMBH in cyan. The top panel displays eccentricities for a disrupted binary, and the bottom for a surviving binary. Time is normalized by the maximum simulation time, $\tilde{t} = t/T_{max}$.

True Anomaly

It is possible to compute the instantaneous true anomaly (orbital phase) between any two masses. This is used in simulation to track the true anomaly of the SMBH orbit. This method relies on the eccentricity vector, which is simply a scaled version of the Laplace-Runge-Lenz vector

$$\vec{e} = \frac{\vec{A}}{\mu k} = \frac{\vec{v} \times \vec{h}}{\tilde{k}} - \frac{\vec{r}}{|\vec{r}|}, \tag{4.53}$$

where $\vec{h}$ is the specific angular momentum $\vec{h} = \vec{\ell}/\mu = \vec{r} \times \vec{v}$, $k = GM\mu$ and $\tilde{k} = GM$. Note that the term eccentricity vector makes sense, as the magnitude is $|\vec{e}| = |\vec{A}|/(\mu k) = \mu k e/(\mu k) = e$. The eccentricity vector is conserved and always points towards pericenter, the angle between $\vec{e}$ and $\vec{r}$ must be the true anomaly θ measured from pericenter. Note in this context where external forces and torques are present, the term conserved should be taken to mean if all external forces and torques were instantly removed, then this vector will maintain constant magnitude and direction in time. The true anomaly is then given by

$$\theta = \begin{cases} \cos^{-1}\left(\dfrac{\vec{e}\cdot\vec{r}}{|\vec{e}|\cdot|\vec{r}|}\right) & \vec{r}\cdot\vec{v} > 0 \\ -\cos^{-1}\left(\dfrac{\vec{e}\cdot\vec{r}}{|\vec{e}|\cdot|\vec{r}|}\right) & \vec{r}\cdot\vec{v} < 0 \end{cases} . \tag{4.54}$$

The $\vec{r}\cdot\vec{v}$ conditions in Equation 4.54 can be understood by considering the dot product of $\vec{r}\cdot\vec{p}$ with the components from Equations 4.22 and 4.33, which is

$$\vec{r}\cdot\vec{v} \propto \vec{r}\cdot\vec{p} = \frac{\ell}{1+e\cos(\theta)}\left(-\sin(\theta)\cos(\theta) + \sin(\theta)[e+\cos(\theta)]\right) \tag{4.55}$$

$$= e\ell\left(\frac{\sin(\theta)}{1+e\cos(\theta)}\right) \tag{4.56}$$

For an elliptical orbit with $e < 1$, this expression is always positive for $0 < \theta < \pi$ and negative for $-\pi < \theta < 0$. For parabolic and hyperbolic orbits with $e \geq 1$, the orbit is defined out to the true anomaly value, θ_∞, where $r \to \infty$, given by $1 + e\cos(\theta_\infty) = 0$. With this definition, we still have the dot product, $\vec{r}\cdot\vec{v}$, positive for $0 < \theta < \theta_\infty$ and negative for $-\theta_\infty < \theta < 0$.

Coordinate Dependent Parameters

The following parameters, which are the orientation angles of the binary, require an external (arbitrary) coordinate system to be properly defined. In an observational setting, this coordinate system could be the sky-plane coordinates described in Section 3.4. For the purposes of this simulation we use the simulation coordinates, i.e., with the z-axis pointing parallel to the initial angular momentum vector of the SMBH orbit, and the x-axis pointing toward the SMBH at periapse (see Figure 4.2).

Inclination

To compute the inclination of the orbital plane with respect to the simulation coordinate system, note the two vectors, $\vec{r}$ and $\vec{v}_1$ (or $\vec{v}_2$), are never parallel, and therefore define the orbital plane. The unit normal vector to the plane of the orbit can then be written as

$$\hat{n} = \frac{\vec{r} \times \vec{v}_1}{|\vec{r} \times \vec{v}_1|}, \tag{4.57}$$

and the inclination angle, ι, can be found by

$$\cos(\iota) = \hat{n} \cdot \hat{z}. \tag{4.58}$$

Longitude of the Ascending Node

The longitude of the ascending node angle can be computed in a straightforward manner by writing the normal vector to the orbital plane as

$$\hat{n} = \begin{bmatrix} n_x \\ n_y \\ n_z \end{bmatrix} = \begin{bmatrix} \sin(\iota)\sin(\Omega_0) \\ -\sin(\iota)\cos(\Omega_0) \\ \cos(\iota) \end{bmatrix}. \tag{4.59}$$

This form follows easily from the sky-plane Equations 3.75, and is also stated explicitly in Larson (2001). By taking the ratio of the first two components of $\hat{n}$, we have

$$\tan(\Omega_0) = \frac{n_x}{-n_y}, \tag{4.60}$$

and so

$$\Omega_0 = \tan^{-1}(-\frac{n_y}{n_x}), \tag{4.61}$$

where the components n_x and n_y are found from Equation 4.57.

Argument of Periapse

Now that the true anomaly, θ, inclination, ι, and longitude of ascending node, Ω_0, can be found, so too can the argument of periapse, ω_0. This is done simply by rotating the

Table 3
Binary End State Classification

Class ID	End State	N_c (millions)
0	Binary disrupted by SMBH	2.1
1	Survived, bound to SMBH with $T < P_\bullet$	1.7
2	Survived, bound to SMBH with $T > P_\bullet$	2.0
3	Survived, unbound from SMBH	7.1

binary plane into the xy-plane, so the separation vector, $\vec{r}$, becomes:

$$\vec{r}\,' = M_x(-\iota)M_z(-\Omega_0)\vec{r} = \begin{bmatrix} r'_x \\ r'_y \\ 0 \end{bmatrix}, \tag{4.62}$$

where M_x and M_z represent CCW rotation operators about the x and z axes respectively by the angles given as arguments. Now the angle between the pericenter position and the vector $\vec{r}\,'$ is the true anomaly θ, so if the angle between the x-axis and $\vec{r}\,'$ is designated β, then the argument of periapse is simply

$$\omega_0 = \beta - \theta. \tag{4.63}$$

4.4 Results and Discussion

4.4.1 Classification and Distributions

The encounter between the binary and SMBH can result in one of four possible end states, which we label class 0 through class 3. Table 3 defines these classes and indicates the number of simulations which resulted in each class.

Each of these classes will be discussed in detail in the following sections. We use the technique of kernel density estimation (KDE) to visualize the probability distribution of each class by assuming independence in the input parameters. KDE is a nonparametric method for estimating probability densities in which a kernel function, $K(x)$, is convolved with a collection of Dirac Delta functions, which asymptotically converges to the true distribution

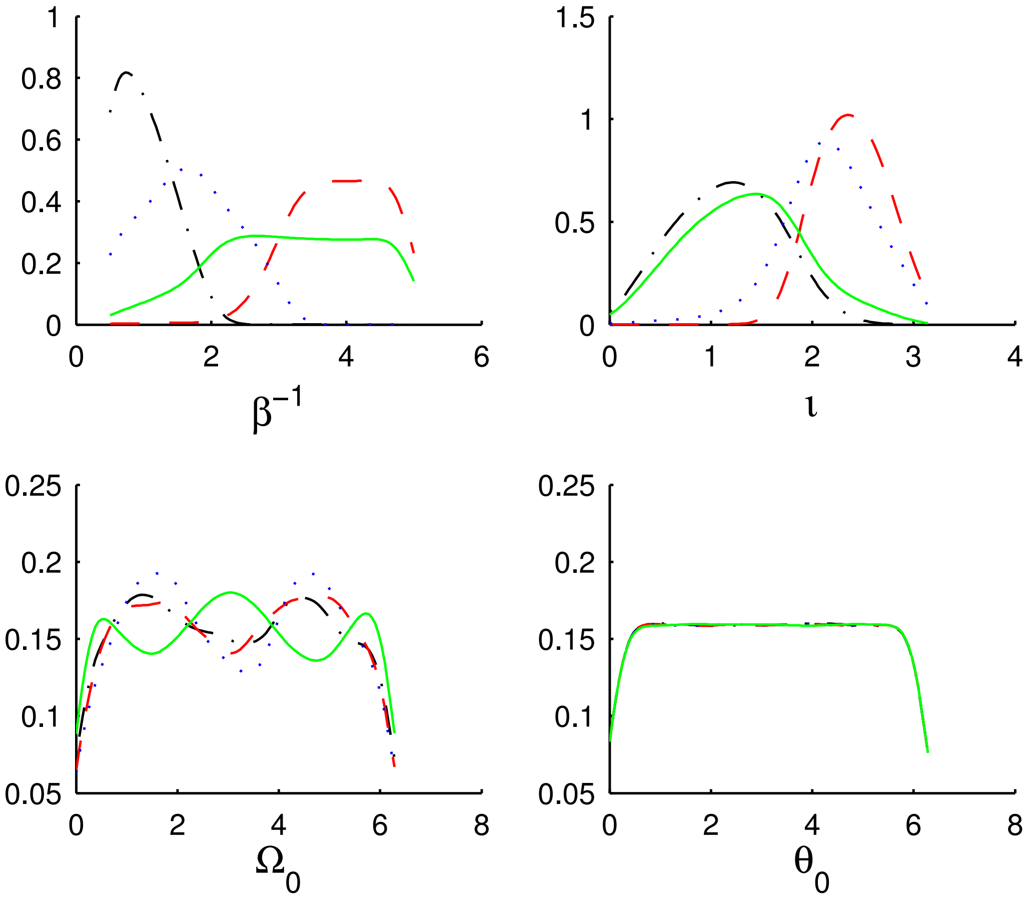

Figure 4.7: KDE results for single parameter probability distributions for each class. The lines-class correspondence is: black-dot/dash-class 0, red-dash-class 1, blue-dot-class 2, green-solid-class 3.

faster than histograms (Scott 1979),

$$f_{KDE}(x) = \frac{1}{N}\sum_{i=0}^{N} K(x) * \delta(x - x_i) = \frac{1}{N}\sum_{i=0}^{N} K(x - x_i), \tag{4.64}$$

where N is the number of data points in the sample. We use a Gaussian kernel, $K(x) = (2\pi h^2)^{-1/2} \exp\left[x^2/(2h^2)\right]$ with a variance of $h^2 = [\text{parameter range}]/100$, chosen to produce distributions that retain structure while not being over-smoothed. The resulting normalized distributions are shown in Figure 4.7.

Based on these distributions, we can draw several conclusions about the nature of the binary end state relative to the input parameters, as well as the predictive power of the individual parameters. It is clear the disrupted (class 0) state occurs primarily with small values of β^{-1}. This should be obvious: closer passes to the SMBH mean stronger tidal forces and higher likelihood of disruption. Additionally, prograde binaries (defined here as those with inclination $\iota < \pi/2$) are more likely to disrupt than retrograde binaries (those with $\iota > \pi/2$). In general, retrograde binaries are more likely to survive and become bound to the SMBH, implying the energy gained by the binary orbit from the black hole orbit is not generally enough to disrupt the binary. It is apparent from the distributions that the parameters β and ι have the largest effect on the binary end state, which will be explored further in subsequent sections. It can be seen here as well, that the longitude of the ascending node, Ω_0, has a weaker but notable effect on the end state, namely a binary is more likely to survive and remain unbound from the SMBH for values of Ω_0 near zero and π. In addition, the initial phase of the binary θ_0 provides no predictive power, as the distributions on this parameter are essentially identical for each class.

4.4.2 Binary Survival and the Tidal Disruption Radius

When a binary passes too close to the SMBH, the tidal force on the binary may be sufficient to unbind or disrupt the binary, resulting in two separate components that are no longer gravitationally bound. These components may become individually bound to the SMBH in highly eccentric orbits, resulting in the classical EMRI scenario, or be ejected at high velocity. Figure 4.8 shows the ratio of surviving and disrupted binaries to the total number of binaries in the corresponding parameter bin, shown for 100 evenly spaced bins in each parameter dimension. The top left panel shows the ratio of surviving binaries vs. β^{-1}, showing that β^{-1} has a strong effect on the probability of survival. The top right panel shows that inclination plays an important role as well, with prograde binaries in general more likely to be disrupted than retrograde binaries. The bottom panels show that Ω_0 has a very weak influence on the survival ratio, though the doubly periodic effect is consistent with the prediction from HR96, and θ_0 has no notable effect.

As a gross statistic, an incoming binary drawn from this parameter space has a 83.8% chance of survival. It can also be seen that the probability of disruption goes to zero for

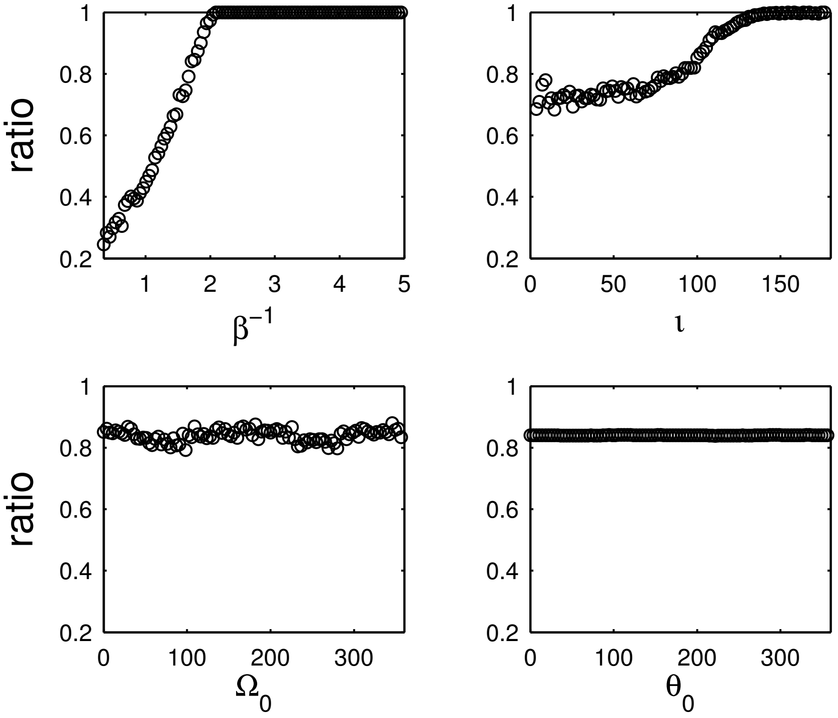

Figure 4.8: The ratio of surviving binaries to the total number of binaries in the corresponding parameter bin.

$\beta^{-1} \gtrsim 2.1$, which is described below.

The tidal disruption radius depends on the orientation of the binary, the nature of the binary-SMBH orbit, and the binary semimajor axis, and is generally taken to be proportional to r_t as defined in Equation 4.1. Our results suggest for a parabolic encounter the maximum possible tidal disruption radius is $r_{t,max} \approx 2.08 r_t$ corresponding to a coplanar prograde binary, and the average over all orientations is $r_{t,ave} \approx 0.95 r_t$.

This result can be compared to the HR96 analytic estimate by determining where Equation 4.18 predicts a change in eccentricity of $\delta e = 1$. This is shown in Figure 4.9 on top of a 2D histogram of tidal disruptions vs. β^{-1} and ι. The parameter ϕ in Equation 4.18 was set to zero as this produces maximum δe. It can be seen that the analytic approximation bounds the region containing disruptions well for $\beta^{-1} \gtrsim 1$, but does not do so well for $\beta^{-1} < 1$ due to higher-order terms in r/R becoming important.

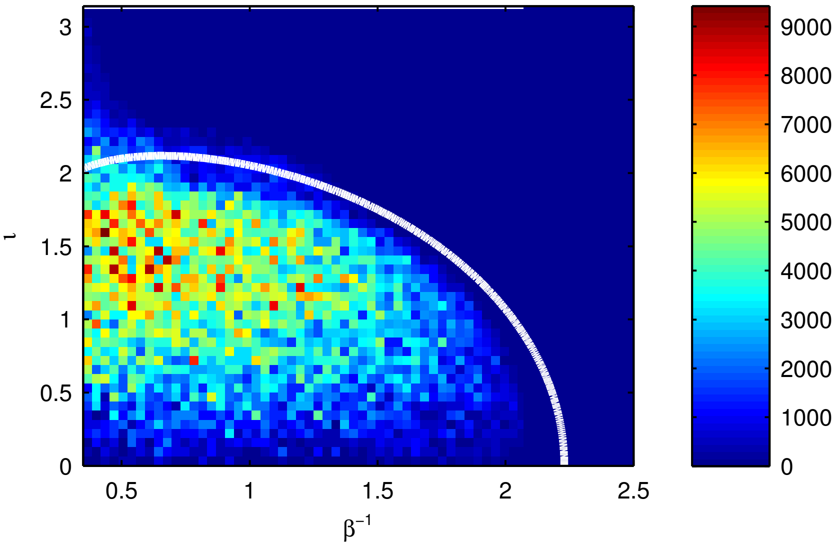

Figure 4.9: 2D histogram of disruptions vs. β^{-1} and ι. Analytic estimate for the disruption radius as a function of β^{-1} and ι shown in white.

4.4.3 The Disrupted Population

The components of the disrupted binaries will either form new elliptical orbits around the SMBH, or remain unbound and continue moving away from the SMBH until either interactions with field stars bring them back to a bound orbit or they leave the influence of the SMBH. Disrupted systems are of interest both in the gravitational wave community as a formation pathway for EMRIs, and in the astrophysics community as a possible source of HVS. In this section we explore the EMRI formation scenario at length, and use previous HVS results as a check for our simulation accuracy.

Energy Considerations in Disruption

Once the binary has been disrupted, the energy of the system can be approximated by Equation 4.4. Figure 4.10 shows a histogram of the energies of the disrupted components, E_{1h} and E_{2h}, while Figure 4.11 shows $E_{2h}/|E_{b0}|$ vs. $E_{1h}/|E_{b0}|$, which fits the line $y = -(x+1)$ very well with a coefficient of determination value of $R^2 \approx 1-10^{-9}$. Our simulation results show the case of two bound orbits after disruption is exceedingly rare, with nearly all disruptions resulting in the one bound and one unbound orbit.

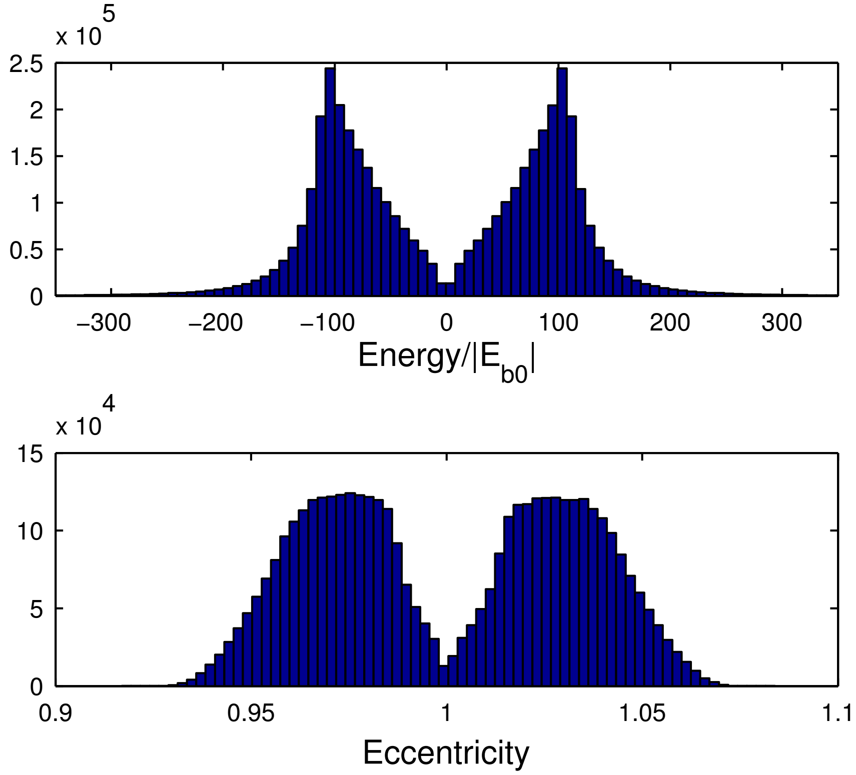

Figure 4.10: Histograms showing binding energy (top) and eccentricity (bottom) distributions of each disrupted component in new orbit around the SMBH.

Due to the parabolic motion of the center of mass of the binary around the SMBH, the binary component masses before disruption are each on a roughly parabolic orbit around the SMBH as well, with pericenter distance comparable to $r_p \pm a_0$. The eccentricity histograms in the lower pane of Figure 4.10 indicate that the resulting orbits after disruption typically have $|1 - e_i| < 0.05$, which for the bound orbits implies high eccentricity. Why is there a preference for highly eccentric orbits, as opposed to more circular ones? If we assume the pericenter distance of each orbit does not change dramatically after disruption, that is $r_{p,i} = r_p + \Delta r$, where r_p and $r_{p,i}$ are the pericenter distances before and after disruption ,respectively, and $\Delta r / r_p \ll 1$, then the resulting bound orbit has energy

$$\frac{E_{ih}}{E_{b0}} = \left(\frac{M_\bullet}{m}\right)^{2/3} (1 - e_i)\beta + \mathcal{O}\left(\frac{\Delta r}{r_p}\right). \tag{4.65}$$

This energy takes a maximum value for a circular orbit with $e_i = 0$, for which $E_{ih,max}/E_{b0} \sim$

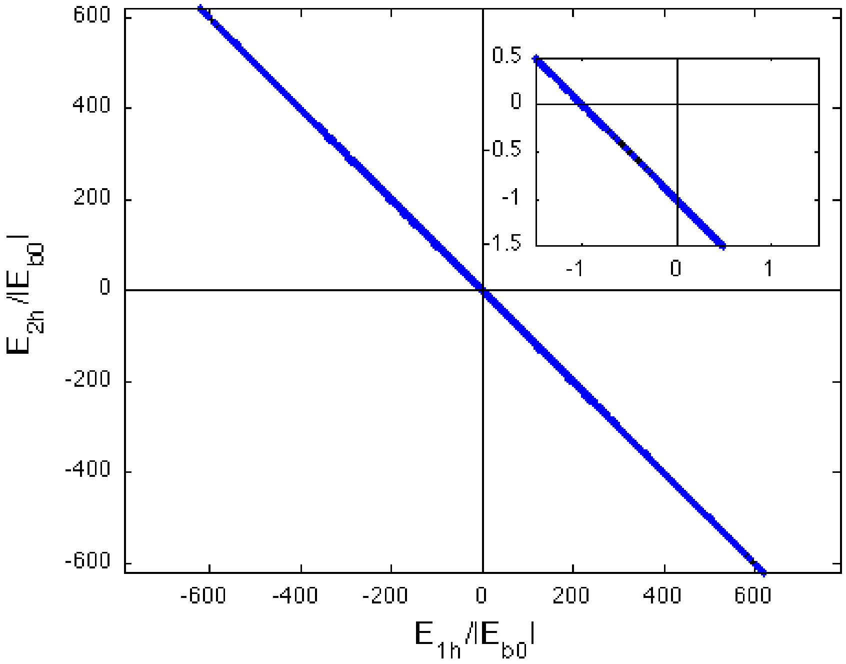

Figure 4.11: E_{2h} vs. E_{1h} for disrupted binaries. The upper right pane shows a zoomed view about the origin, displaying the small region of possible double-bound outcomes.

$\mathcal{O}(10^3)$. For the values of β and resulting eccentricities we see from simulations, this means the typical orbital energies are only on the order $E_{ih}/E_{ih,max} = (1-e_i) \lesssim 5\%$ of the possible energies for a bound orbit with pericenter $r_{p,i} \approx r_p$, and so the preference for highly eccentric orbits stems from the typical scale of energy exchange between the binary components and the SMBH.

We can roughly estimate the amount of energy that will be imparted to the binary components during the close interaction by treating the binary with fixed orbital parameters a and e. Additionally we assume the binary phase evolves linearly with the phase of the black hole orbit, which allows for a simplified expression compared to the true nonlinear phase evolution, and the node passage time $\tau_N \approx 0.5P_b$, which corresponds to $\beta^{-1} \approx 1$. These assumptions allow for a semi-analytical relation, which provides some insight to the simulation results, at least at the level of order of magnitudes. We expand the tidal force on the binary due to the SMBH using the multipole expansion for an equal mass binary

(HR96),

$$\vec{F}_{tid} = \frac{GM_\bullet m}{R} \sum_{n=0}^{\infty} \frac{1}{4^{n-1}} \nabla_r \left[\left(\frac{r}{R}\right)^{2n} P_{2n}\left(\frac{\vec{r}\cdot\vec{R}}{rR}\right) \right], \tag{4.66}$$

and include terms to $n = 2$, with $P_n(x)$ the nth Legendre polynomial. We then integrate to find the difference in work done on each of the binary components during the node passage, assuming the components each follow approximately parabolic paths and the binary disrupts at pericenter, i.e.,

$$\Delta W = \int \vec{F}_{tid}\cdot\hat{t}\,ds = \int_{-\pi/2}^{0} \left(\vec{F}_{tid}\cdot\hat{t}(\theta)\right)\left(\frac{ds}{d\theta}\right) d\theta, \tag{4.67}$$

where $\hat{t}$ is the tangent vector to the parabolic path and $ds/d\theta$ is the differential arc-length traveled per differential change in orbital anomaly θ. This leads to an approximate expression of the form

$$\frac{\Delta W}{|E_{b0}|} \sim 2.3\left(\frac{M_\bullet}{m}\right)^{1/3}\beta^2 + 0.65\left(\frac{M_\bullet}{m}\right)^{-1/3}\beta^4. \tag{4.68}$$

This expression predicts a difference in work done on the binary components in a prograde black hole orbit of order $\sim 100|E_{b0}|$. If we further assume the amount of work done on the components is equal and opposite and this energy is donated entirely to the newly formed orbit with the SMBH, we find that the individual orbital energies are predicted to fall in the range of $10 \leq |E_{ih}/E_{b0}| \leq 450$ for $0.35 \leq \beta^{-1} \leq 2$, which is compatible with the range of energies seen in Figures 4.11 and is displayed explicitly in Figure 4.12. Inserting these results back into Equation 4.65, we find eccentricities decreasing with β and in the range $0.93 < \tilde{e} < 0.99$, compatible with the observed simulation eccentricities.

The coefficients in Equation 4.68 are for coplanar prograde binaries. For retrograde binaries this estimate predicts coefficients about four times smaller, confirming that retrograde binaries are generally less prone to disruption.

Ejected Components and High Velocity Stars

Hypervelocity stars are stars with large velocities, on the order of hundreds or thousands of km s^{-1}, which may exceed the escape velocity of our galaxy. These stars were predicted

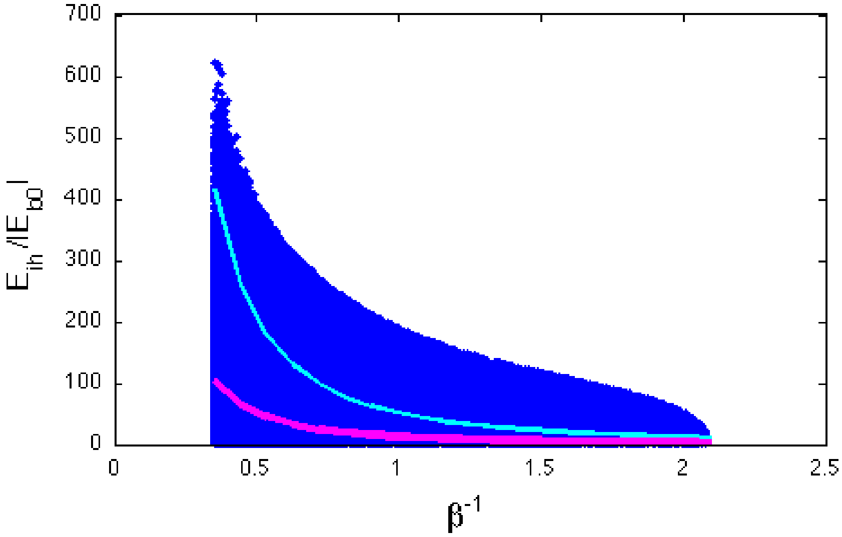

Figure 4.12: Normalized energy $|E_{ih}/E_{b0}|$ vs. β^{-1}. The predictions from Equation 4.68 for prograde binaries shown in cyan, and for retrograde binaries in magenta. The prediction values lie well within the range of possible energy outcomes.

by Hills (1988) as the result of binary disruption in the GC where the ejected component can gain substantial energy, and discovered observationally nearly two decades later (Brown et al. 2005; Edelmann et al. 2005).

The generation of HVS from the tidal disruption of binary systems by a SMBH has been discussed for some time (see references in introduction). Here we show agreement between our simulations and previous results and once again confirm binary disruption as a plausible mechanism for the formation of HVS.

We can use the internal energy of the orbit between an ejected component and the SMBH to find the ejection velocity, i.e.,

$$E_{ih} = \frac{1}{2} m v_{\infty}^2, \tag{4.69}$$

where v_∞ is the velocity of the ejected component at $r_i = \infty$, and then examine the distribution of ejection velocities resulting from tidal disruptions in our simulations. Figure 4.13 plots the complete range of ejection velocities, v_{ej}, converted using Equation 4.69 and the binned average of these velocities with 100 evenly spaced β bins between $0.35 \leq$

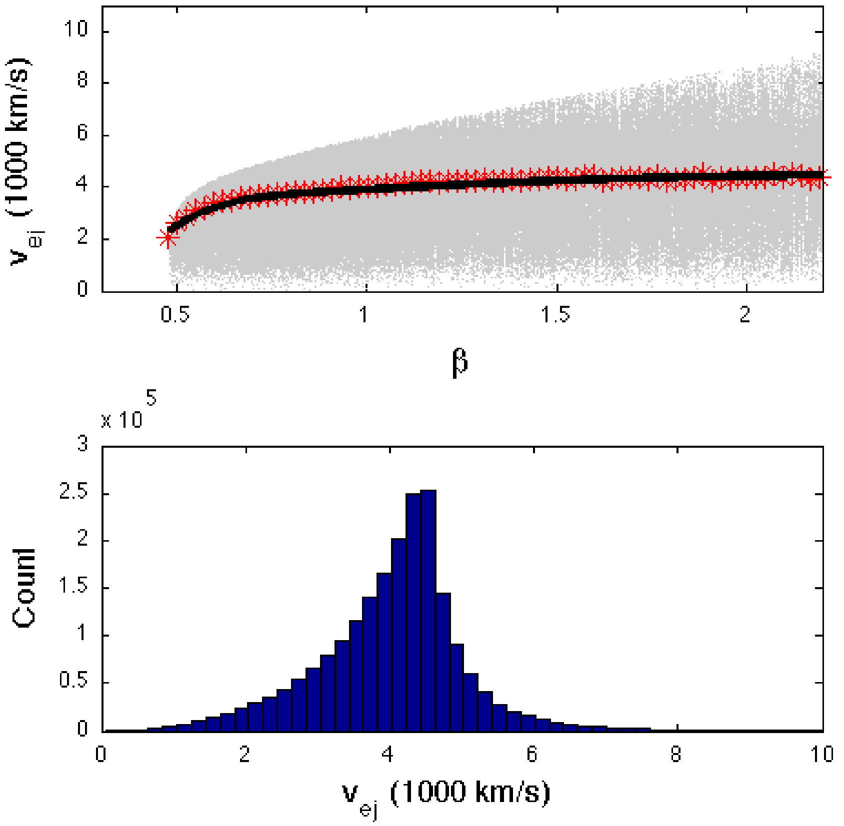

Figure 4.13: Hypervelocity star results. Top panel: plot of ejection velocity for all ejected components in gray, average over 100 β bins as red stars, model prediction in black. Bottom panel: distribution of v_{ej} for all ejected components.

$\beta^{-1} \leq 2.1$. Not only do we predict ejection velocities on the correct order of magnitude, $v_{ej} \sim \mathcal{O}\left(10^3 km/s\right)$, the β-bin average velocities match well to the analytic prediction based on previous numerical studies (Hills 1988; Yu & Tremaine 2003; Antonini et al. 2010), which found

$$v_{ej} \approx 1770 \left(\frac{a_0}{0.1AU}\right)^{-1/2} \left(\frac{M_b}{2M_\odot}\right)^{1/3} \left(\frac{M_\bullet}{3.5 \times 10^6 M_\odot}\right)^{1/6} f_R(D) \text{ km/s}, \tag{4.70}$$

where $f_R(D)$ is a function of the dimensionless closest approach parameter, also known as the Hills' parameter:

$$D = \left(\frac{r_p}{a_0}\right) \left(\frac{2M_\bullet}{10^6 M_B}\right)^{-1/3} = (5 \times 10^5)^{1/3} \beta^{-1}. \tag{4.71}$$

A 5th order polynomial expression for $f_R(D)$ has been fit by Bromley et al. (2006) and found to be

$$f_R(D) = 0.774 + (0.0204 + (-6.23 \times 10^{-4} + (7.62 \times 10^{-6} + \\ (-4.24 \times 10^{-8} + 8.62 \times 10^{-11} D)D)D)D)D. \quad (4.72)$$

The predicted ejection velocity from Equation 4.70 is shown in the top panel of Figure 4.13 as a solid black line. Our averaged results agree with this model with a coefficient of determination value of $R^2 = 0.9033$, though it should be noted that the range of possible velocities can vary significantly from this average, with the largest values roughly double the analytic prediction and nearly 59% of ejections in our simulations exceeding the predicted value.

EMRI Formation

The traditional formation channel for EMRIs is the capture of single stars by the central SMBH by the emission of GW radiation after a close encounter. This occurs when a star passes within the capture radius, which is given by Amaro-Seoane et al. (2007) as

$$r_{capt} = 5r_s \left(\frac{m}{10M_\odot}\right)^{2/7} \left(\frac{M_\bullet}{10^6 M_\odot}\right)^{-2/7} \left(\frac{v}{100 \text{ km s}^{-1}}\right)^{-4/7}. \quad (4.73)$$

This has typical values on the order $r_{capt} \sim 5r_s$. Comparing this to the binary tidal disruption radius, r_{tid}, gives $r_{tid}/r_{capt} \approx 17$. Since binary disruption will always leave a component bound to the SMBH (see Section 4.2.2), it is clear CO binaries can form potential EMRIs with much more distant encounters via tidal disruption than singles via GW capture.

After a disruption, the remaining bound orbit(s) is (are) highly eccentric with average eccentricity $\langle e_{EMRI} \rangle \approx 0.97$. The relationship between the EMRI eccentricity and semimajor axis (or pericenter distance) determines the merger lifetime of the orbit. Figure 4.14 displays the relative frequency of EMRI parameter combinations (a_{EMRI}, e_{EMRI}) and $(r_{p,EMRI}, e_{EMRI})$ as intensity maps, as well as contours of constant β^{-1} and constant

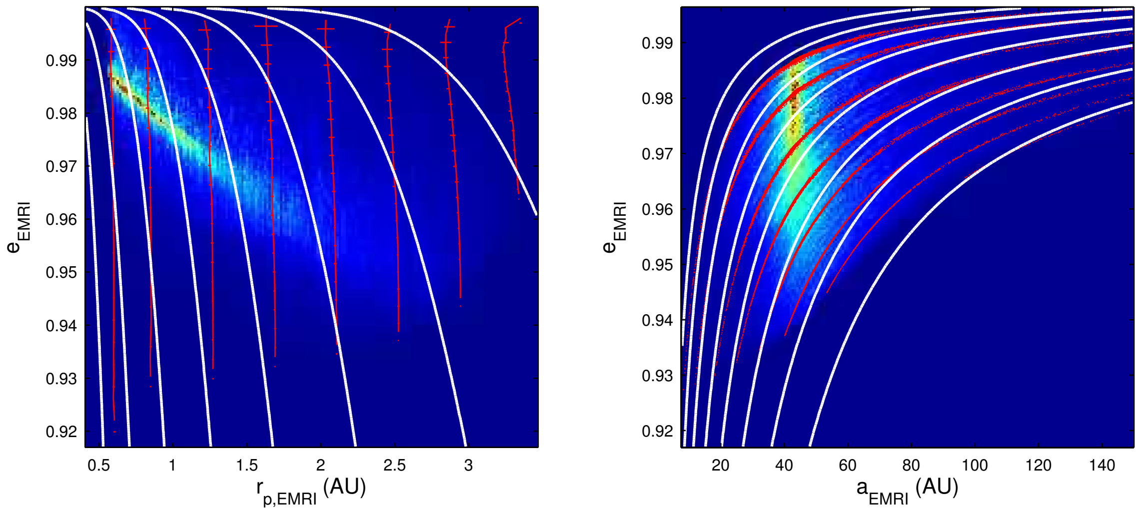

Figure 4.14: 2D histogram of EMRI eccentricity e_{EMRI} vs. pericenter distance $r_{p,EMRI}$ on left, and vs. semimajor axis a_{EMRI} on right. White contours show lines of constant Peters' lifetime with values $T_{EMRI} = 10^{\alpha}$ years, where $\alpha \in \{5.0, 5.5, 6.0, ..., 8.5\}$, increasing from left to right in both plots. Red lines in the left plot show lines of constant β^{-1} binned in eccentricity and averaged over $r_{p,EMRI}$, and associated standard deviations, while the left plot shows the individual points associated with constant β^{-1}. In both plots the values are $\beta^{-1} \in \{0.35, 0.5, 0.75, 1.0, ..., 2.0\}$, and increase from left to right.

merger lifetime. The pericenter distances are tightly correlated with the input parameter β^{-1}, and hence r_p for the original parabolic orbit with typical values $r_{p,EMRI} \lesssim r_p$, which can be seen by the nearly vertical lines of constant β in Figure 4.14.

The EMRIs formed by single capture need to penetrate so deeply into the SMBH potential well that despite circularization from GW emissions, the EMRI can still have significant eccentricity in the LISA band $e \sim 0.5 - 0.9$. It was shown in M05 that while EMRIs formed by tidal disruption of binaries are not expected to contribute significantly to the overall rate of EMRI detections, they will likely have a unique signature in that they will have circularized dramatically by the time they enter the LISA band. This work confirms and extends those results to disruptions of binaries with arbitrary orientations.

Eccentricity in the LISA Band

The EMRIs created from disrupted binaries will gradually circularize and shrink as energy and angular momentum are radiated away in gravitational waves. Given the initial semimajor axis $a_{E,0}$ and eccentricity $e_{E,0}$ of a newly formed EMRI, we compute the eccentricity at which the EMRI orbit will have fundamental frequency f by solving the equation

$$e(f) = \arg\min_{e} |a(e, e_{E,0}, a_{E,0}) - a_{EMRI}(f)|, \tag{4.74}$$

where $a_{EMRI}(f)$ is the semimajor axis of the EMRI when the orbital frequency is $f = 1/P_{orb}$, given by Kepler's third law, and $a(e, e_{E,0}, a_{E,0})$ is the semimajor axis as a function of eccentricity due to the emission of gravitational radiation (Peters 1964),

$$a(e, e_0, a_0) = \frac{c_0(e_0, a_0) e^{12/19}}{(1 - e^2)} \left(1 + \frac{121}{304} e^2\right)^{870/2299}, \tag{4.75}$$

with $c_0(e_0, a_0)$ determined by the condition that $a(e_0, e_0, a_0) = a_0$.

The EMRI eccentricity at frequencies in the LISA band were calculated and averaged, with the result shown in Figure 4.15. This figure shows that in the sensitive LISA band, from about 0.1 mHz $\lesssim f_{GW} \lesssim$ 100 mHz the EMRIs can have an average eccentricity as high as $e_{EMRI} \gtrsim 0.1$. At the most sensitive frequencies, however, at $f_{GW} \lesssim$ 10 mHz, these EMRIs will have typical eccentricities $e < 0.01$, in agreement with M05.

The semimajor axis of these particular EMRIs at $f = 5$ mHz is $a \approx 1.7 r_s$, which is well within the radius of the innermost stable circular orbit, $r_{ISCO} = 6 r_s$ for a nonrotating SMBH, and approaching $\tilde{r}_{ISCO} = r_s$ for a maximally rotating SMBH. In fact, the orbital frequency at which these EMRIs reach r_{ISCO} is at $f_{ISCO} \approx 0.77$ mHz (in the Keplerian approximation), so we should not generally expect these EMRIs to survive to the most sensitive LISA range. Given these factors, a more conservative estimate of the eccentricity of EMRIs formed by binary tidal separation in the LISA band would be $e_{EMRI} \lesssim 0.05$, several times larger than previously thought. While these EMRIs will still have significantly reduced eccentricity in the LISA band compared to their single capture counterparts, it may not reach quite as low as that predicted by M05 due to moving from slow orbital shrinkage to rapid plunge.

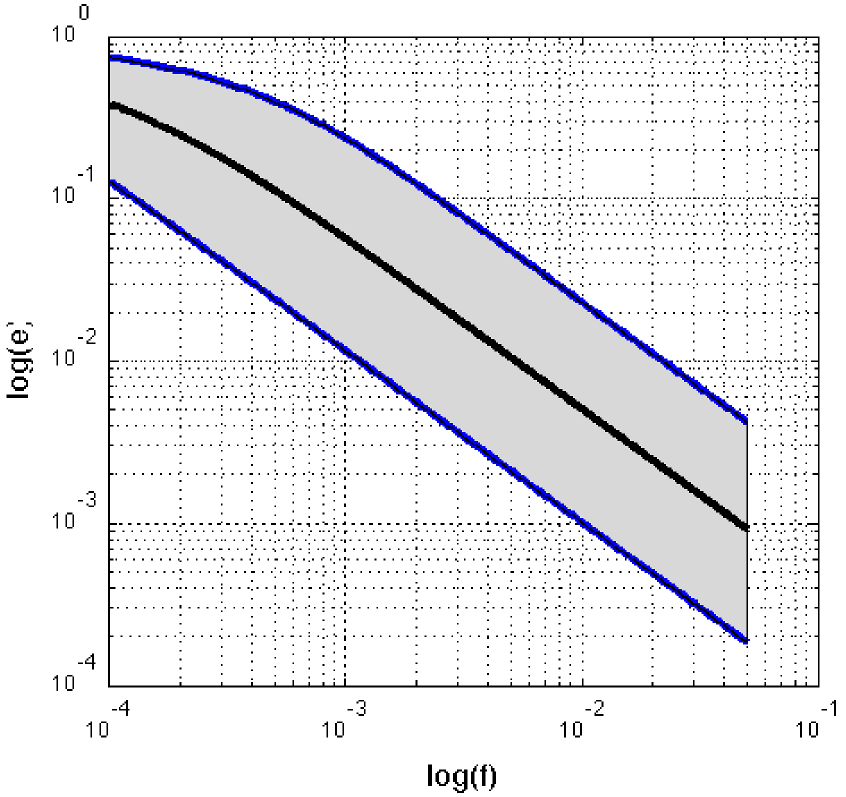

Figure 4.15: EMRI eccentricity at fundamental frequency, f. Eccentricity for individual EMRIs shown in gray, average shown in black. Note that GW energy for nearly circular binaries will be radiated primarily at a frequency $f_{GW} = 2f$.

4.4.4 The Surviving Population

We now turn to the population of binaries that survive the encounter with the SMBH. These binaries make up the majority of the data, given the range of β. The energy exchange is simpler in this scenario: energy is either drained from the black hole orbit and donated to the binary, or vice versa (this follows from Equation 4.3). For this reason, we can expect two general cases of the binary softening and becoming bound to the SMBH, or tightening and remaining unbound. In this section we explore the distributions of orbital parameters of the surviving binaries, with the goal of determining the net change to merger lifetime and whether this leads to detectable changes in the CBC rate observed by detectors like LIGO.

The Effect of Initial Phase

The phase of the binary at the beginning of the simulation represents the most random and unpredictable physical parameter considered in this study, and by all rights should be considered a nuisance parameter. It was previously shown that in general, the initial phase alone provides no predictive power for determining the end state of a given binary. For a particular choice of $(\beta^{-1}, \iota, \Omega_0)$, however, the end state can be highly dependent on θ_0. Since our simulations step through θ_0 in a nonrandom fashion, we can investigate the outcome of a given binary with parameters $(\beta^{-1}, \iota, \Omega_0)$ with respect to θ_0. Figure 4.16 displays the perturbed eccentricity as a function of θ_0 for a selection of binaries with different values of $(\beta^{-1}, \iota, \Omega_0)$, where it can be seen that the variability in the eccentricity due to θ_0 tends to become smaller as β^{-1} increases and the binary orbit becomes more retrograde.

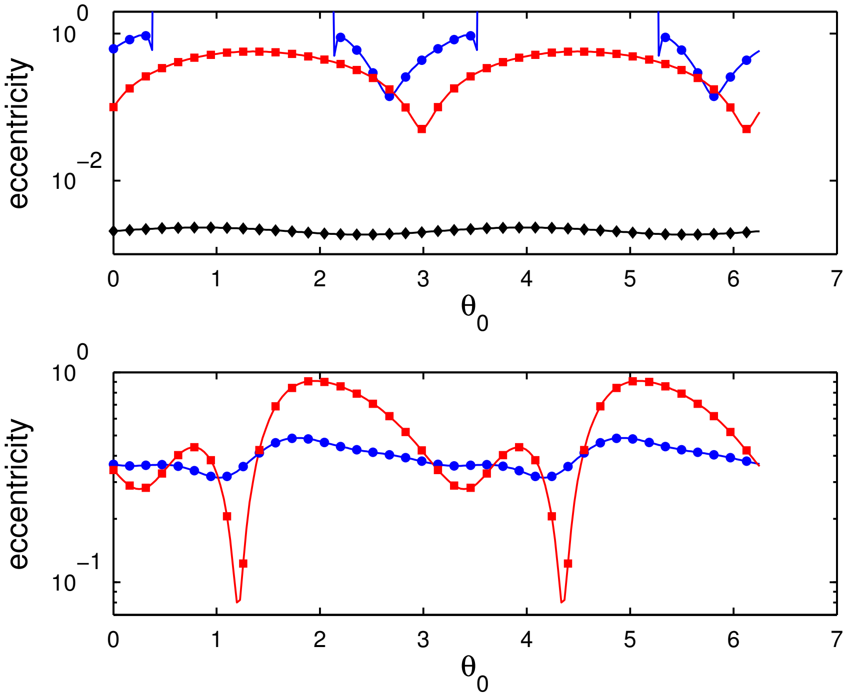

Figure 4.16: Resulting eccentricity of surviving binaries as a function of θ_0. Upper pane: the circles have parameters $(\beta^{-1}, \iota, \Omega_0) = (0.77, 123^\circ, 46^\circ)$, the squares have $(1.9, 101^\circ, 312^\circ)$, and the diamonds have $(4.6, 49^\circ, 152^\circ)$. Points where the curve jumps above 1 indicate disrupted binaries. Lower pane: The binary making a closer pass (circles) generally suffers a reduced perturbation to eccentricity due to the nearly retrograde orbit. The circles have parameters $(\beta^{-1}, \iota, \Omega_0) = (0.57, 177^\circ, 255^\circ)$, the squares have $(1.7, 79^\circ, 308^\circ)$.

Subsequent plots and statistics will be computed by marginalizing over θ_0 and reducing to a three dimensional parameter space.

Final Binary Eccentricity

Eccentricity of the surviving binaries is shown as a histogram in Figure 4.17 along with the cumulative distribution function (CDF) of the eccentricity values. Note the majority of the surviving binaries are relatively unperturbed in eccentricity, with the 65% quantile lying at approximately $e_{65\%} \approx 0.109$ and the 90% quantile at $e_{90\%} \approx 0.553$.

We can compare the simulation results to the analytic estimate for δe from Equation 4.18 by first converting to an Equation in β,

$$\delta e = 3\sqrt{2\pi} g(\iota) \left(\frac{\beta}{2}\right)^{-3/4} \exp\left[-\frac{2\sqrt{2}}{3}\beta^{-3/2}\right] + \mathcal{O}\left(\frac{m}{M_\bullet}\right), \tag{4.76}$$

where $g(\iota)$ contains all of the angular terms from Equation 4.18, averaged over ϕ. The contours of constant $\delta e = 10^\alpha$ for $\alpha \in \{-5.5, -5.0, -4.5, ..., 0\}$ plotted on top of the eccentricity intensity map for β^{-1} and ι with matching contours is shown in Figure 4.18. As expected, we see better agreement between the prediction and simulation results for large β^{-1} and

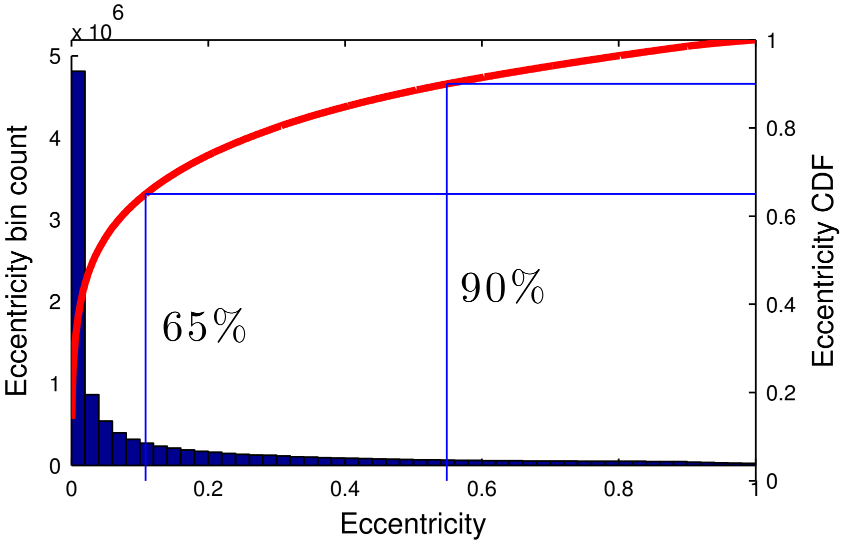

Figure 4.17: Histogram showing final eccentricity distribution with eccentricity CDF shown in red and the 65% and 90% quantiles shown as blue lines.

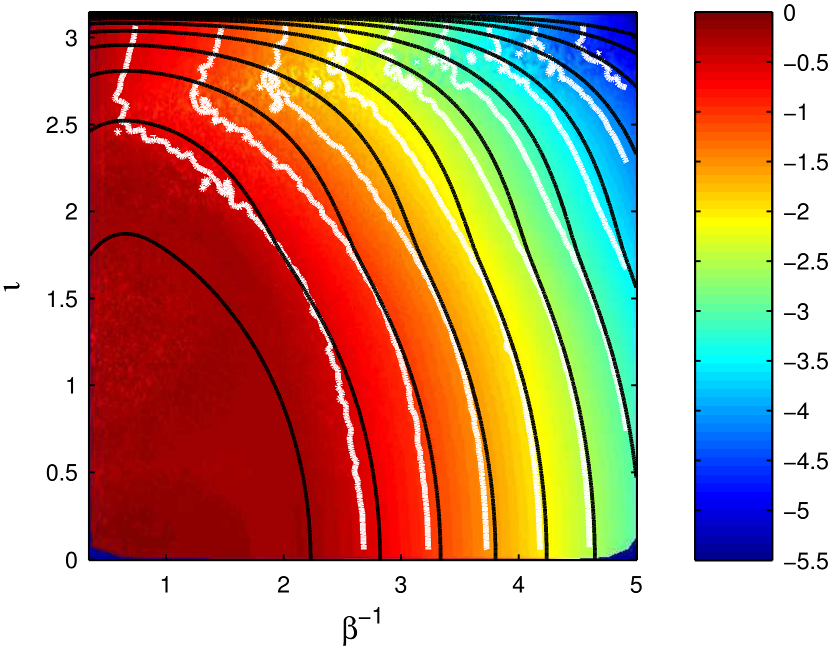

Figure 4.18: Resulting eccentricity $\log(e)$ for surviving binaries plotted as an intensity map vs. β^{-1} and ι. Contours of constant $\delta e = 10^{\alpha}$ for $\alpha \in \{-5.5, -5.0, -4.5, ..., 0\}$ are shown for simulation data in white and for the analytic estimate from Equation 4.76 in black. Note the contour for $\delta e = 1$ is not present for the simulation data. All simulation values have been averaged over θ_0.

small ι. The small overestimation of the prediction at small inclination is consistent with what was found in HR96 for an equal mass binary.

Figure 4.20 plots the perturbed eccentricity values for surviving binaries as 2D intensity maps against the pairs of the three parameters β^{-1}, ι, and Ω_0, averaged over θ_0. Here some of the effects of the individual parameters become clear. As β^{-1} increases, the perturbed eccentricity decreases toward zero; however, even binaries at penetration factors as large as $\beta^{-1} = 3$ can receive a nonnegligible amount of eccentricity, $e \sim 0.2$, after the encounter. Inclination plays a smaller, but important, role in determining the allowable range of final eccentricities, with eccentricity decreasing as the binary orbit approaches retrograde with respect to the SMBH orbit. The longitude of the ascending node, Ω_0, plays no predictable role in the perturbed eccentricity.

Computing overall statistics for eccentricity of surviving binaries gives a mean of $\mu_e = 0.158$ and standard deviation of $\sigma_e = 0.239$.

Final Binary Semimajor Axis

The semimajor axis of the surviving binaries is shown as a histogram in Figure 4.19. This histogram is truncated on the x-axis for better resolution of the central peak, though there are a small number of surviving binaries with substantially increased semimajor axes. It is clear the semimajor axis is generally not perturbed to a strong degree, with the overall mean being $\mu_a = 1.03$. If the sample size is restricted to binaries with final semimajor axes in the range $0.5 < a/a_0 < 1.5$, which accounts for $> 97\%$ of the data and removes the outliers, then the mean is $\tilde{\mu}_a = 0.988$ and standard deviation is $\tilde{\sigma}_a = 0.084$.

Figure 4.21 shows the final semimajor axes as 2D intensity maps over pairs of the input parameters. It can be seen here that for $\beta^{-1} < 2$, the binary can suffer a large change to the semimajor axis, while above this value, the change is small. Inclination has the general effect of tightening the binary for $\iota < \pi/2$, and loosening it for $\iota > \pi/2$. There is some

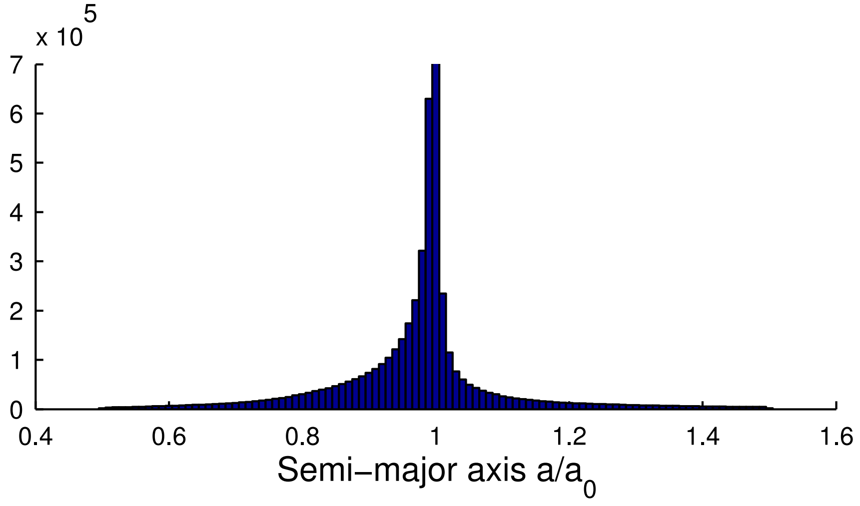

Figure 4.19: Histogram of the binary semimajor axis distribution after SMBH encounter. The horizontal axis has been stretched so the few outliers did not dominate the plot scale, and the vertical axis has been truncated to show detail with the central bin having a true count of $\sim 6.7 \times 10^6$. It is clear the majority of encounters result in very small change in semimajor axis.

variation in the extent of semimajor axis perturbation as a function of Ω_0, particularly when the inclination is around $\iota \approx \pi/2$ or at low values of β^{-1}, with minimum change to a_b at $\Omega_0 \approx \{0, \pi\}$.

The binding energy of the binary is related to the semimajor as $E_b \propto -a_b^{-1}$, and so an increase in a_b results in an increase in E_b and vice versa. This allows us to use Figure 4.21 to identify regions where the energy increases or decreases. From the energy terms in Equation 4.3, it is clear that an increase in binary energy, E_b, must be compensated by a decrease in the black hole orbit energy, E_{cm}, resulting in capture of the binary. Therefore, the points in Figure 4.21 where $a/a_0 > 1$ correspond to binaries that become bound, while $a/a_0 < 1$ indicates binaries that remain unbound.

Final Peters' Lifetime

The Peters' lifetime of a binary system is a measure of how much time it will take for two point masses in a binary orbit to spiral together and reach a separation of zero from the emission of quadrupolar gravitational radiation. This is a standard estimate for the merger lifetime of a physical binary system. The Peters' lifetime for a given binary is computed from the component masses, the eccentricity, and the semimajor axis. The initial binary system used in these simulations has a lifetime of $T_0 \approx 2.37 \times 10^{16}$ s, or 7.5×10^8 years. The resulting lifetimes for all surviving binaries are shown in Figure 4.22.

We can construct four separate categories with respect to the merger lifetime: binaries bound to the SMBH with $T < P_\bullet$, bound with $T > P_\bullet$, unbound with $T < T_0$, and unbound with $T > T_0$, where $P_\bullet$ is the orbital period of the binary around the SMBH, and T_0 is the original unperturbed binary merger lifetime. The last situation is impossible: for the binary to remain unbound from the SMBH, the binding energy, E_b, must decrease, which requires the semimajor axis to decrease as well. This alone would cause the lifetime to decrease, and coupled with increased binary eccentricity further decreases the binary lifetime. Since the initial binary eccentricity is zero, an increase in T would require the semimajor axis to increase, which is not possible in our first-order approximation. All of the unbound binaries will therefore have accelerated merger times due to the encounter.

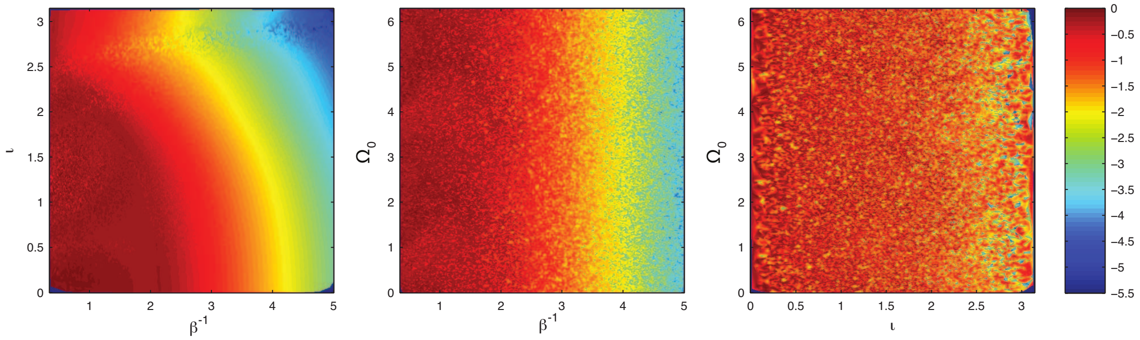

Figure 4.20: Resulting eccentricity $\log(e)$ for surviving binaries plotted as intensity maps vs. pairs of input parameters. All values have been averaged over θ_0.

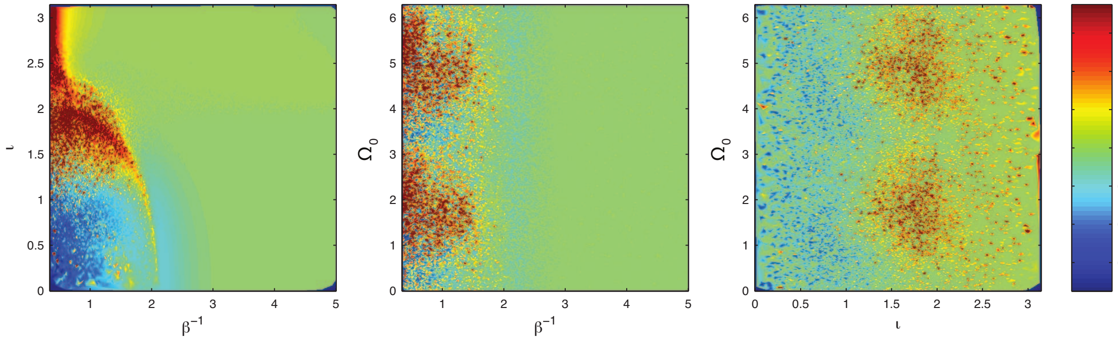

Figure 4.21: Resulting semimajor axis (a/a_0) for surviving binaries plotted as intensity maps vs. pairs of input parameters. All values have been averaged over θ_0.

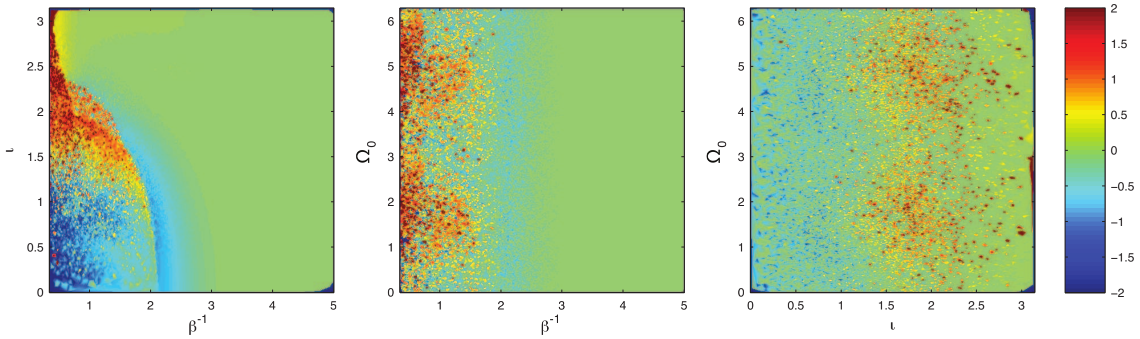

Figure 4.22: Resulting Peters' lifetime $\log(T/T_0)$ for surviving binaries plotted as intensity maps vs. pairs of input parameters. All values have been averaged over θ_0.

BEMRIs

We refer to the population of binaries that become bound to the SMBH as binary extreme mass ratio inspirals (BEMRIs). Because the BEMRI orbits are highly elliptical with average eccentricity $e_{BEMRI} \approx 1 - 10^{-5}$ and long periods, the binary systems have the potential to merge due to GW emission before a single orbit is completed. Analyzing the evolution of the BEMRI systems with $T/P_\bullet > 1$ (short-period BEMRIs) will require careful consideration of GW radiation effects, as the binaries will circularize and shrink by the time they reencounter the SMBH. Careful analysis of the BEMRI systems will be the focus of a future study.

CBC Rate Enhancement

The acceleration of merger lifetimes may have an effect on the CBC rate, and therefore affect the rate at which ground-based GW observatories such as LIGO detect such events. We construct a simple formula to get a first estimate of this effect as

$$\mathcal{E}_{CBC} = [\Gamma * f_b * N_G(D_h)] * (\mathcal{E}_T * f_L), \tag{4.77}$$

where $\mathcal{E}_{CBC}$ is the enhancement to the current predicted CBC rate R_{CBC}, i.e., $\hat{R}_{CBC} = R_{CBC} + \mathcal{E}_{CBC}$. The first three terms in the Equation are observational quantities taken from the literature. Γ is the estimated encounter rate per SMBH per year, f_b is the binary fraction, and $N_G(D_h)$ is the number of Milky Way equivalent galaxies (MWEGs) observable by a GW detector with horizon distance, D_h. The product of these factors is the rate of binary encounters with a SMBH in the observable volume of a GW detector.

The next two factors come from our simulation results. The single binary enhancement $\mathcal{E}_T = (1 - \tilde{T}/T_0)$ is the percent difference between the old merger lifetime, T_0, and the mean new lifetime, $\tilde{T}$, and f_L is the fraction of binaries from our simulations that result in guaranteed LIGO sources after the SMBH encounter. From our data we consider the binaries which are either

1. survived, bound to SMBH, $T < P_\bullet$, or

2. survived, unbound from SMBH,

as these binaries are guaranteed to merge before subsequent encounters (if any) with the SMBH.

Encounter rates in galaxies with a $10^6 M_\odot$ SMBH, estimates for the single CO capture rate range from $\Gamma \sim 5 \times 10^{-9}$ yr^{-1} MWEG^{-1} to as high as $\Gamma \sim 10^{-6}$ yr^{-1} MWEG^{-1} (Hils & Bender 1995; Sigurdsson & Rees 1997; Ivanov 2002; Hopman & Alexander 2005; Merritt et al. 2011); we use the higher side of these estimates, $\Gamma = 10^{-7}$ yr^{-1} MWEG^{-1}, as the pericenter distances in our simulations reach much larger values than the single star capture radius. The binary fraction, f_b, near the GC is not a well determined value, however, in the absence of better knowledge, we take it to be roughly the same as the binary fraction of field stars, $f_b = 0.5$. The number of MWEGs observable by aLIGO with a BH-BH merger horizon distance of $D_h = 2187$ Mpc is given by Abadie et al. (2010); Kalogera et al. (2001) as

$$N_G = \frac{4}{3}\pi \left(\frac{D_h}{\mathrm{Mpc}}\right)^3 \frac{0.0116}{(2.26)^3}, \tag{4.78}$$

which gives a value of $N_G \approx 4.4 \times 10^7$ MWEGs.

From our simulation results, we find that binaries from the f_L categories have a mean Peters' lifetime of $\tilde{T} \approx 0.84 T_0$ giving $\mathcal{E}_T \approx 0.16$ and LIGO fraction $f_L \approx 0.68$.

With all of this, we compute an estimated enhancement to the CBC rate of $\mathcal{E}_{CBC} \approx 0.25$ yr^{-1}. The predicted rate of expected BH-BH mergers has been estimated to lie between 0.4 MWEG^{-1} Myr^{-1} $< \Gamma_{BH} <$ 30 MWEG^{-1} Myr^{-1} for realistic to optimistic scenarios (Kalogera et al. 2007; Abadie et al. 2010). This corresponds to an estimated merger rate within the aLIGO volume of ~ 20 yr^{-1} $< \dot{N}_{BH} <$ 1300 yr^{-1}, which our estimated rate enhancement $\mathcal{E}_{CBC}$ may change by as much as $\approx 1\%$. This enhancement may be difficult to detect with small observation catalogs given the uncertainty in the estimated merger rates, but could become noticeable over long observation times.

4.5 Summary

In this chapter we have presented the results of $\sim 13,000,000$ individual simulations of parabolic encounters between compact circular BH-BH binaries and a galactic SMBH while varying binary orientation and SMBH pericenter distance.

4.5.1 Disruption Results

Tidal disruption of the binary occurs with about 16% probability given our range of parameters. Consistent with previous work in this area, this sort of disruption can create HVS which can escape from the SMBH with high speed. We also explored disruption as a formation mechanism for EMRIs, which are of interest to space-based GW detection missions, and found the EMRIs formed in this way will generally have very low eccentricity when they enter the LISA band. This work shows that considering the full range of possible orientations gives a broader range of formation eccentricities than previous estimates have predicted.

4.5.2 Survival Results

Surviving binaries can either become bound to the SMBH after the encounter or remain unbound. Binaries that become bound to the SMBH are designated BEMRIs; those with a small enough black hole orbital period such that they will not merge before completing one orbit are the short-period BEMRIs, and understanding their full evolution requires a more careful (i.e., Post-Newtonian) approach to the integration in order to account for eccentricity and semimajor axis change due to GW loss during the long orbit. Both the unbound binaries and the long-period BEMRIs, which merge before one SMBH orbit, are factored into the calculation for the CBC rate enhancement, which is potentially important to ground-based GW detectors. We find for the aLIGO volume an enhancement factor for BH-BH mergers of $\mathcal{E}_{CBC} \approx 0.25\ \mathrm{yr}^{-1}$. Despite being a small percentage of the realistic CBC rate predictions, this effect could become meaningful over long observing campaigns.

CHAPTER 5

MEASURING ACCRETION IMPACT RADII WITH OPTICAL AND GRAVITATIONAL WAVE OBSERVATIONS OF COMPACT BINARIES

One of the primary astrophysical sources for space-based gravitational wave observatories will be ultra-compact binary star systems in the Milky Way. Of the millions of such systems in the galaxy, several thousand will be individually resolvable to a spaceborne gravitational wave observatory. For a large number of these systems, multi-messenger observing campaigns with both gravitational wave and electromagnetic telescopes will be possible. The multi-messenger characterization of compact binaries provides a useful synergy of observing capabilities, which can be exploited to recover detailed information about the underlying astrophysical processes in the binary. This chapter describes a novel method for characterizing the accretion discs around the primary in mass transferring binaries using simultaneous photon and gravitational wave observations. The results suggest that for a large number of systems at a variety of inclinations, accretion disc radii can be measured to a precision of better than 5%. This is comparable to measurements using electromagnetic observations of eclipsing systems, but is important because it will work for a much wider range of binary inclination angles, including noneclipsing systems. This work is currently being prepared for publication in the Astrophysical Journal.[1]

5.1 Introduction

The interface between astrophysics and gravitational wave astronomy is an important, emerging area of research as new methods of analyzing and correlating gravitational data with traditional electromagnetic data are found. Of particular interest are ultra-compact binary stars in the Milky Way galaxy. Population estimates based on observed local space densities (Hils et al. 1990; Timpano et al. 2006), as well as population synthesis calculations (Nelemans et al. 2001a,b; Belczynski et al. 2008) suggest that all told, the Milky Way may be populated by as many as 10^7 ultra-compact binaries. This population will be dominated

---

[1] Coauthored by Eric Addison, Shane L. Larson, and Katelyn Breivik.

by white dwarf systems, with fewer numbers of systems where at least one component is a neutron star or stellar mass black hole.

The ultra-compact binaries are characterized by strongly bound components (often mass transferring, or having evolved to their current state through significant periods of mass transfer) and short orbital periods. Binaries with orbital periods of $P_{orb} \sim 10^5$ s to $P_{orb} \sim 1$ s should be easily observable in the gravitational wave spectrum by any future space-based observatory. The archetype of such detectors has been the Laser Interferometer Space Antenna (LISA) (Bender et al. 1998); current design concepts include the European eLISA-NGO (Amaro-Seoane et al. 2013), and the US SGO (Amaro-Seoane et al. 2013; Livas et al. 2012; Stebbins et al. 2012) designs.

The sheer numbers of ultra-compact binary systems are expected to produce a confusion-limited foreground of gravitational waves, which will blanket the gravitational wave spectrum below $f \sim 3$ mHz. An example of the expected level of the confusion limit is shown in Figure 5.1 (Bender & Hils 1997), plotted against the nominal sensitivity curves (Larson 2003) for missions with 5 Gm and 2 Gm armlengths. Strong sources of gravitational waves will rise up above this confusion foreground and be observable by a space-based gravitational wave observatory.

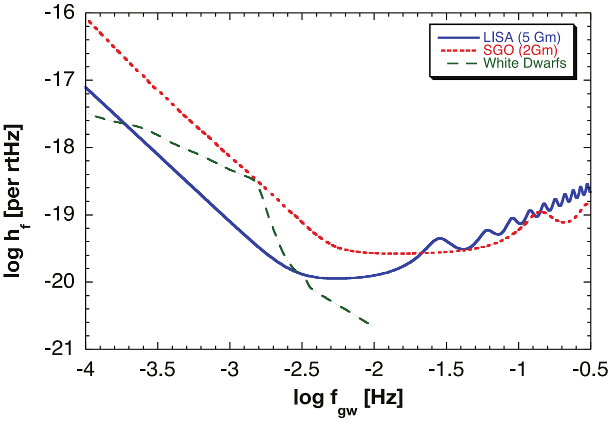

Figure 5.1: The average gravitational wave power spectral amplitude, h_f, of the confusion foreground due to ultra-compact galactic binaries, plotted against the standard sensitivity curve (Larson 2003) for a 5 Gm (LISA) and 2 Gm (SGO) armlength observatory. The assumed bandwidth is one year.

An interesting subset of the ultra-compact binaries are cataclysmic variable stars (CVs), comprised of a primary white dwarf star and a low-mass secondary that has filled its Roche lobe and is transferring mass to the primary; several thousand CVs have been cataloged in the Milky Way (Downes et al. 2001), but a gravitational wave detector in space will be sensitive to as many as 20,000 strewn throughout the galaxy. The disparity in number here is the dim electromagnetic brightness of ultra-compact binary systems, which restricts EM detections to those that lie close to Earth, whereas a gravitational wave detector will detect systems of this sort across the entire galaxy. Already, a growing number of ultra-compact binaries and CVs have been observed and characterized with traditional electromagnetic telescopes (Nelemans 2010), a large fraction of which are a class of helium cataclysmic variables (HeCV) similar to the star AM *Canum Venaticorum* (AM CVn). These systems have primary white dwarfs with low-mass helium companions providing mass flow onto accretion discs of unknown radii. They are expected to be strong gravitational wave radiators.

Realistic simulations on mock data (Babak et al. 2008, 2010) have shown tens of thousands of these stars will be detectable by a space-based gravitational wave detector as individually resolved sources (Crowder & Cornish 2007), and several hundred of those will be simultaneously detectable by electromagnetic telescopes, even for mission designs more modest in scope than LISA (Littenberg et al. 2013). A population of binaries that can be observed with both electromagnetic telescopes and gravitational wave interferometers can be used as probes of the fundamental astrophysics that governs these systems; this multi-messenger mode of observations can reveal information that is difficult or even impossible to extract otherwise.

Models of the accretion discs in HeCV systems have been studied in the past, and suggest the disc radii will be around 75% of the primary Roche radius (Sulkanen et al. 1981a), but this estimate is only certain to within about 10%. Measurements of accretion disc radii in ultra-compact binary systems have been made using eclipsing systems, with results that are accurate to about $\sim 10\%$ (Sulkanen et al. 1981b). Future space interferometry mission concepts (Peterson & Shao 1997; Beichman et al. 1999) may make direct optical imaging of close binary systems (like AM CVn) possible, allowing a direct measurement of the accretion disc radius. This chapter demonstrates how correlating optical observations of a mass transferring CV system with simultaneous gravitational wave observations by a space-based interferometer can yield a measure of the primary accretion disc's radius.

The chapter is organized as follows. Section 5.2 reviews the conceptual model for the electromagnetic lightcurve and the gravitational wave emission from these systems, as well as the multi-messenger comparison. Section 5.3 describes our model for overflow and accretion and our model for the light curve from these systems. Our results and discussion are presented in Sections 5.4 and 5.5.

5.2 Multi-Messenger Signals

5.2.1 The Restricted Three-Body Problem

The general gravitational three-body problem has no analytic solution, and only with the advent of digital computers has any significant progress been made in understanding few-body dynamics (Valtonen & Mikkola 1991). The intractability of the general problem explains why so much work has been done exploring analytic approximations, as well as developing specialized numerical techniques (Mikkola & Tanikawa 1999; Mikkola & Aarseth 1993). When considering the dynamics of a small test mass in the presence of two much larger masses in a binary orbit, however, a case known as the Restricted Three-Body Problem, a solid analytic framework exists (Hellings 1994).

A test mass at rest in the corotating frame of a binary system (a coordinate frame with origin at the center of mass, which rotates along with the binary) will experience both the standard gravitational attraction and a centrifugal force. These forces can be written as the gradient of a single potential function:

$$V(x,y) = -G\frac{m_1}{r_1} - G\frac{m_2}{r_2} - \omega^2\frac{x^2+y^2}{2}, \tag{5.1}$$

where m_1 and m_2 are the masses of the binary components, r_1 and r_2 are the distances between the test particle and the binary components, and ω is the angular speed of binary rotation. This potential function and several equipotential contours are plotted in Figure 5.2.

The white contour in Figure 5.2 defines two separate teardrop-shaped regions, one around each component of the binary. These regions are known as the Roche lobes, and they define the regions where each binary component has the dominant influence. A test mass within the Roche lobe of a binary component is gravitationally bound to that component, while outside of the Roche lobe it may still be bound to the binary system, though not necessarily associated with one component.

Compact binary systems can be tight enough such that the gravitational influence of one component (the primary) causes the other (the secondary) to expand and puff up, filling its Roche lobe. As the secondary star fills its Roche lobe, the stellar material that lies along the boundary of the Roche lobe is free to move along without a change in energy. Material that crosses into the Roche lobe of the primary star (passing through the L_1 Lagrange point) will become bound to the primary and form a stream of matter that flows inward toward the star. The phenomenon of matter flowing from one tidally deformed star onto its companion is known as accretion, the stream of matter is the accretion stream, and the resulting disc that often forms is the accretion disc.

5.2.2 Electromagnetic Lightcurve

Roche lobe overflow through the Lagrange point in ultra-compact binaries will often lead to the formation of an accretion disc around the primary star in mass transferring systems (Lubow & Shu 1975; Paczynski 1977). A model (Warner 1995) that can explain the optical properties of mass-transferring HeCVs has a massive ($\sim 1\mathrm{M}_\odot$) CO white dwarf embedded in an accretion disc as a primary, and a less massive ($\sim 0.02\mathrm{M}_\odot$) helium dwarf that has expanded to fill its Roche lobe. Material spills through the inner Lagrange point, streaming onto the accretion disc and causing a bright hot spot (see Figure 5.3). This hot spot radiates approximately radially outward from the disc; as the binary orbits, the spot alternately turns towards and away from distant observers, modulating the lightcurve. This model has been applied to AM CVn *in extenso* (Faulkner et al. 1972; Patterson et al. 1992,

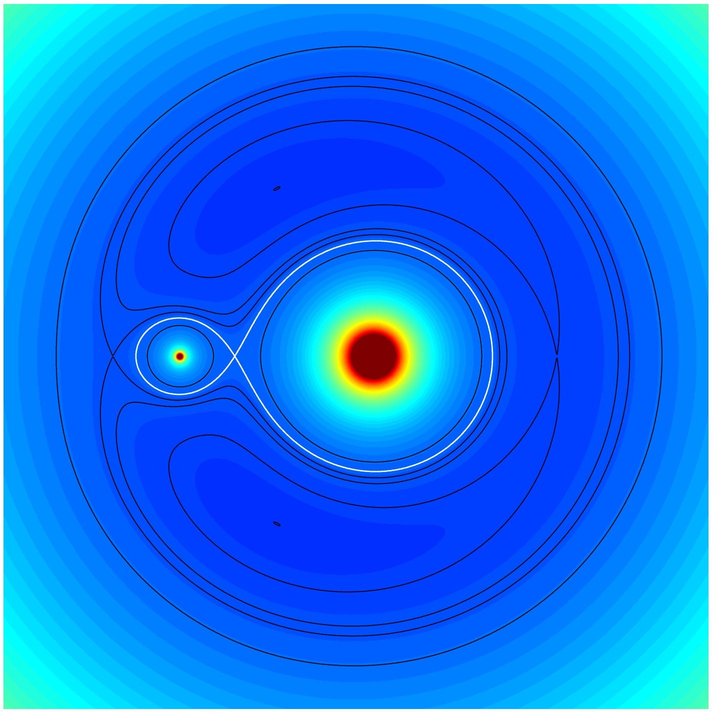

Figure 5.2: The potential and equipotential contours for the restricted three-body problem. Several equipotentials are shown in black. The contour shown in white is the special equipotential line that crosses itself at a point known at the L_1 Lagrange point; one of five points in the corotating frame where the forces on a test mass balance. The teardrop-shaped regions outlined by the white contour are known as the Roche lobes, and each component of the binary has its own Roche lobe.

1993) and successfully describes a variety of signals present in the photometric lightcurve of this star. Photometric observations have measured an orbital period of $\tau_o = 1028.7325 \pm 0.0004$ s (Harvey et al. 1998), confirming previous theoretical predictions (Patterson et al. 1993).

Electromagnetic observation methods exist for determining accretion disc radii from the lightcurve in eclipsing binary systems (Ritter 1980; Sulkanen et al. 1981a). In eclipsing systems, the accretion disc can be occulted by the secondary, and then can itself occult the secondary a half period later. The contact points of the eclipse in the electromagnetic lightcurve encode the exact position of the binary components, and provide solutions for all

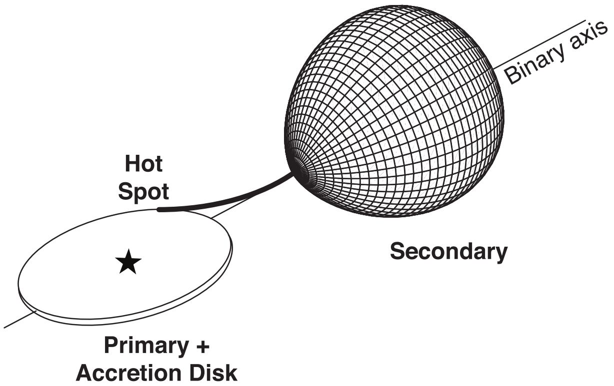

Figure 5.3: The secondary companion has expanded to fill its Roche lobe, which overflows, forming an accretion disc around the white dwarf primary. The point of accretion impact on the edge of the disc creates a electromagnetically bright hot spot.

the geometric parameters of the binary, including the size of the accretion disc. The error expected from these eclipsing methods is $\sim 10\%$, estimated by Sulkanen et al. (1981b).

5.2.3 The Gravitational Wave Signal

The ultra-compact binaries are strong gravitational wave radiators in the millihertz gravitational wave band. In this regime, with orbital periods on the order of several thousand seconds to tens of seconds, the gravitational wave emission is well described by the quadrupole formula (Peters & Mathews 1963; Peters 1964). The gravitational wave emission extracts energy and angular momentum from the binary on long timescales, until ultimately the components merge [for compact stellar remnants like neutron stars and black holes, the merger occurs at high frequencies, in the regime covered by ground-based gravitational wave detectors like LIGO (Harry & the LIGO Scientific Collaboration 2010)]. A particularly useful formulation of the emission from compact binaries utilizing the quadrupole formula is due to (Wahlquist 1987), expressed in terms of standard binary observational parameters (inclination, argument of periapsis, longitude of the ascending node, etc.). The overall strength of the gravitational waves depends on a scaling factor H:

$$H = \frac{4G^2 m_1 m_2}{c^4 a(1-e^2)D} = \frac{4G^{5/3}}{c^4(1-e^2)}\frac{\mathcal{M}}{D}\left(2\pi f_o \mathcal{M}\right)^{2/3}, \tag{5.2}$$

where Kepler's third law has been used to express a in terms of the orbital frequency f_o,

D is the luminosity distance, and $\mathcal{M} = (m_1 m_2)^{3/5}/(m_1 + m_2)^{1/5}$ is the chirp mass of the system. It is expected that compact interacting binaries will have become circularized through mass transfer and common envelope evolution; gravitational wave emission also tends to circularize binaries. For circular binaries, $e = 0$, and the gravitational wave frequency, f, is simply related to the orbital frequency by $f = 2f_o$. Then the scaling amplitude is simply

$$H = \frac{4G^{5/3}}{c^4} \frac{\mathcal{M}}{D} (\pi f \mathcal{M})^{2/3} \ . \tag{5.3}$$

Gravitational wave detectors will detect two polarization states, the strength of which are expressed in terms of the scaling amplitude, H. Using the quadrupole formula for an arbitrarily oriented circular binary gives (see Section 3.5):

$$\begin{aligned} h_+(\theta) &= H(\cos(2\phi)A_0 - \sin(2\phi)B_0), \text{ and} \\ h_\times(\theta) &= H(\sin(2\phi)A_0 + \cos(2\phi)B_0) \ . \end{aligned} \tag{5.4}$$

Here, ϕ can be interpreted as either the binary longitude of the ascending node, or the gravitational wave polarization angle, and

$$A_0 = -\frac{1}{2}[1 + \cos^2(\iota)] \cos 2(\theta - \theta_n), \text{ and} \tag{5.5}$$

$$B_0 = -\cos(\iota) \sin 2(\theta - \theta_n) \tag{5.6}$$

are orientation-dependent functions (additional terms for $e \neq 0$ may be found in section 3.5). The angle θ is the angular position in the orbit (the true anomaly), and θ_n is the value of θ at the line of nodes, which we will set to zero for convenience. In a circular binary, the orbital phase angle, $\theta(t)$, is related to the gravitational phase angle, $\varphi(t)$, by $\varphi(t) = 2\theta(t)$, where $\varphi(t)$ is the phase function of the gravitational wave determined from the orbital dynamics and evolution. The gravitational wave phase for most of the population of ultra-compact binaries is a simple function of the gravitational wave frequency

$$\varphi(t) = ft + \frac{1}{2}\dot{f}t^2 + \phi_0 \ , \tag{5.7}$$

where f and ϕ_0 are the gravitational wave frequency and wave phase at $t = 0$, and $\dot{f}$ is the chirp. The gravitational wave contribution to the chirp, from the quadrupole approximation, is

$$\dot{f} = \frac{96}{5}\pi^{8/3}\frac{G^{5/3}}{c^5}f_0^{11/3}\mathcal{M}^{5/3} \ . \tag{5.8}$$

Astrophysical effects [such as spin orbit interactions (Hut 1981), tidal interactions (Willems et al. 2008) or mass transfer (Deloye & Taam 2006)] will alter the angular momentum in the binary, and thus the orbital period and observed frequency, f_0. The ultimate effect is that there are many competing processes that drive the evolution of angular momentum in the system. It is clear the relative contributions of each physical process will alter the interpretation of the orbital evolution derived from LISA's gravitational wave observations, a matter that will be considered in a future study.

A LISA-like detector will have a frequency resolution related to the mission duration T_{obs} given by $\Delta f = 1/T_{obs}$; this is the frequency bin width for observations. As T_{obs} lengthens, the bin width narrows. In general, a conservative estimate is that a detector will detect a binary chirping if the frequency evolves by a bin or more during the observing time, or $\dot{f} \gtrsim \Delta f/T_{obs}$. For the known parameters of AM CVn, Equation 5.8 predicts an evolution of $\dot{f} = 4.79 \times 10^{-19}$ Hz/s. For a $T_{obs} = 1$ year observation, the limiting chirp would be $\dot{f} = 1$ bin/yr $= 1.00 \times 10^{-15}$ Hz/s; AM CVn's chirp falls well below this conservative threshold. For the purposes of this work, it is assumed the binaries are all monochromatic (nonchirping).

A spaceborne interferometer will characterize both polarization amplitudes as part of its deconstruction of the data stream; the ratio of h_+ to $h_\times$ is a direct measure of the inclination angle, ι, of the binary, as shown in Figure 5.4. Knowledge of the inclination angle provides further constraints on the model of the electromagnetic lightcurve, making

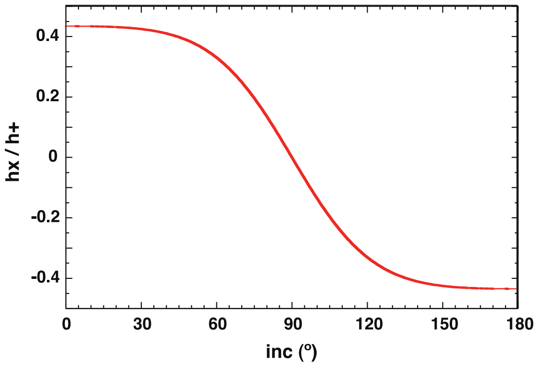

Figure 5.4: Measuring the ratio of measured gravitational wave polarization amplitudes, $h_\times/h_+$, is a measure of the binary inclination angle, ι.

any derived radius of the accretion disc more secure.

5.2.4 Multi-Messenger Phase Comparison

The multi-messenger comparison being examined in this project is exploiting the periodic structure in both the gravitational wave and the electromagnetic signals as a probe of the geometry of the source. Consider a circularized ultra-compact binary with orbital frequency, f_o. The gravitational wave frequency, f, is twice the orbital frequency of the binary, $f = 2f_o$. In this case, the gravitational wave signals peak at the times when the distance between the components of the binary when projected onto the sky plane is minimized, which occurs when one of the components is at its closest distance to the observer. This provides a fundamental marker for the orientation of the binary components in time. By contrast, the electromagnetic lightcurve shows variation (on orbital timescales) corresponding to the underlying components of the binary changing position and orientation with respect to the line of sight. The tool for determining the location of those structures, by measuring them against the reference provided by the gravitational waves, is the measured phase difference between the arriving gravitational waves and the electromagnetic lightcurve.

The phase difference between the lightcurve and the gravitational waves at any observation time t is

$$\Phi(t) = \phi_{gw}(t) - \phi_{em}(t) = 2\pi t(f_{gw} - f_{em}) + \alpha \ , \tag{5.9}$$

where α is a phase offset between the gravitational waves as compared to the electromagnetic lightcurve at the time of measurement. The term α can encode a variety of physical and geometric effects, but in principle can be divided into two basic flavors: effects that delay propagation after the signals are emitted, and model-dependent delays that produce phase offsets when the signals are originally generated in the system.

For propagation delays, there are two fundamental origins. First, gravitational waves and photons could propagate at intrinsically different speeds. General relativity predicts that gravitational waves should propagate at $v_{gw} = v_{em} = c$, but as a matter of observational science this can be tested using multi-messenger observations like those described here (Hazboun & Larson 2013). As the expectations are for general relativity's predictions to be correct, this chapter assumes gravitational waves will propagate at the speed of light: $v_{gw} = c$. A second fundamental delay during propagation could be experienced by the photons, traveling through media with nonunit index of refraction: first through the interstellar medium, and then through the Earth's atmosphere. Given the typical distance to sources that will be simultaneously detectable in both EM and GW spectra, the typical phase delay from propagation delays is estimated to be $\alpha_{prop} \sim 5 \times 10^{-11}$, about four orders of magnitude less than the expected accuracy of the raw phase measurements themselves (Larson & Hiscock 2000), and can be safely neglected for this analysis.

For geometric and model-dependent phase differences, one must consider the structure of the waves being observed. The gravitational wave structure is simple. The ultra-compact binaries being considered here are assumed to be circular and monochromatic, with the waveforms being accurately described by the quadrupole radiation formula. In this context, the gravitational waves are sinusoidal. Even for systems that harbor small amounts of eccentricity, the signals will still be exceedingly clean (both cases are shown in Figure 5.5). The peaks in the gravitational wave signals correspond to times when the binary components reach their closest distance to the observer; thus, the gravitational waves provide an absolute reference for locating the binary axis orientation as a function of time. There is an ambiguity associated with the quadrupolar nature of the gravitational radiation pattern — it peaks when one component is at its closest distance to the observer, but also 180° away in the orbit,

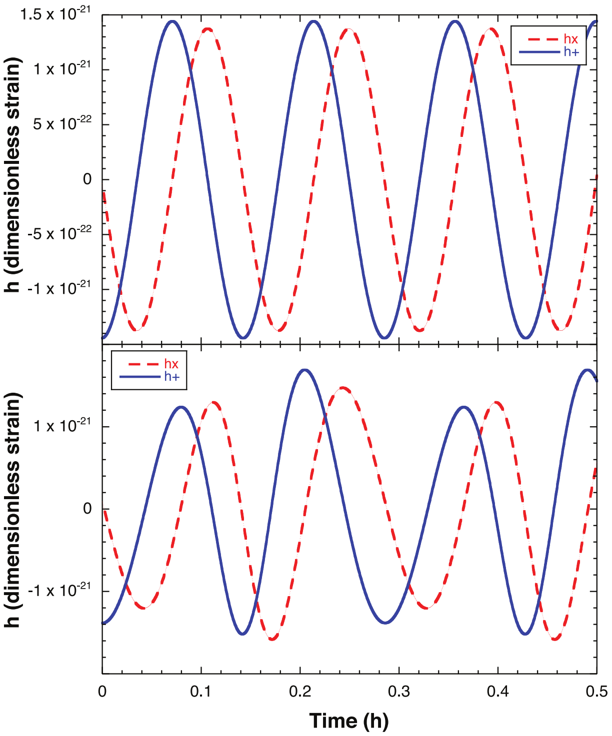

Figure 5.5: Simulated gravitational wave signals for AM CVn using current, best known parameters (Nelemans 2010). Top panel shows the signal for a purely circular, monochromatic system. Lower panel illustrates how signal changes if system had moderate eccentricity ($e = 0.1$), but otherwise identical parameters.

when the positions of the binary components are reversed (this is most obviously indicated in the gravitational wave frequency, which is twice the orbital frequency, $\omega_g = 2\omega_{orb}$).

By contrast, the electromagnetic lightcurve is rich in structure, with shapes and peaks in the curve being the result of the changing aspect of the system's internal components during the course of an orbit. There are several primary contributions to the lightcurve shape: emission from the white dwarf primary; emission from the Roche expanded secondary giving ellipsoidal variations as the secondary shape rotates relative to the line of sight; emission from the accretion disc; and lastly, emission from the hot spot where the overflow stream impacts the accretion disc. Consequently one must choose where we want the gravitational wave signal and the lightcurve signal to line up, and the offset from this alignment point to the point of zero binary phase constitutes the geometrical part of α.

In this project we are interested in characterizing the accretion disc radius by measuring the phase of the hot spot compared to the phase of the gravitational wave signal. In this context then, the value of the parameter α in Equation 5.9 is affected by the geometric angle $\alpha_\star$ illustrated in Figure 5.6, the angle between the binary axis and the impact point on the accretion disc. For a given model of the overflow stream, the measured value of $\alpha_\star$ will correspond to a unique accretion disc radius. The ability to measure $\alpha_\star$ will be limited by the errors associated with each of the independent phase measurements, and by our ability to recognize the contribution of the hot spot to the electromagnetic lightcurve.

5.3 A Simple Model for Ultra-Compact Mass Overflow Binaries

5.3.1 Model System: AM CVn

Many ultra-compact binaries have already been identified as candidate verification binaries for space-based gravitational wave detectors (Nelemans 2010). For the purposes of demonstration, the current known values for *AM Canum Venaticorum* (AM CVn) are used as canonical parameters. AM CVn is the archetype for a large number of ultra-compact binaries that are expected to be visible in gravitational waves. The physical parameters for AM CVn are (see Table 4): $m_1 = 0.68M_\odot$, $m_2 = 0.125M_\odot$, and $\omega = 6.108 \times 10^{-3}$ s^{-1} (a circular binary with semimajor axis $0.21R_\odot$). The disc radius is estimated to be $R_d = 0.478a$ (Solheim et al. 1998). The temperature parameters were estimated by minimizing the L_2 error between the output of our lightcurve model (see Section 5.3.3) and the observed lightcurve. A temperature $T = 10^4 K$ is adopted as an initial guess for the pole temperature

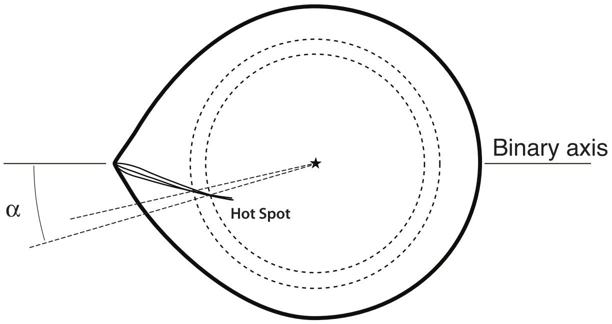

Figure 5.6: The overflow stream from the donor creates a hot spot at the impact point on the accretion disc. The value of the angle $\alpha_\star$ depends on the radius of the accretion disc.

Table 4
AM CVn Simulation Parameters

Parameter	Notation	Value	Reference
Mass 1	m_1	$0.68M_\odot$	1
Mass 2	m_2	$0.125M_\odot$	1
Orbital Period	P_{orb}	1028.73 s	2
Inclination	ι	43°	1
Luminosity Distance	d	606 pc	1
Disc Radius	$R_{\rm disc}$	$0.48a$	3
Char. Disc Temp.	$T_{\rm disc}$	90000 K	Fit
Pole Temp.	$T_{\rm pole}$	15065 K	Fit, 4
WD Temp.	T_{WD}	19473 K	Fit
Max HS Temp.	$T_{\rm HS}$	131000 K	Fit
HS Cooling Parameter	ζ	2.9828	Fit

Notes. Parameters below the horizontal line are fitted using our lightcurve model.
References. (1) Roelofs et al. 2006; (2) Harvey et al. 1998;
(3) Solheim et al. 1998; (4) Roelofs et al. 2006.

of the secondary (Roelofs et al. 2006).

5.3.2 Overflow Simulations

Equations of Motion

In order to demonstrate this method for measuring the accretion disc radius, a simple model of the accretion overflow was created using the restricted three-body approximation (Flannery 1975). In the corotating frame of the binary, the accelerations on a fluid particle in the x and y directions may be written as

$$\ddot{x} = -\frac{Gm_1}{r_1^3}\left(x - \frac{aq}{1+q}\right) - \frac{Gm_2}{r_2^3}\left(x + \frac{a}{1+q}\right) + \omega^2 x + 2\omega\dot{y} - \xi\dot{x}, \text{ and} \tag{5.10}$$

$$\ddot{y} = -\frac{Gm_1}{r_1^3}y - \frac{Gm_2}{r_2^3}y + \omega^2 y - 2\omega\dot{x} - \xi\dot{y}\ . \tag{5.11}$$

Here $\omega = 2\pi f_{orb}$ is the orbital angular velocity of the stellar components, $q = m_2/m_1$ is the mass ratio, and ξ is a parameter that characterizes the viscous drag on the fluid element.

In simulation, the equation is nondimensionalized by introducing scaling factors M

(total mass) for mass, a (binary separation) for length, ω^{-1} for time, and GM/a for potential. The dimensionless equations then read

$$\tilde{x}'' = -\frac{\mu}{\tilde{r}_1^3}(\tilde{x} - \tilde{a}Q) - \frac{(1-\mu)}{\tilde{r}_2^3}\left(\tilde{x} + \frac{\tilde{a}}{q}Q\right) + \tilde{x} + 2\tilde{y}' - \tilde{\xi}\tilde{x}', \text{ and}$$
$$\tilde{y}'' = -\frac{\mu}{\tilde{r}_1^3}\tilde{y} - \frac{(1-\mu)}{\tilde{r}_2^3}\tilde{y} + \tilde{y} - 2\tilde{x}' - \tilde{\xi}\tilde{y}' \;, \tag{5.12}$$

where $\tilde{x}$ and $\tilde{y}$ are dimensionless coordinates, $\tilde{\xi}$ is the dimensionless viscosity coefficient, μ is the mass fraction $\mu = m_1/M$, $Q = q/(1+q)$, and prime denotes differentiation with respect to the dimensionless time variable.

These equations are simultaneously numerically integrated to give the position and velocity of particles in the overflowing accretion stream. The geometric information regarding the position of the stream is an essential player in the determination of the accretion disc radius, and the stream particle velocity at disc impact is used in the energetic calculations that give the model brightness for the hot spot.

From this point on, tildes will be dropped and quantities discussed in the context of the overflow simulation will be the dimensionless variables.

Stream Coherence

Early numerical simulations (Flannery 1975) of matter overflow in cataclysmic variables suggested the stream maintains coherence as it falls toward impact. Coherence in the overflow stream through impact with the primary accretion disc is a necessity to understanding the variable lightcurve created by cataclysmic variable stars such as AM CVn. To evaluate the stream coherence in this model, initial velocity data for Equation 5.12 were drawn from the Maxwell-Boltzmann Speed Distribution, which describes the speed distribution of particles in a simple gas:

$$f(\upsilon) = \frac{\sqrt{\frac{2}{\pi}}\upsilon^2 \exp(\frac{-\upsilon^2}{2\eta^2})}{\eta^3}, \tag{5.13}$$

where η is determined by the thermal coefficient

$$\eta = \sqrt{\frac{kT}{m}}, \tag{5.14}$$

and k, T, and m are Boltzmann's constant, the temperature of the secondary, and the mass of the particle in the stream. The velocities were constrained by angle $\theta = \pm 57^\circ$, the maximum opening angle of the gravitational equipotential that passes through the inner Lagrange point.

Taking the canonical particle mass to be the mass of a proton, the simulation was run $2,500$ times pulling randomly from the speed distribution and attaching that speed to an angle drawn from a uniform distribution in the range of θ. Results of this simulation are shown in Figure 5.7, in the corotating frame of the binary. This histogram shows the injected parameters, while the trajectory plot shows overlays of all $2,500$ runs in the equipotential space dominated by the white dwarf (the vertex of the equipotential boundary drawn at $y = 0$ is the Lagrange point between the primary and secondary). All of the trajectories, irrespective of initial conditions at the overflow point, coalesce around a central trajectory.

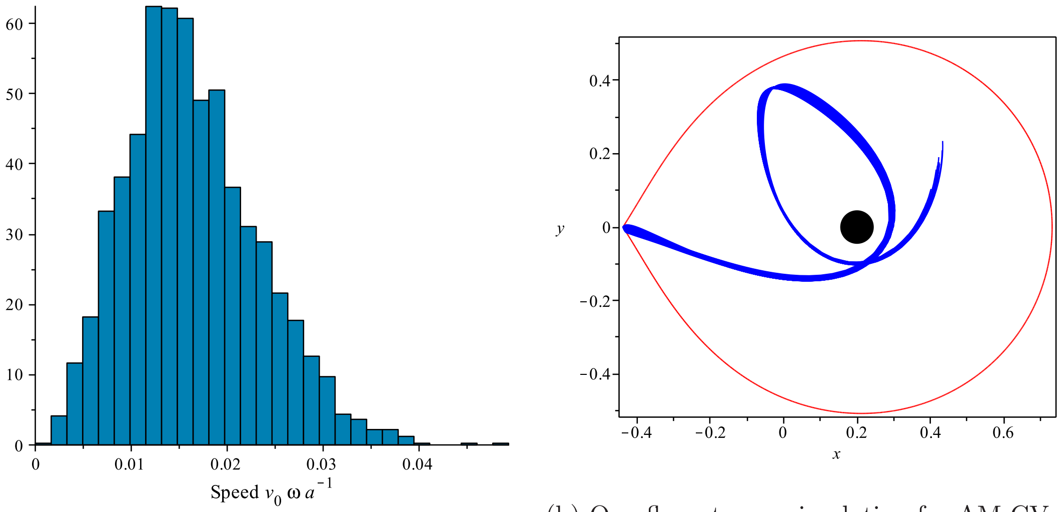

(a) Histogram of sampled speeds with most probable speed $v_p = \sqrt{2}\eta = 0.0145$.

(b) Overflow stream simulation for AM CVn parameters. Stream is visually observed to maintain coherency until self impact.

Figure 5.7: Overflow stream simulation figures.

Hot Spot Phase Angle

Based on the stream coherence simulation, the trajectory of the matter overflow stream is known until the time it intersects the accretion disc. The HS phase offset angle, $\alpha_\star$, is measured from the binary axis (located from the gravitational waves) to the hot spot impact point (measured from the electromagnetic lightcurve), and using the trajectory model yields the accretion disc radius at which the trajectory crosses the angle $\alpha_\star$ (i.e., the radius of the disc when it intersects the matter stream). For the AM CVn demonstration parameters, Figure 5.8 displays calculated values of the HS phase offset angle, $\alpha_\star$, for a range of disc radii lying within the primary's Roche radius. Larger disc radii show a small spread in impact angles ($\sim 2^\circ$), a consequence of tight stream coherency, while smaller radii result in a larger impact spread (as high as $\sim 10^\circ$) due to the oblique angle of attack at impact.

Viscosity Term

The overflow stream consists of a collection of infalling particles, which will have some measure of interaction with each other, plausibly influencing the trajectory. To explore this, a dimensionless viscosity parameter is used in the Equations of motion, Equation 5.12. In general, this value is expected to be small, $\xi \lesssim 0.1$, but even smaller values are typical in modern accretion simulations (Kley et al. 2008), to the point of using inviscid flow (Sawada & Matsuda 1992). By examining the range of ξ over which the stream crosses itself, it is seen that neither the mean impact angle nor the angular spread vary significantly in the range $0 \leq \xi \leq 0.3$ (see Figure 5.9). For viscosity values larger than $\xi \gtrsim 0.3$, these simulations enter the regime where the stream will not cross itself, but rather it will impact the primary directly, resulting in no disc formation. This implies that the stream viscosity does not significantly affect the angle $\alpha_\star$. A value of $\xi = 0.06$ is adopted for the simulations presented here.

5.3.3 Lightcurve Simulations

Since simultaneous, coordinated electromagnetic and gravitational wave observations of ultra-compact binaries do not exist (yet), simulated lightcurve data are generated for this

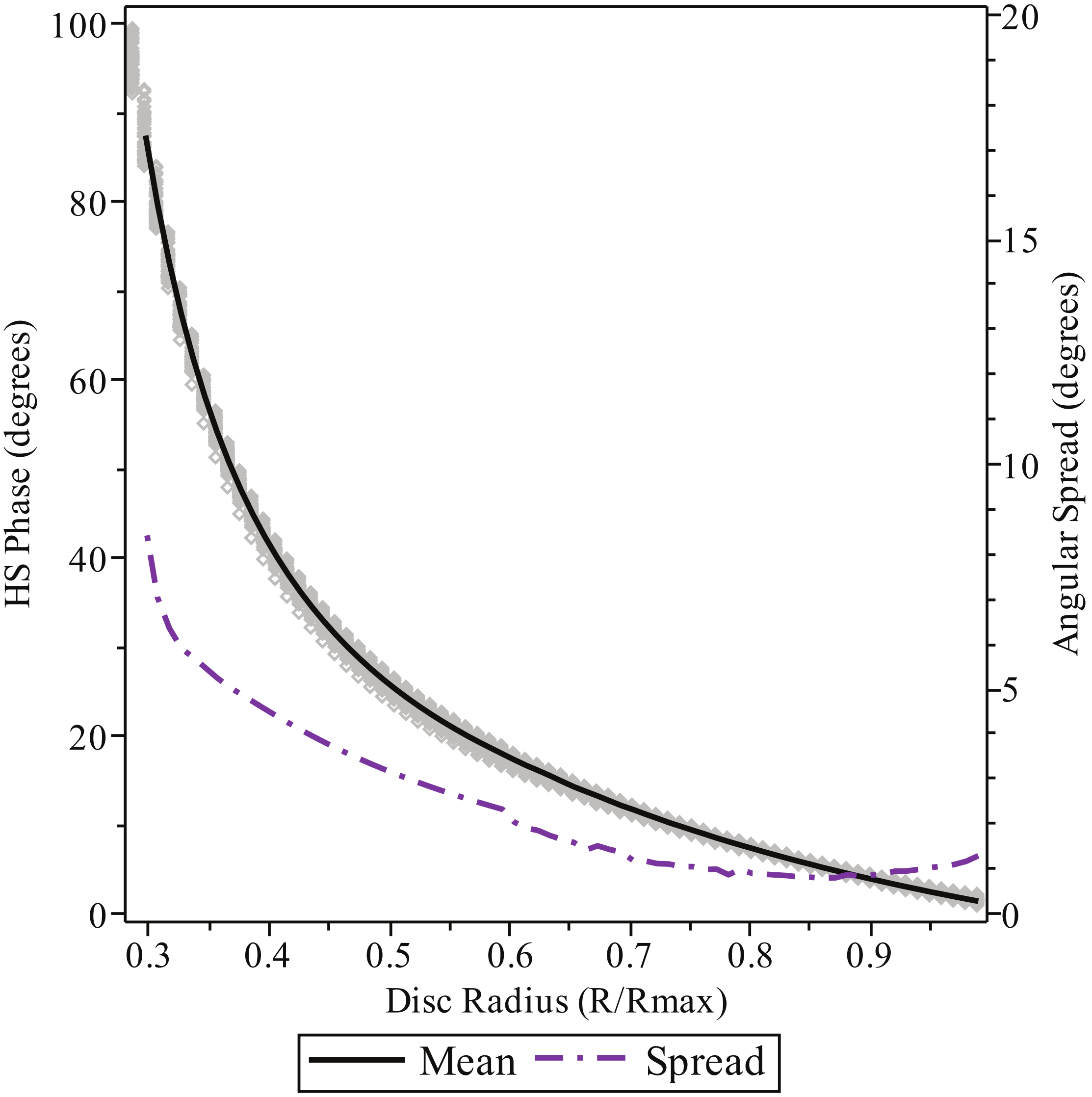

Figure 5.8: Stream impact angle $\alpha_\star$ for various disc radii, ranging up to the size of the primary Roche lobe. Radius values are scaled by the value $R_{\max}$, which is defined as the distance from the primary to the $L1$ Lagrange point. The grey envelope shows the spread of impact angles for a random selection of initial velocities, while the black line plots the mean of the spread. The dashed line plots the angular spread of the stream impact with values on the right vertical axis.

study. Lightcurves are generated via a simple geometric model with numerically modeled accretion implemented in a MATLAB program. In this simulation, a close binary system with an accretion disc and a hot spot is rotated in three dimensions, and the observed portions of the bodies in the system are used to generate a synthetic lightcurve. This is

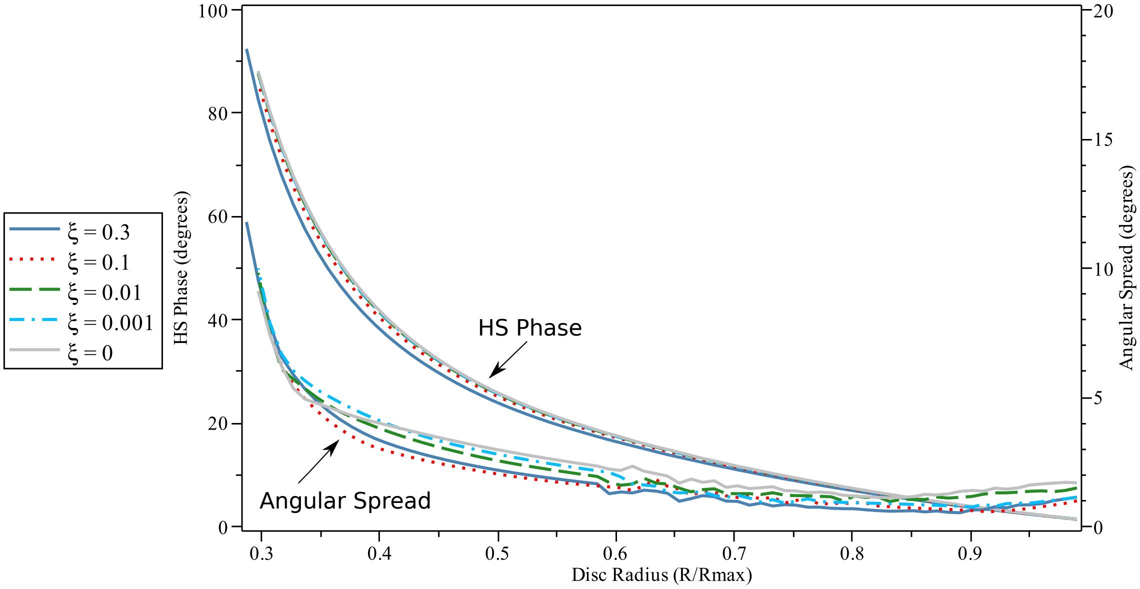

Figure 5.9: HS phase offset angle, $\alpha_\star$, for various values of dimensionless viscosity, ξ. Note that the mean impact angle and angular spread are essentially unchanged over many orders of magnitude.

a geometry-based simulation; physical processes such as gravitational attraction are not explicitly computed. This is a well-known basis for lightcurve simulations, e.g., Wilson & Devinney (1971).

Setup

There are four distinct objects in the simulation: the primary star, the accretion disc, the hot spot, and the Roche lobe filled by the secondary star. Three-dimensional point clouds (collections of points in 3-D) are generated for each object in appropriate orbital positions, which are then used to compute the three-dimensional convex hull of each object. The convex hull of a 3-D point cloud is a triangulation of the bounding surface of the cloud, i.e., a set of vertex-connected triangles such that all points in the cloud are either triangle vertices or interior to the surface formed by the triangulation. For each triangle in the triangulation, the geometric center, area, and normal vector are computed. Temperature profiles (described in the next section) are mapped onto the objects by assigning a temperature for each triangle in the convex hulls, based on input parameters for the simulation.

The simulation can be run for as long as desired to generate lightcurves of arbitrary length.

Temperature Profiles

Temperature values for the Roche lobe are generated by the law of gravity darkening, $T_e \propto g^{1/4}$ (Lucy 1967; von Zeipel 1924). This leads directly to an expression for the temperature at any point on the Roche lobe given the pole temperature, T_{pole},

$$\frac{T(x,y,z)}{T_{\rm pole}} = \left[\frac{g(x,y,z)}{g_{\rm pole}}\right]^{1/4}, \tag{5.15}$$

where $T_{\rm pole}$ and $g_{\rm pole}$ are the values of temperature and gravitational acceleration at the star pole. $T_{\rm pole}$ is generally taken to be the effective temperature of a comparable field star (Orosz & Bailyn 1997), and $g_{\rm pole}$ can be found by taking the gradient of the known gravitational potential at the pole of the Roche lobe.

The temperature profile for the disc is a simple energy-conservation-based model given by

$$T = T_{\rm disc}\left(\frac{R}{r}\right)^{3/4}\left(1-\sqrt{R/r}\right)^{1/4}, \tag{5.16}$$

where

$$T_{\rm disc} = \left(\frac{3Gm_1\dot{m}_1}{8\pi\sigma R^3}\right)^{1/4} \tag{5.17}$$

is a characteristic temperature of the disc with $\dot{m}_1$ the mass transfer rate, R the radius of the primary, r the radial distance out from the center of the disc, and σ the Stephan-Boltzmann constant.

The hot spot is modeled as a sphere with center located at the edge of the accretion disc, and assigned an exponentially decaying temperature profile according to

$$T(\hat{x}) = (T_{\rm HS} - T_d)\exp(-\zeta\hat{x}) + T_d, \tag{5.18}$$

where $\hat{x}$ is a dimensionless coordinate that ranges from $0 \le \hat{x} \le 2$, given by $\hat{x} = (s - s_{\rm CM})/R_{\rm HS} + 1$, s is the radial distance of the center of the hot spot from the primary, $s_{\rm CM}$ is the center of the hot spot, $R_{\rm HS}$ is the radius of the hot spot, $T_{\rm HS}$ is the maximum temperature on the hot spot, T_d is the outer disc temperature, and ζ is the spatial cooling rate.

The primary white dwarf temperature is set as a constant value over a sphere.

Geometric Flux Projection

The lightcurve simulation assumes the observer is positioned far away on the negative z-axis, in which case the xy-plane is the sky plane for the observer. At each time step, a point on the synthetic light curve is computed as follows. For the four objects in the simulation, the normal vectors for each triangle in the convex hull triangulations are examined to determine if the value of the z component is negative, i.e., has a component pointing toward the observer. Triangles failing this condition are discarded for this iteration. Next, the objects are ordered based on their z coordinate, essentially from lowest to highest. The triangle centers of the first object in the order are projected onto the xy-plane. Subsequent objects are also projected; however, care is taken to avoid overlap of the objects by use of a 2-D convex hull and a standard point-in-polygon algorithm. The 3-D convex hull and 2-D projection are shown for the Roche lobe in Figure 5.10a. Triangles whose projected centers lie interior to the convex hull of a previously projected object are discarded, thus ignoring those triangles occulted by other objects in the system.

The luminosity of each triangle visible to to the observer is calculated using the Stefan-Boltzmann law. Total flux arriving at Earth is then computed using the standard flux-luminosity relationship, summed over $\mathcal{V}(t_k)$, the set of all visible triangles at the kth time step,

$$F(t_k) = \sum_{i \in \mathcal{V}(t_k)} \frac{\sigma A_i T_i^4 (\hat{\mathbf{o}} \cdot \hat{\mathbf{n}}_i)}{4\pi D_E^2}, \tag{5.19}$$

where A_i and T_i are the area and temperature of the ith triangle, respectively, $\hat{\mathbf{o}}$ is the unit vector pointing toward the observer, $\hat{\mathbf{n}}_i$ is the unit vector normal to the ith triangle (see Figure 5.10b), and D_E is the distance to Earth.

This simulation calculates only raw bolometric blackbody luminosities; more detailed effects such as frequency specific flux, reflectance, etc. are not included. We are using the

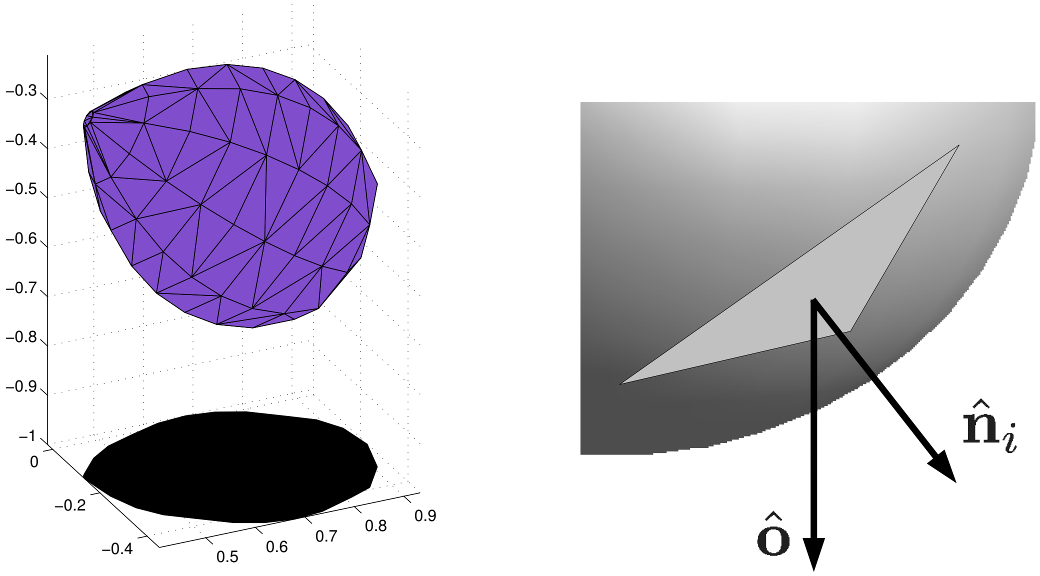

(a) Example of the 3-D convex hull for the Roche lobe as used in the lightcurve simulation. Also shown is the 2-D projection onto the x-y plane.

(b) Illustration of observer vector and triangle normal vector, overlaid on a convex hull element at the stellar surface.

Figure 5.10: Lightcurve simulation figures.

full simulation only as a test for the radius estimation method, not for detailed parameter estimation, so we find these omissions acceptable. A lightcurve generated for the AM CVn model parameters is plotted against observed lightcurve data in Figure 5.11.

5.3.4 GW Phase Calibration

The $h_+(t)$ and $h_\times(t)$ waveforms in Equation 5.4 represent the expected signals that will be observable by a gravitational wave observatory. These expressions can be solved for θ to give an estimate of the binary phase as a function of time:

$$\hat{\theta}(t) = \frac{1}{2}\cos^{-1}\left(\frac{2\sqrt{\tilde{h}_+^2(t)+\tilde{h}_\times^2(t)-\cos^2(\iota)}}{\sin^2(\iota)}\right), \tag{5.20}$$

where $\tilde{h}_+$ and $\tilde{h}_\times$ are the measured waveform amplitudes scaled by H, i.e., $h_+ = H\tilde{h}_+$.

There is a four-fold degeneracy in Equation 5.20 due to the square root and inverse

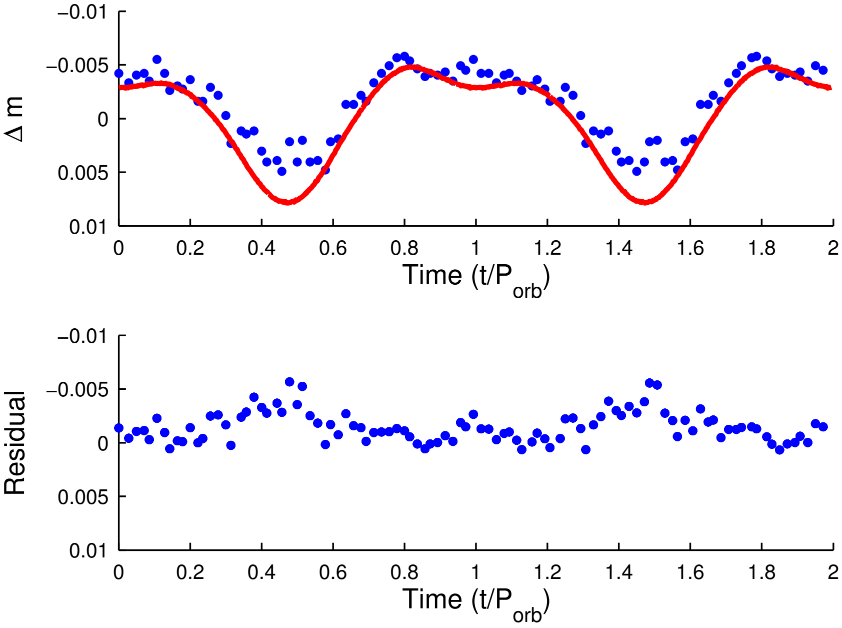

Figure 5.11: Simulated lightcurve for AM Canum Venaticorum in the top panel, displayed as magnitude deviation from mean, Δm. Solid line shows simulation output, dots represent actual AM CVn data [extracted from Harvey et al. (1998)]. Bottom panel shows residuals between model and observation.

cosine. This results in four locations where $\hat{\theta} = 0$ during each binary orbit, corresponding to the phases where the projected distances between the binary components are maximized or minimized, i.e., the quadrature and conjunction phases. The model lightcurve uses a value of $\phi = 25°$, resulting in gravitational wave signals and phase estimate as shown in Figure 5.12.

5.4 Model Demonstration and Implementation

Our accretion disc radius estimation method is now described explicitly and applied to the AM CVn system. Lightcurve data from our model and the actual observed lightcurve from Harvey et al. (1998) are used to demonstrate the method. Gravitational waveforms and model lightcurves are generated using the model parameters in Section 5.3.1. Since gravitational wave observations do not yet exist for this system, we regard this as a test of the method with partially real data.

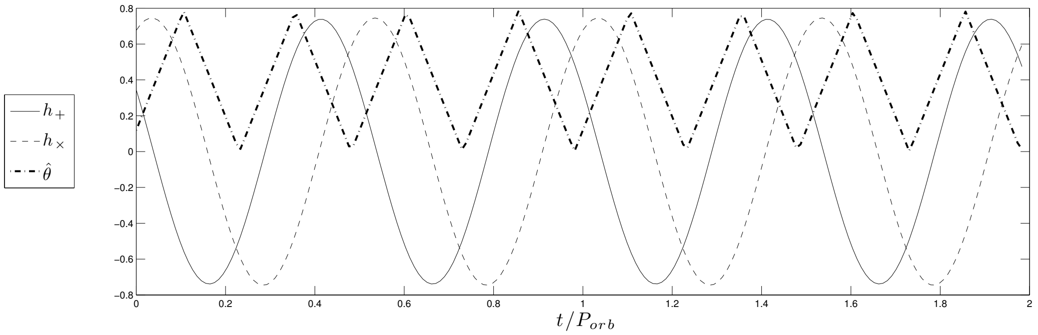

Figure 5.12: Gravitational wave signals, $\tilde{h}_+$ and $\tilde{h}_\times$, as well as the estimated phase value $\hat{\theta}$. Note there are four possible zero values of phase in each orbital period.

We assume that fundamental parameters of the system can be extracted, i.e. component masses, secondary temperature, orbital period, inclination, and luminosity distance, from which a stream overflow model and lightcurve model for the ellipsoidal variations (EV) can be generated. We also assume the gravitational wave signals $h_+(t)$ and $h_\times(t)$ have been disentangled and are separately available. There will be a substantive number of multi-messenger binaries that can be simultaneously observed in EM and GW spectrums (Littenberg et al. 2013). The gravitational wave data will provide accurate values for the component masses, the orbital period, and the inclination, all of which will inform the modeling described here.

The method proceeds as follows:

- Model accretion stream.
- Model ellipsoidal variations.
- Use GW signal to calibrate lightcurve to orbital phase.
- Subtract EV from observational data – remaining modulation should be due to hot spot.
- Determine phase offset between binary axis and hot spot.
- Use stream overflow model to determine radius of disc.

5.4.1 System Modeling

The methods outlined in Section 5.3.3 have been used to model the AM CVn lightcurve, which is shown against the observed lightcurve in Figure 5.11. Using our model parameters, the calculated magnitude for this simulation is $m_{\mathrm{sim}} \approx 14.18$, which matches the accepted value for AM CVn.

The model output shown in Figure 5.11 displays the residuals between the observed data and the model fit in the bottom panel. The model performs reasonably well in recreating the qualitative features of the observed data given it's simplicity, though it greatly overestimates the amount of dimming that occurs during the quadrature phases. These errors are likely due to omitting physical effects, such as reflectance and limb darkening, which would have small but noticeable effects on the total flux output.

Our lightcurve model is used in two ways. First we assume the model lightcurve generated by simulating the full AM CVn system is the observed lightcurve and proceed with the method from there, showing that the method can recover the disc radius well for the simulated data. In parallel, we work with the true lightcurve data where the full system model is not used. For each case, a model of the EVs are required to perform the subtraction which results in the hot spot modulation, and so each demonstration utilizes the EV model generated by our simulation. Given the simple and predictable nature of EVs, this is a reasonable course of action.

5.4.2 EV Subtraction

In order to locate the hot spot phase, the contribution to the lightcurve from the EV must be modeled and removed. The resulting EV from our model using the AM CVn parameters from Table 4 is shown in Figure 5.13.

In Section 5.3.4 the method for identifying the quadrature and conjunction phases using the gravitational wave signals was described. To compute the hot spot phase offset from the binary axis, we need to identify the conjunction phase in which the secondary Roche lobe is closest to the observer, as the hot spot flux should peak briefly before that time. It is the phase difference between the hot spot flux peak and the following conjunction phase that

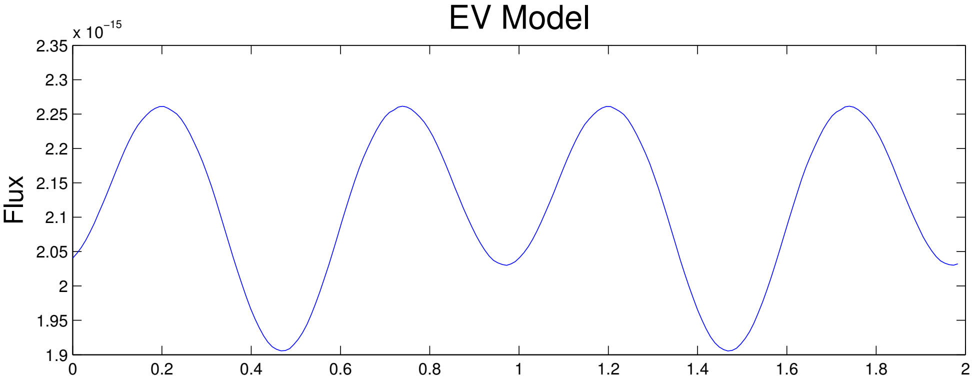

Figure 5.13: Ellipsoidal variation model output for Am CVn. This curve will be subtracted from observed lightcurve to find the HS modulation after the correct initial phase θ_0 is found.

we interpret as the hot spot phase offset. Using the synthetic GW signals, a binary phase estimate, $\hat{\theta}(\tilde{t})$, is generated and shown in Figure 5.12. The conjunction and quadrature phases are identified as the points where $\hat{\theta}(\tilde{t}) = 0$ ($\tilde{t} \equiv t/P_{orb}$), and since our EV model treats a quadrature phase for $\theta = 0$, the initial phase, θ_0, for the EV model will take one of four values

$$\theta_{0,i} = 2\pi(1 - 0.25i - \tilde{t}_0), \tag{5.21}$$

where $i \in \{0, 1, 2, 3\}$, and $\tilde{t}_0$ is the first location where $\theta(\tilde{t}) = 0$.

Based on the overflow trajectory simulations, we expect the phase of the HS peak output to lead the appropriate conjunction phase. We make the reasonable assumption that the peak in the lightcurve corresponds closely to the peak in received hot spot flux, and so we choose the valley in $\hat{\theta}$ just behind the lightcurve peak to be the appropriate conjunction phase, making the previous $\tilde{t} = 0$ point the quadrature phase we want for the initial EV phase, i.e., the point near $\tilde{t} = 0.75$ in our demonstration data.

With both the EV model and initial phase estimate in hand, the estimated hot spot modulation can be found by performing the subtraction $HS = OD - EV$ (abbreviations from Table 5). If the correct initial phase was chosen, the remaining variation in the lightcurve should be due to either HS modulation or eclipses. The subtraction results are shown in Figure 5.14 for both the full model simulation (solid red curve) and the actual observed data (blue dots). The top panel illustrates the result of choosing an incorrect $\tilde{t}_0$

Table 5
Lightcurve Abbreviations

Abbreviation	Meaning
OD	Observed lightcurve data
HS	Hot spot modulation
EV	Ellipsoidal variations

as the initial phase for the EV model, while the bottom panel shows the result of choosing the correct initial phase as described previously.

5.4.3 Disc Radius Estimate and Errors

The subtraction $HS = OD - EV$ yields what should be the modulation in the lightcurve due to the hot spot flux. From here it is possible to estimate the phase at which the hot spot flux peaks (the face-on view), and therefore compute a value for the HS phase angle $\alpha_\star$.

Noise exists in both the simulated data and the observed data. In the simulated data this arises from the fact that the simulation samples are taken at a realistic rate (60 Hz), and numerical noise that is introduced by the finite discretization of the body surfaces. Due to the noise present in the lightcurves, we estimate the location of maximum HS flux output by fitting parabolas to random subsets of the lightcurve data surrounding the apparent peak in the $HS = OD - EV$ subtraction and taking the mean of the resulting parabola vertex locations as the orbital phase of the HS peak flux output, θ_{HS}. The HS phase offset, ϕ_{HS}, is then estimated by finding the phase difference between θ_{HS} and the conjunction phase following the initial phase, i.e., $\phi_{HS} = (\theta_0 + \pi/2) - \theta_{HS}$, and the corresponding disc radius is identified from the accretion stream simulations described in Section 5.3.2. The parabola fitting procedure is depicted in Figure 5.15, which displays a small selection of the number of parabolas used.

For the model data using the random parabola procedure, we find a HS phase offset of $\phi_{HS} = 7.76^\circ \pm 1.6^\circ$. Using the overflow stream simulation, we find a corresponding disc radius estimate of $\hat{R}_D/a \approx 0.476 \pm 0.025$, where the error bars arise from various parabola fits. This gives an error for the mean value of $\approx 0.4\%$ when compared with the accepted

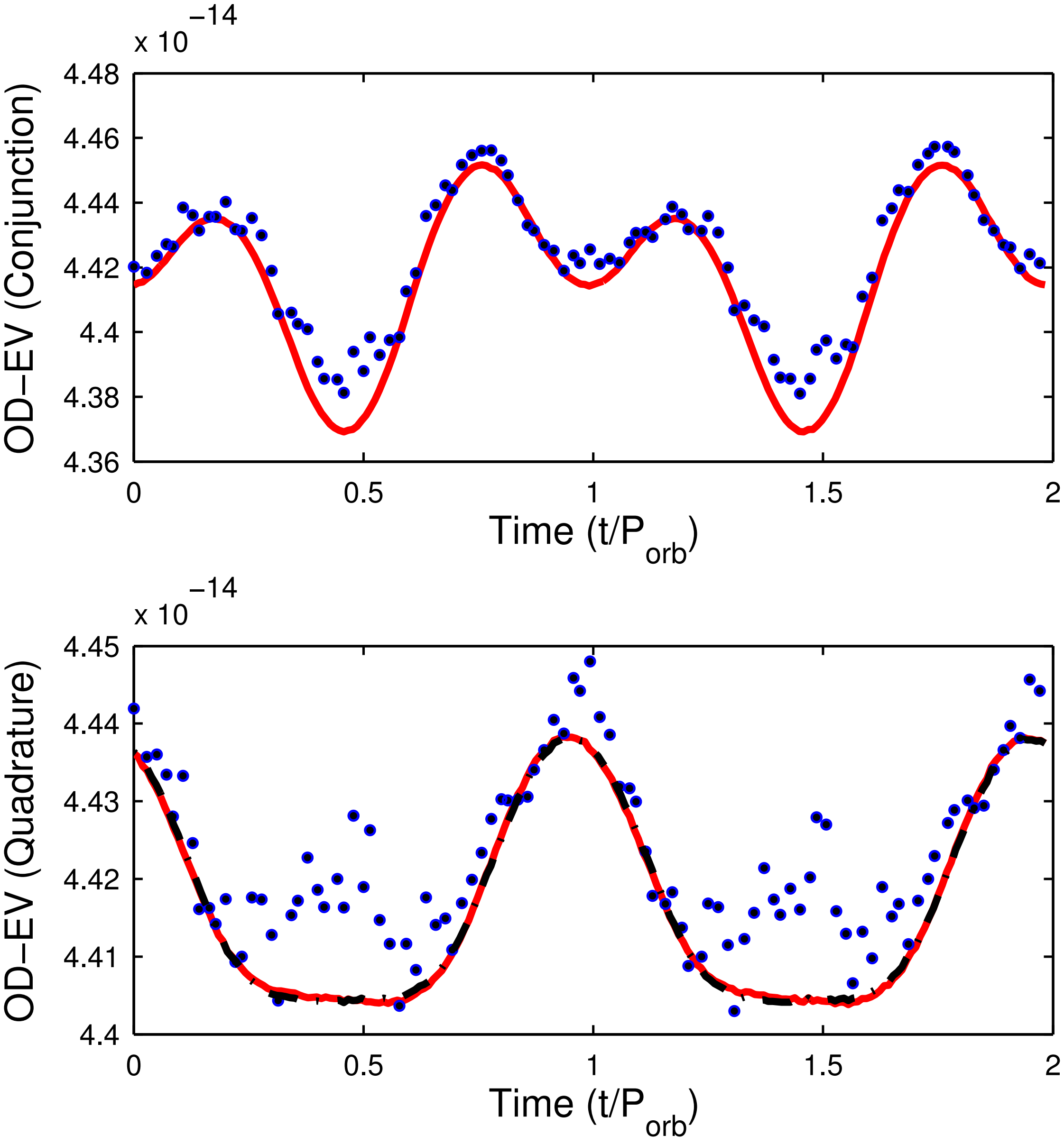

Figure 5.14: Results of the $HS = OD - EV$ subtraction for both the model data (red line) and observed data (blue dots) using the conjunction phase (incorrect) as θ_0 (top panel) and the quadrature phase (correct) as θ_0 (bottom panel). Also plotted in the bottom panel is the actual HS output from the model (black dot-dash). The model subtraction result matches very closely to the model HS output, but not perfectly due to errors discussed in the text.

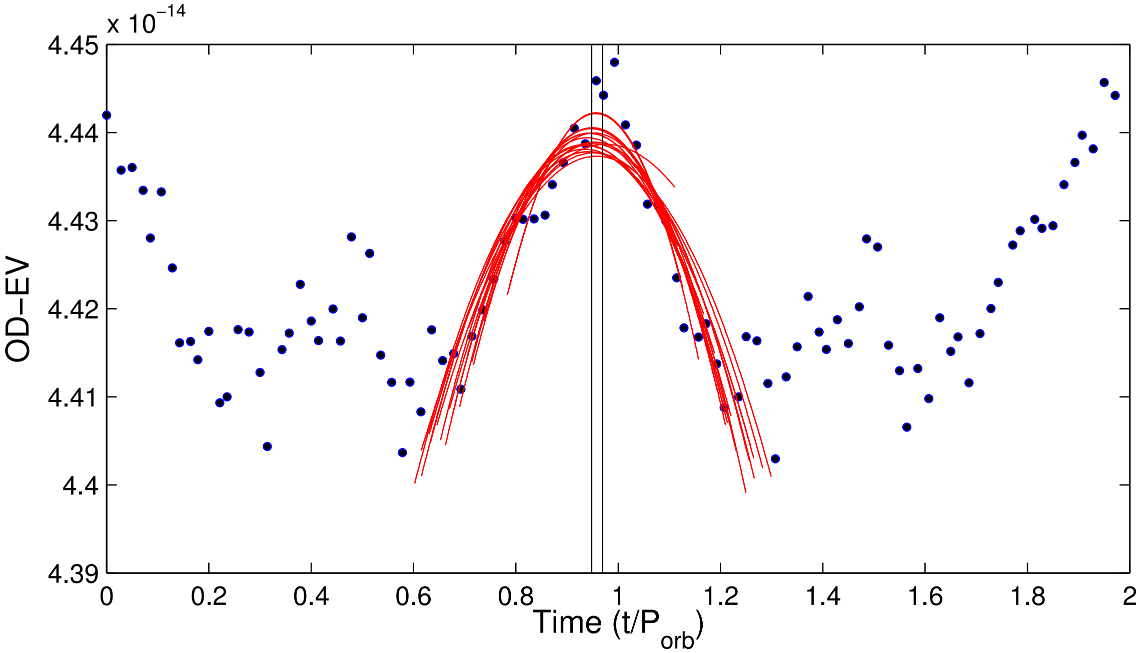

Figure 5.15: The parabola fitting procedure used to estimate the location of the observed HS peak output. Parabolas are fit to random subsets of the data surrounding the apparent peak near $t = 1$. The average peak location (left hand black line) is found and regarded as the true peak location, θ_{HS}, which is then used to find the HS phase offset, ϕ_{HS}, relative to the subsequent conjunction phase (right hand black line).

value of $0.478a$.

The noisy nature of the true observed data makes it less clear where the HS peak flux lies. We attempt the same fitting procedure and find HS phases in the approximate range $\phi_{HS} = 7.6^\circ \pm 2.8^\circ$. This translates to an estimated disc radius of $\hat{R}_D/a \approx 0.481 \pm 0.05$. With this method we find an estimation error of $\approx 0.6\%$.

5.5 Discussion

The method described here is an independent method that is applicable to mass-transferring galactic binaries observable by multi-messenger campaigns involving gravitational wave and electromagnetic observatories. It is a method for measuring the accretion disc radius in any compact binary system, whether it is eclipsing or not.

Recent work has estimated that with even modest, submeter class telescopes, there will be hundreds of ultra-compact binaries that will be simultaneously detectable in gravitational waves and with EM telescopes (Littenberg et al. 2013); thousands will be observable with multi-meter class telescopes, opening the potential to characterize the physical nature of an entire population of mass transferring binaries.

The model described here for measuring accretion disc radii assumes the primary variation in the optical lightcurve can be identified with a radiating hot spot on the disc, rotating about the primary with the orbital frequency, ω_o. In low-mass ratio systems like AM CVn, it has been predicted that the accretion disc will suffer tidal instabilities, deforming it into an eccentric precessing disc, resulting in the phase offset angle varying in time, $\alpha_\star = \alpha_\star(t)$. This instability was first recognized in SU UMa stars, and is thought to be responsible for the superhump phenomena in the optical signature of CV stars. The lightcurve of AM CVn is known to exhibit a superhump signature, which could complicate the measurement of the optical phase if it were not well characterized, especially when tracked over long time periods.

The superhump mechanism has been well studied, and there is a known relationship between the periods of the binary orbit (τ_o), the precessional period of the accretion disc (τ_{aa}, period of apsidal advance), and the superhump signature (τ_{sh}) given by

$$\tau_o^{-1} = \tau_{sh}^{-1} + \tau_{aa}^{-1} \ . \tag{5.22}$$

For AM CVn, all three periods have been measured [$\tau_o = 1028.77$ s, $\tau_{sh} = 1051.2$ s, and $\tau_{aa} = 13.38$ hr (Patterson et al. 1993; Harvey et al. 1998)]. This allows the lightcurve to be reduced and a measurement of the accretion disc made using the difference in phase with a gravitational wave signal. In principle, the presence of the superhump signature, together with the disc radius measurements described here, could be used in concert with gravitational wave observations to measure the ellipticity of the accretion disc. This in turn can provide a method to probe theoretical models of the pressure profile of the accretion disc (Goodchild & Ogilvie 2006). This will be the focus of a future study.

The analysis presented here also depends crucially on knowledge of the trajectory of the matter stream which overflows from the secondary Roche lobe into the sphere of influence of the white dwarf. If the hydrodynamic simulations of the overflow present an accurate picture of the trajectory, then gravitational wave observations can provide a new tool for probing the physical character of astrophysical systems.

CHAPTER 6

CONCLUSION

6.1 Summary and Future Directions

As the long-awaited GW detections come closer to reality, physicists are (and have been) working diligently to produce an extensive set of theoretical applications that will make use of the the observations. Techniques, models, and tools are being developed that will immediately put GW detections to work as new sources of astrophysical information. The deeper we can dig now, the more we will be able to learn once GW observations become a reality.

6.1.1 SMBH Encounters

The first project (Chapter 4) considered parabolic encounters between a binary system composed of two stellar-mass black holes and a galactic supermassive black hole. This setup was intended to mimic possible encounters in the center of galaxies similar to the Milky Way. Numerical codes were run that simulated this encounter, tracking relevant orbital quantities and reporting the end-state configuration. Approximately 13,000,000 of these simulations were run, giving confidence in the statistical conclusions drawn.

It was found that binaries disrupted by the SMBH form extreme mass ratio inspirals which would begin with very high eccentricity, $e \approx 1 - \mathcal{O}(10^{-2})$, but circularize dramatically by the emission of GW radiation. At the time when the stable orbit turns over to a plunge orbit, the EMRIs still have some small residual eccentricity, $e \approx 0.05$ on average. While this is much smaller than the typical residual eccentricity in the EMRIs formed by the capture of single stars, it is slightly larger than the previous estimate.

The surviving binaries were classified based on their final relation with the SMBH. A surviving binary could either remain unbound from the SMBH and hence have a merger lifetime $T < T_0$, or become bound to the SMBH in which case we compare the merger lifetime to the BEMRI (binary extreme mass ratio inspiral) period where long-period BEMRIs have $T < P_\bullet$ and short-period BEMRIs have $T > P_\bullet$. When inspecting the merger lifetime of the surviving binaries, it was found that the unbound binaries and the long-period BEMRIs have mean merger lifetime of $\tilde{T} = 0.8T_0$. When factoring in this new lifetime with other relevant data, we calculate the merger rate of these systems in the range of aLIGO to be about 0.25 yr^{-1}, which represents a small percentage of the current predicted CBC rates. Over long observing times, however, this effect could become noticeable.

Future possibilities for this project first include improving the integration scheme to make use of recent developments in post-Newtonian few-body simulation techniques. This would allow for more physically accurate results at very close encounters. Additionally, increasing the size of the parameter space to include neutron star masses or a spectrum of mass would extend the range of this study to more than stellar mass black holes, and using noncircular initial binaries, varied initial semimajor axis, and closer encounters with the SMBH would also form a more complete picture of these interactions.

6.1.2 Accretion Disc Radius

In the second project (Chapter 5), we studied the possibility of merging electromagnetic and gravitational wave observations to estimate the radius of the accretion disc in compact binary systems similar to AM CVn. The idea was built off of the well-accepted theory that the impact between the essentially freely flowing accretion stream and the inward spiralling accretion disc will result in a hot spot, which shines brightly with EM radiation. By identifying the angle of this hot spot on the accretion disc measured from the binary axis, ϕ_{HS}, the radius of the disc can be recovered.

Two simulations were built for this project. The first modeled the accretion stream as it flows from the inner Lagrange point and intersects with the accretion disc. This allows us to compute a disc radius for a given HS phase offset angle. The second simulation modeled the EM flux generated by a system like AM CVn, and was used as both a full simulation of the binary system as a test of our method, and to generate the lightcurve from the ellipsoidal variations, which must be removed in order to reveal the hot spot lightcurve modulations.

We tested the proposed method against the fully simulated lightcurve output from our model, as well as the true observed AM CVn lightcurve. In both cases, we found our method capable of estimating the disc radius to high precision by taking the average of the peak location of parabolas fit to random subsets of the data surrounding the apparent hot spot peak after EV subtraction. We calculated a disc radius of $\hat{R}_D/a \approx 0.476 \pm 0.025$ for the fully simulated data and $\hat{R}_D/a \approx 0.481 \pm 0.05$ for the true lightcurve data. These estimates agree with the accepted value of $R_D = 0.478a$ to within the uncertainties, and differ from the accepted value by 0.4% and 0.6%, respectively.

When GW observations from candidate systems are made, this method can truly be tested. Until then, this project could be advanced by including additional physics into the lightcurve simulation such as reflectance, limb darkening, and frequency-specific EM radiation. The method we have developed here could also be used to measure the ellipticity of noncircular, precessing discs. Such a measurement can provide a method to probe theoretical models of the disc pressure profile, and will be the focus of a future paper.

6.2 Final Thoughts

This dissertation has focused on work that centers around binary systems, which lie at the heart of the intersection between gravitational wave science and astrophysics. The projects presented here have addressed contrasting topics in both the astrophysics of compact binaries (three-body interactions and cataclysmic variable stars) and gravitational wave science (EMRIs, CBCs, and multi-messenger astronomy). I believe this illustrates the utility and importance of GW observations as new probes of astrophysical systems, and it is my sincere hope that this work has added constructively to the great scientific endeavor.

REFERENCES

Abadie, J., Abbott, B. P., Abbott, R., et al. 2010, Class. Quantum Grav., 27, 173001

Alexander, T. 2005, Phys. Rep., 419, 65

Amaro-Seoane, P., Aoudia, S., Babak, S., et al. 2013, GW Notes, 6, 4

Amaro-Seoane, P., Gair, J. R., Freitag, M., et al. 2007, Class. Quantum Grav., 24, R113

Antonini, F., Faber, J., Gualandris, A., & Merritt, D. 2010, ApJ, 713, 90

Antonini, F., Murray, N., & Mikkola, S. 2014, ApJ, 781, 45

Antonini, F. & Perets, H. B. 2012, ApJ, 757, 27

Arun, K. G. & Pai, A. 2013, International Journal of Modern Physics D, 22, 41012

Babak, S., Baker, J. G., Benacquista, M. J., et al. 2008, Class. Quantum Grav., 25, 184026

Babak, S., Baker, J. G., Benacquista, M. J., et al. 2010, Class. Quantum Grav., 27, 084009

Beichman, C. A., Woolf, N. J., & Lindensmith, C. A. 1999, The Terrestrial Planet Finder (TPF) : a NASA Origins Program to search for habitable planets (Pasadena: JPL publication)

Belczynski, K., Kalogera, V., Rasio, F. A., et al. 2008, ApJS, 174, 223

Benacquista, M. J. 2011, ApJ, 740, L54

Bender, P., Brillet, A., Ciufolini, I., et al. 1998, LISA Pre-Phase A Report, 2nd ed., MPQ 233

Bender, P. L. & Hils, D. 1997, Class. Quantum Grav., 14, 1439

Bennett, J., Donahue, M., Schneider, N., & Voit, M. 2013, The Cosmic Perspective (New Jersey: Pearson Education)

Bondi, H. 1957, Nature, 179, 1072

Brackenridge, J. 1996, The Key to Newton's Dynamics: The Kepler Problem and the Principia (Berkeley: University of California Press)

Bromley, B. C., Kenyon, S. J., Geller, M. J., et al. 2006, ApJ, 653, 1194

Brown, W. R., Geller, M. J., Kenyon, S. J., & Kurtz, M. J. 2005, ApJ, 622, L33

Brown, W. R., Kilic, M., Hermes, J. J., et al. 2011, ApJ, 737, L23

Burgay, M., D'Amico, N., Possenti, A., et al. 2003, Nature, 426, 531

Collins, H. 2010, Gravity's Shadow: The Search for Gravitational Waves (Chicago: University of Chicago Press)

Crowder, J. & Cornish, N. J. 2007, Phys. Rev. D, 75, 043008

Deloye, C. J. & Taam, R. E. 2006, ApJ, 649, L99

Demorest, P. B., Ferdman, R. D., Gonzalez, M. E., et al. 2013, ApJ, 762, 94

Dimopoulos, S., Graham, P. W., Hogan, J. M., Kasevich, M. A., & Rajendran, S. 2009, Physics Letters B, 678, 37

Downes, R. A., Webbink, R. F., Shara, M. M., et al. 2001, PASP, 113, 764

Dyson, F. W., Eddington, A. S., & Davidson, C. 1920, Royal Society of London Philosophical Transactions Series A, 220, 291

Eddington, A. S. 1922, Royal Society of London Proceedings Series A, 102, 268

Edelmann, H., Napiwotzki, R., Heber, U., Christlieb, N., & Reimers, D. 2005, ApJ, 634, L181

Einstein, A. 1916a, Sitzungsberichte der Königlich Preußischen Akademie der Wissenschaften (Berlin), Seite 688-696., 688

Einstein, A. 1916b, Annalen der Physik, 354, 769

Einstein, A. 1918, Sitzungsberichte der Königlich Preußischen Akademie der Wissenschaften (Berlin), Seite 154-167., 154

Einstein, A. & Rosen, N. 1937, Journal of The Franklin Institute, 223, 43

Faulkner, J., Flannery, B. P., & Warner, B. 1972, ApJ, 175, L79

Ferdman, R. D., van Haasteren, R., Bassa, C. G., et al. 2010, Class. Quantum Grav., 27, 084014

Flannery, B. P. 1975, MNRAS, 170, 325

Forward, R. L. 1978, Phys. Rev. D, 17, 379

Gair, J. R., Kennefick, D. J., & Larson, S. L. 2006, ApJ, 639, 999

Gair, J. R., Vallisneri, M., Larson, S. L., & Baker, J. G. 2013, Living Reviews in Relativity, 16

GEO600. 2006, GEO600 Sensitivity Curves http://www.geo600.uni-hannover.de/geocurves/

Ghez, A., Morris, M., Lu, J., et al. 2009, arXiv:astro-ph/0903.0383

Ghez, A. M., Salim, S., Hornstein, S. D., et al. 2005, ApJ, 620, 744

Ghez, A. M., Salim, S., Weinberg, N. N., et al. 2008, ApJ, 689, 1044

Goldstein, H., Poole, C., & Safko, J. 2002, Classical Mechanics (3rd ed.; San Francisco: Addison-Wesley Longman, Incorporated)

Goodchild, S. & Ogilvie, G. 2006, MNRAS, 368, 1123

Gualandris, A., Portegies Zwart, S., & Sipior, M. S. 2005, MNRAS, 363, 223

Hamilton, D. P. & Burns, J. A. 1991, Icarus, 92, 118

Hamilton, D. P. & Burns, J. A. 1992, Icarus, 96, 43

Harry, G. M. & the LIGO Scientific Collaboration. 2010, Class. Quantum Grav., 27, 084006

Harvey, D. A., Skillman, D. R., Kemp, J., et al. 1998, ApJ, 493, L105

Hawking, S. & Israel, W. 1989, Three Hundred Years of Gravitation, Philosophiae Naturalis, Principia Mathematica (Cambridge: Cambridge University Press)

Hazboun, J. S. & Larson, S. L. 2013, arXiv:gr-qc/1311.3153

Heggie, D. C. & Rasio, F. A. 1996, MNRAS, 282, 1064

Hellings, P. 1994, Astrophysics with a PC: An Introduction to Computational Astrophysics (Richmond: Willmann-Bell, Incorporated)

Hild, S., Chelkowski, S., & Freise, A. 2008, arXiv:gr-qc/0810.0604

Hills, J. G. 1988, Nature, 331, 687

Hils, D. & Bender, P. L. 1995, ApJ, 445, L7

Hils, D., Bender, P. L., & Webbink, R. F. 1990, ApJ, 360, 75

Hopman, C. & Alexander, T. 2005, ApJ, 629, 362

Hulse, R. A. & Taylor, J. H. 1975, ApJ, 195, L51

Hut, P. 1981, A&A, 99, 126

ICRR. 2010, KAGRA Sensitivity Curve http://gwcenter.icrr.u-tokyo.ac.jp/en/researcher/parameter

Ivanov, P. B. 2002, MNRAS, 336, 373

Jackson, J. D. 1998, in Classical Electrodynamics (3rd ed.; Hoboken: John Wiley & Sons, Incorporated), 243–246

Kalogera, V., Belczynski, K., Kim, C., O'Shaughnessy, R., & Willems, B. 2007, Phys. Rep., 442, 75

Kalogera, V., Narayan, R., Spergel, D. N., & Taylor, J. H. 2001, ApJ, 556, 340

Kennefick, D. 2007, Traveling at the Speed of Thought: Einstein and the Quest for Gravitational Waves (Princeton: Princeton University Press)

Kley, W., Papaloizou, J. C. B., & Ogilvie, G. I. 2008, A&A, 487, 671

Kramer, M. & Wex, N. 2009, Class. Quantum Grav., 26, 073001

Lada, C. J. 2006, ApJ, 640, L63

Larson, S. L. 2001, AJ, 121, 1722

Larson, S. L. 2003, LISA Online Sensitivity Curve Generator http://www.srl.caltech.edu/ shane/sensitivity/

Larson, S. L. & Hiscock, W. A. 2000, Phys. Rev. D, 61, 104008

Le Verrier, U. 1859, Comptes Rendus Hebdomadaires Des Sances De l'Acadmie Des Sciences, 49, 379

Lee, K. J., Wex, N., Kramer, M., et al. 2011, MNRAS, 414, 3251

Lindley, D. 2005, Phys. Rev. Focus, 16, 19

Littenberg, T. B., Larson, S. L., Nelemans, G., & Cornish, N. J. 2013, MNRAS, 429, 2361

Livas, J. et al. 2012, SGO Mid A LISA-Like Concept for the Space-based Gravitational-wave Observatory (SGO) at a Middle Price-Point http://pcos.gsfc.nasa.gov/studies/gravwave/gravitational-wave-mission-rfis.php

LSC. 2010a, Advanced LIGO Anticipated Sensitivity Curves https://dcc.ligo.org/LIGO-T0900288/public

LSC. 2010b, LIGO Laboratory Homepage for Interferometer Sensitivities http://www.ligo.caltech.edu/ jzweizig/distribution/LSC_Data/

Lubow, S. H. & Shu, F. H. 1975, ApJ, 198, 383

Lucy, L. B. 1967, ZAp, 65, 89

Maggiore, M. 2008, Gravitational Waves: Volume 1: Theory and Experiments, Gravitational Waves (Oxford: Oxford University Press)

Manchester, R. N., Hobbs, G., Bailes, M., et al. 2013, PASA, 30, 17

Merritt, D., Alexander, T., Mikkola, S., & Will, C. M. 2011, Phys. Rev. D, 84, 044024

Mikkola, S. & Aarseth, S. J. 1993, Celestial Mechanics and Dynamical Astronomy, 57, 439

Mikkola, S. & Tanikawa, K. 1999, MNRAS, 310, 745

Miller, M. C., Freitag, M., Hamilton, D. P., & Lauburg, V. M. 2005, ApJ, 631, L117

Misner, C., Thorne, K., & Wheeler, J. 1973, Gravitation, Gravitation No. pt. 3 (New York: W. H. Freeman)

Muno, M. P., Pfahl, E., Baganoff, F. K., et al. 2005, ApJ, 622, L113

Nelemans, G. 2010, LISA verification sources www.astro.ru.nl/ nelemans/dokuwiki/doku.php?id=lisa_wiki

Nelemans, G., Portegies Zwart, S. F., Verbunt, F., & Yungelson, L. R. 2001a, A&A, 368, 939

Nelemans, G., Yungelson, L. R., Portegies Zwart, S. F., & Verbunt, F. 2001b, A&A, 365, 491

O'Leary, R. M., Kocsis, B., & Loeb, A. 2009, MNRAS, 395, 2127

Orosz, J. A. & Bailyn, C. D. 1997, ApJ, 477, 876

Paczynski, B. 1977, ApJ, 216, 822

Patterson, J., Halpern, J., & Shambrook, A. 1993, ApJ, 419, 803

Patterson, J., Sterner, E., Halpern, J. P., & Raymond, J. C. 1992, ApJ, 384, 234

Peters, P. C. 1964, Physical Review, 136, 1224

Peters, P. C. & Mathews, J. 1963, Physical Review, 131, 435

Peterson, D. & Shao, M. 1997, in ESA Special Publication, Vol. 402, Hipparcos - Venice '97, ed. R. M. Bonnet et al., 749–754

Pitkin, M., Reid, S., Rowan, S., & Hough, J. 2011, Living Reviews in Relativity, 14

Pound, R. V. & Rebka, G. A. 1959, Phys. Rev. Lett., 3, 439

Preskill, J. & Thorne, K. S. 1995, in Feynman Lectures on Gravitation, ed. B. Hatfield (Boulder: Westview Press), vii–xxx

Prince, T. A., Binetruy, P., Centrella, J., et al. 2006, in Bulletin of the American Astronomical Society, Vol. 38, American Astronomical Society Meeting Abstracts, 990

Raghavan, D., McAlister, H. A., Henry, T. J., et al. 2010, ApJS, 190, 1

Ritter, H. 1980, A&A, 91, 161

Roelofs, G. H. A., Groot, P. J., Nelemans, G., Marsh, T. R., & Steeghs, D. 2006, MNRAS, 371, 1231

Rubanu, F., Poggiani, R., & Hough, J. 2009, Class. Quantum Grav., 26, 225012

Sathyaprakash, B. & Schutz, B. F. 2009, Living Reviews in Relativity, 12

Sawada, K. & Matsuda, T. 1992, MNRAS, 255, 17P

Schutz, B. 2009, A First Course in General Relativity (Cambridge: Cambridge University Press)

Scott, D. W. 1979, Biometrika, 66, 605

Sigurdsson, S. & Rees, M. J. 1997, MNRAS, 284, 318

Solheim, J.-E., Provencal, J. L., Bradley, P. A., et al. 1998, A&A, 332, 939

Stebbins, R., Baker, J., Benacquista, M., et al. 2012, SGO High: A LISA-Like Concept for the Space-based Gravitational-wave Observatory (SGO) at a High Price-Point http://pcos.gsfc.nasa.gov/studies/gravwave/gravitational-wave-mission-rfis.php

Sulkanen, M. E., Brasure, L. W., & Patterson, J. 1981a, ApJ, 244, 579

Sulkanen, M. E., Brasure, L. W., & Patterson, J. 1981b, ApJ, 244, 579

Taylor, J. H. & Weisberg, J. M. 1982, ApJ, 253, 908

Timpano, S. E., Rubbo, L. J., & Cornish, N. J. 2006, Phys. Rev. D, 73, 122001

Valtonen, M. & Mikkola, S. 1991, ARA&A, 29, 9

Virgo/INFN. 2011, Virgo Sensitivity Curves https://wwwcascina.virgo.infn.it/DataAnalysis/Calibration/Sensitivity/

von Zeipel, H. 1924, MNRAS, 84, 665

Wahlquist, H. 1987, General Relativity and Gravitation, 19, 1101, 10.1007/BF00759146

Wald, R. M. 1984, General Relativity (Chicago: University of Chicago Press)

Warner, B. 1995, Ap&SS, 225, 249

Weber, J. 1968, Physical Review Letters, 20, 1307

Weber, J. 1969, Physical Review Letters, 22, 1320

Weinberg, S. 1972, Gravitation and Cosmology: Principles and Applications of the General Theory of Relativity (Hoboken: John Wiley & Sons, Incorporated)

Weisberg, J. M., Nice, D. J., & Taylor, J. H. 2010, ApJ, 722, 1030

Will, C. M. 2006, Living Reviews in Relativity, 9

Willems, B., Vecchio, A., & Kalogera, V. 2008, Physical Review Letters, 100, 041102

Wilson, R. E. & Devinney, E. J. 1971, ApJ, 166, 605

Yardley, D. R. B., Hobbs, G. B., Jenet, F. A., et al. 2010, MNRAS, 407, 669

Yu, Q. & Tremaine, S. 2003, ApJ, 599, 1129

CURRICULUM VITAE

Eric D. Addison

CURRENT ADDRESS	1435 E 700 N Logan, UT 84321	*Cell:* (907) 350-4648 *E-mail:* eric.addison@aggiemail.usu.edu

RESEARCH INTERESTS

Gravitational wave astrophysics, technical computing applications (modeling and simulation, high performance computing, numerical methods), geophysics (inverse theory, seismic processing, seismic interpolation), information science (signal processing, stochastic processes, Bayesian statistics, detection and estimation theory).

ONLINE PRESENCE

LinkedIn: http://www.linkedin.com/pub/eric-addison/62/a68/79

SelectedWorks: http://works.bepress.com/eric_addison/

GitHub: https://github.com/ericaddison/

EDUCATION

Utah State University (USU), Logan, Utah

Ph.D., Physics, May 2014

- Dissertation: *Gravitational Wave Astrophysics with Binary Systems*
- Advisor: Dr. Shane Larson
- Area of Study: Gravitational Wave Astrophysics

M.Eng., Electrical Engineering, May 2013

- Advisor: Dr. Todd Moon
- Area of Study: Information Science and Signal Processing

University of Alaska, Anchorage (UAA), Anchorage, Alaska

B.S. Engineering, May 2008

- *Magna cum Laude*
- Advisor: Dr. Jens Munk
- Electrical and Computer Systems specializations

B.S. Mathematics, May 2008

- Advisor: Dr. Debbie Narang

RESEARCH SUMMARIES

Gravitational Wave Physics, USU, Spring 2009 - Present
Graduate Research Assistant, Advisor: Dr. Shane Larson
Developing multiple simulations for gravitational wave astrophysics including: supermassive black hole / compact object binary

interactions, binary system accretion disc observations, and stellar mass black hole population analysis.

Cooperative Vehicle Networks Lab, USU, Fall 2008
Research Assitant, Advisor: Dr. Wei Ren
Implemented control algorithms and real time data filtering techniques for autonomous quad-rotor stabilization. Assembled custom sensor suite for navigation and localization.

Investigating Unusual Permafrost, UAA, Aug 2007-May 2008
Research Assitant, Advisor: Dr. Jens Munk
Mapped probable location and extent of anomalous permafrost near Anchorage, Alaska using resistivity mapping. Accurate cross sectional plots were produced using inverse algorithms.

WRITING AND PUBLICATIONS

1. **Measuring accretion impact radii with optical and gravitational wave observations of compact binaries.** Eric Addison, Katelyn Brevik, Shane Larson. In preparation.
2. **Busting up binaries: parabolic encounters between compact binaries and a supermassive black hole** Eric Addison, Pablo Laguna, Shane Larson. In preparation.
3. **Astrophysical mechanisms for pulsar spindown.** Eric Addison. Doctoral candidacy exam report. http://works.bepress.com/eric_addison/

ACADEMIC APPOINTMENTS

Graduate Research Assistant Fall 2011 - present
Department of Physics,
Utah State University

Graduate Teaching Assistant Spring 2009 - Spring 2011
Department of Physics,
Utah State University

Graduate Teaching Assistant Fall 2009
Department of Electrical and Computer Engineering,
Utah State University

Undergraduate Lab Instructor Spring 2005
School of Engineering,
University of Alaska, Anchorage

TEACHING EXPERIENCE

Labs: General Physics for Life Sciences I & II, Physics for Scientists and Engineers I & II, Microcomputer Hardware Interfacing

Recitations: Physics for Scientists and Engineers I & II

Full Courses: General Physics for Life Sciences II, Physics for Scientists and Engineers II

TALKS AND PRESENTATIONS

April 2013, American Physical Society, National Meeting, Denver, CO.

June 2012, American Astronomical Society, National Meeting, Anchorage, AK.

March 2012, 2011, 2010, Intermountain Graduate Research Symposium, Logan, UT.

October 2010, American Physical Society, Four Corners Regional Meeting, Ogden, UT.

GRANTS AND SCHOLARSHIPS

Howard L. Blood Scholarship ($4000), 2012.

Gene Adams Endowed Scholarship ($500), 2010.

USU Meritorious Graduate Student Tuition Award ($1,795), 2009.

UAA Undergraduate Research Grant ($1,850), 2007.

UAA BP Mathematical Sciences Scholarship ($500), 2007.

Anchorage Society of American Military Engineers Scholarship ($1,000), 2007.

UAA Pia Denkewalter Memorial Scholarship ($750), 2006.

Sven and Lorraine Eriksson Scholarship ($2,850), 2006.

Armed Forces Communications and Electronics Association Scholarship ($2,000), 2006.

David D. Adams Memorial Engineering Scholarship ($1,000), 2005.

HONORS AND AWARDS

Intermountain Graduate Research Symposium, Outstanding Presentation Abstract Award, March 2012.

USU Department of Physics Outstanding TA Award, April 2011.
Awarded for excellence in teaching duties.

Intermountain Graduate Research Symposium, 1st Place, March 2011, March 2010.
Regional showcase of graduate research. First place physics presentation.

Sigma Pi Sigma Physics Honor Society, April 2010.
Inducted based on academic achievement.

National Science Foundation Graduate Research Fellowship Program, April 2010.
Honorable mention.

UAA Math Wrangler Award, Spring 2008.
Recognizes top academic performers in the mathematics program

UAA Engineering Student Competition, 1st Place, Fall 2007.
Undergraduate engineering design competition. Designed a RISC architecture and instruction set, simulated in MATLAB.

Who's Who Among Students in American Univ. and Colleges Award, Oct. 2007.

Martin Luther King Jr. Student Appreciation Citation, 2007
For making a postive difference as a student

UAA Chancellor's List, Spring 2008, Fall 2007, Spring 2007, Fall 2006, Spring 2006, Spring 2005, Fall 2002.
Recognizes students with a semester GPA of 4.0

UAA Dean's List, Fall 2005, Fall 2004.
Recognizes students with a semester GPA of 3.5 or better

Undergraduate Mentoring

Katelyn Brevik (BS, Physics, USU, graduated)

Darren McKinnon (BS, Physics, USU, current)

Russell Floyd (High School Student, InTech HS)

Workshops

Introduction to High Performance Computing, Sep. 21-22, 2013

Advanced School in General Relativity: Relativistic Astrophysics and Cosmology, July 16-27, 2012.
Competitive entrance, travel grant.

Center for Astronomy Education *Tier 1 Teaching Excellence Workshop*, June 9-10, 2012

South Padre Island International Summer School in Gravitational Wave Astronomy, June 1-12, 2009.
Competitive entrance, travel grant.

Service and Activities

USU SIAM Student Chapter Member and Webmaster
Webmaster for student club. Helped develop and instruct biweekly C++ programming tutorial sessions.

USU Science Unwrapped Lecture Series Volunteer, 2009-2010.

UAA Alaska Natives in Science and Engineering (ANSEP) Tutor, 2007-2008

UAA IEEE Student Branch Founding Chairman, 2007.

IEEE INFOCOMM Volunteer, May 2007

Tang Soo Do Black Belt Instructor, 2007.

OTHER WORK EXPERIENCE

ExxonMobil Exploration Company, Houston, TX
Geophysical Processing Intern

- Trained and worked with Omega2 and OpenCPS seismic data processing software.
- Familiarized with various seismic processing skills including: survey geometry, velocity analysis, frequency filtering and spectral analysis, NMO correction, statics corrections, mute picking, visualization, demultiple, stacking, and seismic migration.
- Implemented 5D interpolation in Omega2 for multiple surveys for the first time at ExxonMobil. Had a significant impact on four production datasets, two of which were time sensitive.
- Collaborated with the ExxonMobil Upstream Research Company for testing new interpolation tools in OpenCPS.
- Created 5D interpolation documentation and reference materials for future use by ExxonMobil.
- Participated in various intern educational events.

Alaska Air National Guard, Anchorage, Alaska
Search and Rescue Loadmaster

- Responsible for aircraft inspections, equipment rigging, loading operations supervision, air-drop operations, and in-flight helicopter refueling.
- Deployed twice in support of OEF (Uzbekistan, Afghanistan, and Djibouti, Africa)
- Vehicle control officer responsible for equipment totalling $240K.

REFERENCES

Dr. Shane Larson, Dept. of Physics and Astronomy, Northwestern University
Ph.D. Advisor, shane.larson@northwestern.edu, (847) 467-4305

Dr. Todd Moon, Dept. of Electrical and Computer Engineering, Utah State University
Master's Advisor, todd.moon@engineering.usu.edu, (435) 797-2970

Dr. Jens Munk, Dept. of Engineering, University of Alaska, Anchorage
Undergraduate Advisor, afjm@uaa.alaska.edu, (907) 786-7754

Erik Neumann, Geophysical Processing, ExxonMobil Exploration Co.
Supervisor, erik.neumann@exxonmobil.com, (281) 654-2987